Utilization of Decomposition Techniques for Analyzing and Characterizing Flows

Carlsson, Christian

2014

Citation for published version (APA):
Carlsson, C. (2014). *Utilization of Decomposition Techniques for Analyzing and Characterizing Flows*. [Doctoral Thesis (compilation), Department of Energy Sciences].

Total number of authors:
1

LUND UNIVERSITY

PO Box 117
221 00 Lund
+46 46-222 00 00

Utilization of Decomposition Techniques for Analyzing and Characterizing Flows

Christian Carlsson

Doctoral Thesis

Division of Fluid Mechanics
Department of Energy Sciences

Lund University, Sweden
2014

Populärvetenskaplig sammanfattning

Vetskap om strömning av vätskor och gaser är viktigt i dagens samhälle, vilket inkluderar transport i rör, förbränning, och flödesinducerade vibrationer. På grund av sin flyktiga form är möjligheten att kontrollera flöden i diverse applikationer begränsad. Strömning kan vara väldigt svårt att beskriva och kategorisera, speciellt då höga hastigheter är inblandade. Hastigheten i olika punkter i flödet är oftast väldigt oförutsägbar, och detta får stora konsekvenser när man vill blanda eller transportera olika substanser. Ett karakteristiskt inslag hos flöden med höga hastigheter är uppkomsten av virvlar och liknande strukturer av olika storlekar. Ett visst synsätt kan leda till att behandla olika strukturer som individuella delar, vars summa innefattar hela flödet. Detta är alltså ett försök att underlätta situationen genom att först dela upp flödet, för att sedan analysera de individuella delarna. Tillsammans med slumpmässiga strukturer kan det också uppstå flödesmönster som upprepar sig periodiskt, eller nästan periodiskt, varje fall inom ett visst tidsintervall. Dessa återkommande mönster är ofta stora och energirika, och kan ha ett dominerande inflytande på flödet i stort. Till exempel kan de ge upphov till en ökad friktion och energiförlust för rörflöde, eller till att inducera storskaliga tryckoscillationer i gasturbiner. För att kunna definiera och utvärdera olika flödesmönster krävs robusta metoder, vilka bör baseras på vettiga fysikaliska kriterier. Detta skulle kunna innefatta energirika strukturer, eller strukturer som oscillerar med en enda frekvens.

Denna avhandling syftar till att undersöka och karakterisera storskaliga strukturer för flöden i olika typer av situationer. I första hand hanteras ett fall med ett inkommande turbulent flöde till ett 90° krökt rör. Fallet riktar sig mot att förklara ett fenomen, kallat 'swirl switching', där någon form av storskalig rotation eller deformation av flödet sker nedströms om kröken. Resultat från numeriska studier visar på en koppling mellan detta fenomen och långa energirika flödesformationer som bildas uppströms, i det raka röret. Andra fall som också har behandlats involverar starkt roterande strömning, från inlopp till utlopp, vilket ger flödespartiklar som rör sig i en spiralform. Dessa strömningar har en tendens att sakta ner flödet, och t.o.m. orsaka hastigheter i riktning mot inloppet. Detta bidrar i sin tur till starka strukturer, vilka får möjlighet att byggas upp i stället för att transporteras nedströms. Denna typ av flöde, med en hög rotationsnivå, används flitigt för att stabilisera flammor i befintliga gasturbiner. En annan typ av flamstabilisering, vilket härstammar från ett nyare koncept, bygger på en låg rotationsnivå. Eftersom hastighetsändringarna för dessa flöden är lägre, har man lyckats skapa stabila flammor med låg temperatur, som dessutom svävar en bra bit över brännaren. Detta kan däremot vara en väldigt känslig uppsättning, med en flamma som lätt blåser iväg. En mekanism som hjälper till att förankra flamman har isolerats, och presenteras i denna avhandling. Till sist har vakflöden för strömning kring olika objekt studerats, där objekten har förflyttats/deformerats som svar på krafter från flödet. Fallen behandlar strömning kring en cylinder fastspänd i fjädrar, en uppsättning av fyra cylindrar fastspända i fjädrar, och en balk som är fastspänd i ena änden. Olika strukturer har extraherats, och fysikaliska förklaringar har lagts fram.

Abstract

This thesis presents the utilization of two different decomposition techniques, proper orthogonal decomposition (POD) and dynamic mode decomposition (DMD), for enhanced understanding of flow structures and their stability. The advantages of these techniques are shown for a range of flow situations, most of which are turbulent. It is shown that by these methods additional insight into complex flow situations can be gained. Such insight has been found to be needed for the flow in straight and 90° curved pipes. The so-called swirl switching phenomenon is investigated, which is a large scale oscillation of the flow after the bend. This phenomenon is classified into a low frequency and a high frequency switching, each with its own mechanism of formation. It is shown that while the low frequency switching stems from very-large-scale motions created in the upstream pipe, the high frequency switching results from the bend itself, making it an inherent property of the system.

The second set of studies consider swirling flow in combustor-related geometries, using both high and low swirl levels. These investigations show highly energetic unsteady structures in the strongly vortical regions. The spatial symmetry of these flow modes reflect the level of confinement. While the vortices that are weakly confined show unsteady modes reflecting their displacement, the strongly confined vortices show low-order multipole deformations. For the low swirl burner, which is the only reacting flow considered, the flame is stabilized without the presence of vortex breakdown. To be able to investigate how the flame is anchored above the burner, an extended version of DMD (EDMD) is introduced, which helps to couple the flow with the flame. Using this method, a mechanism contributing to the flame stabilization is isolated.

The third and final set of studies involve flow around cylinders and beams. These objects are flexible and respond to the forces that the flow exerts on them. For the flow around cylinders, which are connected to a spring system, the natural frequency of the spring-cylinder system and the frequency from the von Karman vortex shedding are the two a priori known frequencies of the system. Three different flow regimes are considered, one where the two frequencies are similar, giving resonance, and two cases where one frequency is far above/below the other. For flow around a single cylinder, an unexpected high energy low frequency mode is found off-resonance, which is argued to contribute greatly to the chaotic behaviour for the case with the loose spring. For a multiple cylinder array, while the strong low frequency mode found for the single cylinder case has been suppressed, an unexpected synchronization is seen. Considering the flow around a stiff and a flexible beam, a strong beat frequency is found for the lift force. While the beating is seen to be regular for the flexible beam, it appears intermittently for the stiff beam. The flow behaviour giving rise to this forcing is elucidated using the POD and DMD analyses.

List of papers

Paper I
C. Carlsson, E. Alenius, and L. Fuchs - Swirl switching in turbulent flow through 90° pipe bends. To be submitted for journal publication.

Paper II
Y. Wu, C. Carlsson, R. Szazs, L. Fuchs, and X.-S. Bai - Geometry outlet contraction ratio effect to the swirling flow structure and precessing vortex core. To be submitted for journal publication.

Paper III
P. Petersson, R. Wellander, J. Olofsson, H. Carlsson, C. Carlsson, B. Beltoft Watz, N. Boetkjaer, M. Richter, M. Aldén, L. Fuchs, and X.-S. Bai - Simultaneous high-speed PIV and OH PLIF measurements and modal analysis for investigating flame-flow interaction in a low swirl flame. 16th Int. Symp. on Applications of Laser Techniques to Fluid Mechanics, Lisbon, Portugal, 9-12 July, 2012.

Paper IV
H. Carlsson, C. Carlsson, L. Fuchs, and X.-S. Bai - Large eddy simulation and extended dynamic mode decomposition of flow-flame interaction in a lean premixed low swirl stabilized flame. *Flow, Turbulence and Combustion* Volume 93 Issue 3 (2014) pp. 505-519 DOI 10.1007/s10494-014-9560-6

Paper V
A. Cesur, C. Carlsson, L. Fuchs, and J. Revstedt - Modal analysis for oscillating cylinder arrays at low Reynolds number. Under review for publication in Journal of Fluids and Structures.

Paper VI
A. Cesur, C. Carlsson, A. Feymark, L. Fuchs, and J. Revstedt - Analysis of the wake dynamics of stiff and flexible cantilever beams using POD and DMD. *Computers and Fluids* **101** (2014) pp. 27-41 DOI 10.1016/j.compfluid.2014.05.012

Contents

1 Introduction **9**
- 1.1 Outline of the studied cases 11
- 1.2 Preliminaries 13
- 1.3 Outline of the thesis 13

2 Flow instability and turbulence **15**
- 2.1 Governing equations 15
  - 2.1.1 Momentum conservation 15
  - 2.1.2 Mass conservation 16
  - 2.1.3 Energy conservation 17
  - 2.1.4 Constant density and viscosity 17
  - 2.1.5 Initial and boundary conditions 18
  - 2.1.6 Velocity derivatives 18
  - 2.1.7 Fluctuations from a base flow 19
- 2.2 Flow instability 20
  - 2.2.1 Local and global stability analysis 21
  - 2.2.2 Local inviscid instabilities 22
  - 2.2.3 Small and large disturbances 23
  - 2.2.4 Instability and flow patterns in swirling flow 25
  - 2.2.5 Bifurcation analysis and weak nonlinearity 27
  - 2.2.6 Transition and strong nonlinearity 31
- 2.3 Turbulence 32

3 Stability analysis - methodology **35**
- 3.1 Global linear instability 36
  - 3.1.1 Arnoldi method 36
  - 3.1.2 Implicitly restarted Arnoldi method 38
- 3.2 Optimal linear transient growth 39
- 3.3 Proper orthogonal decomposition 40
- 3.4 Koopman analysis 42
  - 3.4.1 Dynamic mode decomposition 43
  - 3.4.2 Extended DMD 45

4 Chaotic time series analysis **46**
4.1 Time delay 47
4.2 Embedding dimension 47
4.3 Attractor dimension 49
4.4 Global Lyapunov spectrum 50

5 Computational models **53**
5.1 Reynolds averaged Navier-Stokes equations 54
  5.1.1 $k - \epsilon$ model 54
5.2 Large eddy simulation 55
  5.2.1 Smagorinsky model 56
  5.2.2 Germano procedure 56
  5.2.3 Scale-similarity model 57
  5.2.4 Implicit LES (ILES) 57

6 Reacting flows **59**
6.1 Turbulent premixed combustion 60
  6.1.1 Flame tracking: G-equation 61

7 Numerical methods **63**
7.1 Grid generation 63
7.2 Second-order finite volume method 64
7.3 Temporal discretization schemes 66
  7.3.1 1st order explicit scheme 66
  7.3.2 1st order implicit scheme 66
  7.3.3 2nd order implicit/backward scheme 66
7.4 Spatial interpolation schemes 67
  7.4.1 Convection term 67
  7.4.2 Diffusion term 68
  7.4.3 Pressure gradient 69
7.5 Pressure-velocity coupling 69
  7.5.1 PISO-algorithm 69

8 Turbulent flow through straight and curved pipes **71**
8.1 Pipe flow 71
  8.1.1 Laminar pipe flow 71
  8.1.2 Transitional pipe flow 72
  8.1.3 Turbulent pipe flow 73
8.2 Flow through curved pipes 76
  8.2.1 Laminar flow through curved pipes 76
  8.2.2 Swirl switching for 90° curved pipes 77
8.3 Results 79
  8.3.1 Results - Turbulent pipe flow 79
  8.3.2 Results - Swirl switching for 90° curved pipes 82
  8.3.3 Results - Summary 85

9 Summary of results - Swirl burners 87
9.1 High swirl - two cold flow studies 88
9.1.1 Results - VT40 burner 89
9.1.2 Results - Expanding/Contracting pipe 92
9.2 Low swirl - stratified premixed combustion 96
9.2.1 Results 97

10 Summary of results - Flow around interacting cylinders and beams 101
10.1 Single and multiple cylinders connected to springs 102
10.1.1 Results - Single cylinder 103
10.1.2 Results - Multiple cylinders 105
10.2 Stiff and flexible beams 107
10.2.1 Results 108

11 Summary of papers and contributions 112

12 Future work 116
12.1 Bifurcation analysis of a swirling jet 116

Chapter 1

Introduction

The flow of water, or the movement of a flame, can hold the attention of people for long periods of time. The irregularity in the motion, which makes it interesting to look at, results from a large number of degrees of freedom interacting in a nonlinear fashion. However, one of the important discoveries during the 20th century was that a large number of degrees of freedom is not necessary to create complexity. Even very simple looking equations can give solutions far beyond human comprehension. This naturally raises questions regarding the complexity of fluid flow, and the effective number of degrees of freedom needed to capture its essence.

The importance of structures in fluid flow compared to the importance of statistics has long been an open question. While names have been given to certain perceived patterns and events, such as streaks and bursts, the role that they play is still very much unclear. Nevertheless, the need to find recurring states is common to most dynamical systems, and statistical measures clearly play a roll in much of this. The high dimensional systems encountered in fluid mechanics do not alleviate the situation, where a plethora of spatial patterns can emerge. The need to be able to reduce these high dimensional systems, by extracting recurring spatial structures or highlighting active regions, is often of great importance. More broadly, the field of spatio-temporal chaos is still in its infancy, and a lot of new ideas are needed.

While slow moving fluids are known to behave nicely, there appears to be no universal set of steps governing how fast moving fluids transition into irregular, or turbulent, motion. The transition can be immediate, or it can follow from a sequence of intermediate states. Likewise, the current understanding of why turbulent flow often stay turbulent, i.e. how it is able to sustain itself, is valid only for wall free, ideal turbulence. Generally, the energy loss to heat typically is (much) larger than for laminar flow and hence it is not obvious why a turbulent state is selected. Even though turbulence is such an important phenomenon, and the equations governing its motion are believed to be known, information regarding its behaviour, coming from first principles, is virtually nonexistent. Therefore, most of what is known about turbulence comes from experiments, phenomenology, and, as of late, computer simulations. While turbulence is found to be a positive feature in certain systems, such as when mixing of fuel and oxidizer needs to take place quickly, it is found to be a negative feature in others, such as when the flow resistance increases for fluid transport. Either way, it needs to be understood.

The primary invesitgation in this thesis is that of turbulent flow through a 90° curved pipe. In particular, a study of the phenomenon called *swirl switching*, first discovered by Tunstall & Harvey [75], is conducted. However, the thesis will also try to shed some light on concepts and methods useful for the analysis of flow instability and coherent structures; in particular, the methods *proper orthogonal decomposition* (POD) and *dynamic mode decomposition* (DMD) are investigated. While POD extracts structures based on optimal energy content, DMD extracts structures oscillating at a given frequency. The end goal is not to improve the procedures used for the study of laminar or transitional flows, but rather to explore different ways to analyse and classify large scale coherent structures that exist in fully turbulent flows. Because of the elusive nature of turbulence, the methods used for extracting flow structures become very important. In fact, the very notion of a "coherent structure" is intimately connected to the extraction method. In evaluating these methods, the applications range from low Reynolds number cold flows to high Reynolds number flame-flow interactions. Large networks of pipes is an example where turbulence usually works against our interests. The enhanced dissipation rate for turbulent flow in straight pipes, compared to laminar flow, can be substantial, not to mention the flow that results from the joints and bends that have to be included. The increased pressure drop resulting from curved pipe sections can be very costly, and needs to be weighed with the capital cost of the network. In addition to pure transport, heat transfer in pipes also has important applications, such as for e.g. heat exchangers. The heat transfer rate experiences a large growth for turbulent flows due to the additional advective thermal flux. Also, the altered velocity profiles for curved pipes generally imply improved heat transfer characterstics. This way of using the pipe geometry to increase the heat transfer is called a passive technique, as opposed to an active technique, such as induced vibrations.

The heat transfer and transport of fluids in pipes alone do not drive the economy. Combustion is estimated to account for about 90% of the world's energy supply [80]. With a diminishing rate of return as the easily accessible oil gets depleted (starting from a ratio at about 50:1 [47]), together with rising concerns about CO_2 levels in the atmosphere and pollutants adversely affecting the health of living things in the biosphere, more emphasis is being placed on efficiency as well as pollution reduction in the energy and transport sectors. A step in this direction, particularly concerning gas turbines, is to remove energy draining mechanical parts from the flame region, by stabilizing the flame using the flow itself, thereby increasing efficiency as well as reducing material cost and maintenance. A way of realizing this is to use swirling (rotational) flows, with different frameworks using either high or low swirl levels. Some form of swirl stabilized combustion is used for more than 50% of all fossil fuels [77]. Another step, particularly concerning stationary gas turbines, is to use premixed flames with a low equivalence ratio, resulting in the ability to reduce the temperature and thereby suppress NO_x production. However, these types of systems in confined spaces are prone to combustion instabilities coming from a coupling between flame and pressure fluctuations due to heat release, possibly resulting in devastating mechanical oscillations of critical components of gas turbines.

Problems with mechanical oscillations of course also occur in many other areas, such as for flow around bluff bodies, where the resulting fluid-structure interaction can produce very non-trivial results. Applications include the flow around airplane wings, buildings and tall structures, or perhaps around pipes and cables immersed in water. It would obviously be useful to be able to predict the outcomes before constructing the (often costly) material objects, and numerical simulations are gaining traction in this area. For example, the tallest building in the world, the 830 meter tall Burj Khalifa in Dubai, has a tapered structure (wide base gradually narrowing towards the top). This suggests that the flow induced pressure oscillations along the building will have different frequencies, which should result in a much smaller net force on the building, compared to one with a uniform cross section along its height.

1.1 Outline of the studied cases

The main aim of the thesis is to utilize reduction methods for improving understanding of unstable flow processes under a variety of conditions. These techniques (POD and DMD) have been applied to different cases and these are listed and described very briefly in the following together with some of the main results.

- Turbulent flow through 90° curved pipes are investigated. Besides the well-known Dean vortices, which are two counter-rotating axial vortices found after pipe bends for laminar flow in gradual bends, the so-called "swirl switching" phenomenon has been seen to occur for turbulent flow in earlier studies. The term appears to entail either a single axial vortex after the bend, or a situation where one of the Dean vortices dominates over the other, giving a net circulation. The net swirl, in turn, switches between a right handed and a left handed direction along the pipe axis. A mechanism for the swirl switching is proposed, involving large scale structures created in the upstream pipe. These large scale structures have a strong streamwise velocity component, and are much longer than the pipe diameter.

- Cold-flow in a geometry similar to the Volvo VT40 swirler and combustor is considered. While the diameter of the exhaust pipe is varied, the resulting structure of the highly swirling flow is studied. Since the swirler is annular, an outer vortex ring is developed, together with an inner vortex core along the centre axis of the burner and in the exhaust pipe. Various displacements and deformations of these two vortex regions, whose strength and shape changes with the exhaust pipe diameter, are characterized.

- A swirling flow through a suddenly expanding and contracting pipe is investigated. The swirler, consisting of a central hub together with eight swirl vanes, is positioned far upstream of the expansion. As the swirl level is increased, a vortex breakdown is seen at the expansion, giving a backflow for the mean velocity field along the centre line. At the same time, time dependent large scale coherent structures appear in the flow. Three unsteady large scale structures are isolated. The strongest coherent structure is the precession of the vortex core at the sudden expansion, which oscillates at a single frequency. Inside the expanded pipe region, a developing vortex is seen to travel upstream from the sudden contraction, stopping downstream of the expansion. The developed vortex core inside the expanded pipe is then displaced, giving rise to motion involving a range of low frequencies. Finally, the flow between the swirler and the expansion shows a narrow high frequency spectrum, with a dominant flow structure corresponding to a deformation of the vortex in the pipe.

  There are a few interesting similarities with the VT40 burner, such as the connection between the unsteady large scale coherent structures and the vortical regions. The practically unconfined vortices give strong modes reflecting their *displacement*, while the confined vortices, which are more influenced by the walls, show strong modes reflecting their *deformation*.

- An annular reacting swirling flow, with a low swirl level, is studied. This way of stabilizing a flame, without making use of vortex breakdown and a strong backflow, is a recent development. The equivalence ratio of the fuel is low, resulting in a low temperature, and the flame is lifted high above the nozzle. These features lead to a flame prone to instabilities. It is therefore of interest to classify the different flow structures that help anchor the flame above the nozzle. A flow structure contributing to the flame stabilization is isolated using and extended version of DMD. This flow structure represents a high order deformation of the vortex, and likely stems from a Kelvin-Helmholtz instability of the inner shear layer.

- The wake of a single cylinder connected to springs is investigated. Two characteristic frequencies are present, one connected to the spring-cylinder system in the fluid, and the other to the von Karman vortex street appearing in the wake of bluff bodies. Three different flow regimes are considered; one where the two frequencies are very similar, showing a resonant behaviour with large cylinder displacements, and two where one of the frequencies is above/below the other. In particular, an unexpected low frequency motion gives a strong contribution for both cases off-resonance. Also, for the case with a loose spring constant, a chaotic behaviour is seen for the cylinder motion. This behaviour is addressed in terms of a feedback between the cylinder motion and the low frequency flow mode.

- The flow past an array of four cylinders, where each cylinder is connected to springs, is also investigated. The highlighted case involves a square formation, where the cylinders are positioned at the edges. Just as for the single cylinder case, three different regimes are considered. The strong low frequency mode, so prominent for the single cylinder case, is found to be suppressed. An unexpected synchronization is seen, where the upper and lower cylinders are compelled to oscillate either in phase or in antiphase. While the von Karman shedding appears to support oscillation in antiphase, the flow phenomenon supporting oscillation in phase is unknown.

- The flow around a stiff and a flexible cantilever beam is analysed. The lift force on the flexible beam shows a clear beat frequency, while the lift force on the stiff beam shows an intermittent beating. The forces on the beams are elucidated by extracting the responsible flow structures. While one of these structures is the von Karman shedding, the other one is a less known low frequency motion giving a symmetric pattern in wake.

1.2 Preliminaries

A large focus in this thesis is placed on the symmetries of different flow structures. Frequent referral will be made to the azimuthal wavenumber m, where,

$$\phi(r,\theta,z) = \widehat{\phi}(r,z)e^{im\theta}$$

for some quantity ϕ in cylindrical coordinates. For swirling flows, a sign is often given to the azimuthal wavenumber, with $\pm m$ depending on whether the helical structure winds in the same or in the opposite direction with respect to the mean flow. However, the sign conventions unfortunately differ in the literature. Therefore, to avoid confusion, $|m|$ will be used together with an explicitly stated winding direction. Besides the winding direction, the direction of rotation will also be stated.

An important parameter for swirling flows is the swirl number, which is a measure comparing the azimuthal and axial momentum. The measure used in this thesis is typically the integrated flux of azimuthal and axial momentum,

$$Sw = \frac{\int \rho r u_\theta u_z dA}{R \int \rho |u_z| u_z dA}$$

where u_θ and u_z are the azimuthal and axial velocities, respectively, and R is a reference radius.

1.3 Outline of the thesis

The governing equations of fluid flow, together with the subjects of flow instability and turbulence, are introduced in Section (2). Methodology in stability analysis, including POD and DMD, is given Section (3), followed by methods to analyse chaotic time series in Section (4). Computational methods, including spatial filtering and temporal/ensamble averaging of the governing equations, are outlined in Section (5), and a brief introduction to reacting flows is given in Section (6). Numerical methods, in particular for the second-order finite volume method, are given in Section (7). In Section (8), turbulent flow in straight and curved pipes are introduced, and results are summerized. Further summaries are provided in Sections (9) and (10), for the studies of the swirl burners and the interacting cylinders/beams, respectively. Finally, a summery of the papers together with contributions are given Section (11), ending with an outline of future work in Section (12).

Chapter 2

Flow instability and turbulence

2.1 Governing equations

The field of fluid dynamics is commonly handled by continuum models that describe the conservation of *momentum*, *mass*, and *energy*. A fluid flow is typically considered in the so-called Eulerian setting, where observations are made in a "fixed" frame, as opposed to the Lagrangian framework where individual fluid parcels are followed through space and time. A temporal change of one of the above quantities in a volume element must be accompanied by a *net* inflow/outflow, or flux, through the boundary of the element, or some other external influence. The additional influences, not already accounted for by the flux terms, end up in a source term.

2.1.1 Momentum conservation

Considering the conservation of momentum per unit volume ρu_i, using Newton's second law, and Cartesian coordinates, gives

$$\frac{\partial \rho u_i}{\partial t} + \frac{\partial \rho u_i u_j}{\partial x_j} = \frac{\partial \sigma_{ij}}{\partial x_j} + \rho f_i, \tag{2.1}$$

where u_i is the velocity field, ρ is the density, σ_{ij} is the total stress tensor, and ρf_i represents body forces (for example, gravity). Summation over repeated indices ($j = 1, 2, 3$) is implied. The first term on the left hand side represents the temporal change of the momentum, while the second term is the so-called convective (or advective) term, showing how the flow "transports itself". The first term on the right hand side represents the normal and shear forces on a given fluid element, which needs to vary in space in order to give a *net* force (therefore the derivative). The second term on the RHS, ρf_i, represents various types of body forces, where "body" should be put in contrast to the surface forces given by σ_{ij}. While eq. (2.1) may be considered to be exact, it is not very useful, since, in particular, σ_{ij} is unknown.

The total stress tensor, which is symmetric, $\sigma_{ij} = \sigma_{ji}$, is usually decomposed into

$$\sigma_{ij} = -p\delta_{ij} + \tau_{ij}, \tag{2.2}$$

for the pressure p and the traceless symmetric shear stress tensor τ_{ij}. While p seeks to stretch/compress the fluid element, τ_{ij} seeks to shear the fluid element. For a Newtonian fluid τ_{ij} is written as

$$\tau_{ij} = 2\mu s_{ij} - \frac{2}{3}\mu\frac{\partial u_k}{\partial x_k}\delta_{ij}, \tag{2.3}$$

where s_{ij} is the strain rate

$$s_{ij} = \frac{1}{2}\left(\frac{\partial u_i}{\partial x_j} + \frac{\partial u_j}{\partial x_i}\right), \tag{2.4}$$

and μ is the dynamic viscosity, which is a material property that generally depends on the temperature. For many fluids, such as air and water (under a large range of conditions), the Newtonian fluid model appears to be a good approximation.

2.1.2 Mass conservation

Moving on to the mass conservation,

$$\frac{\partial \rho}{\partial t} + \frac{\partial \rho u_j}{\partial x_j} = 0, \tag{2.5}$$

which simply says that any change in time of the mass in a given volume must be balenced by a net inflow/outflow through the bounding surface. If several different components or species are considered, such as hydrocarbons and oxygen for combustion, the conservation equation becomes

$$\frac{\partial \rho_i}{\partial t} + \frac{\partial \rho_i (\vec{u}_i)_j}{\partial x_j} = \dot{m}_i \tag{2.6}$$

for each species i with velocity $\vec{u}_i$, allowing for a source term $\dot{m}_i$ representing chemical reactions. By introducing $\vec{j}_i = \rho_i(\vec{u}_i - \vec{u})$, using an average flow $\vec{u}$ for all the species, eq. (2.6) may be rewritten as

$$\frac{\partial \rho_i}{\partial t} + \frac{\partial \rho_i u_j}{\partial x_j} = -\frac{\partial (\vec{j}_i)_j}{\partial x_j} + \dot{m}_i,$$

where $\vec{j}_i$ needs to be modelled using, for example, Fick's law. This way of handling multiple species, using an average flow and treating the deviation as some form of diffusive transport, thereby avoiding the need to have to account for the velocity field of each species separately, is common.

2.1.3 Energy conservation

The energy per unit mass $E = e + \frac{1}{2}u_i u_i$ may be introduced, including the internal (or heat) energy per unit mass e and the kinetic energy per unit mass $\frac{1}{2}u_i u_i$. The governing equation for the energy per unit volume ρE is given by

$$\frac{\partial \rho E}{\partial t} + \frac{\partial \rho E u_j}{\partial x_j} = -\frac{\partial q_j}{\partial x_j} + \frac{\partial u_i \sigma_{ij}}{\partial x_j} + \rho u_i f_i + S \tag{2.7}$$

where q_j represents heat conduction and/or energy transport by particle diffusion, which are both flux terms, whereas S represents heat release from chemical reactions and/or electromagnetic radiation. The conduction part of the term q_j might be modelled using, for example, Fourier's law. Note that eq. (2.7) is used to solve for the internal energy (per unit volume) ρe. Using the governing equation for the kinetic energy per unit mass, obtained by multiplying eq. (2.1) with u_i and summing over i, given by

$$\frac{\partial \rho \frac{1}{2}u_i u_i}{\partial t} + \frac{\partial \rho \frac{1}{2}u_i u_i u_j}{\partial x_j} = u_i \frac{\partial \sigma_{ij}}{\partial x_j} + \rho u_i f_i, \tag{2.8}$$

and subtracting it from eq. (2.7) gives

$$\frac{\partial \rho e}{\partial t} + \frac{\partial \rho e u_j}{\partial x_j} = -\frac{\partial q_j}{\partial x_j} + \sigma_{ij} s_{ij} + S.$$

However, often the internal energy is not directly considered, but instead the enthalpy or temperature.

2.1.4 Constant density and viscosity

For a general case, the equations for ρu_i, ρ, ρ_i, and E, together with an equation of state, all need to be used, at least in some approximate form. However, for the special case of having a constant density ρ and a constant dynamic viscosity $\mu \equiv \rho\nu$, as well as neglecting any body forces, eq. (2.1) may be written as

$$\frac{\partial u_i}{\partial t} + u_j \frac{\partial u_i}{\partial x_j} = -\frac{1}{\rho}\frac{\partial p}{\partial x_i} + \nu \frac{\partial^2 u_i}{\partial x_j^2}, \tag{2.9}$$

where ν is called the kinematic viscosity, together with eq. (2.5) which becomes

$$\frac{\partial u_j}{\partial x_j} = 0. \tag{2.10}$$

The four equations in (2.9) and (2.10) may solve for the four unknowns u_i $(i = 1, 2, 3)$ and p. The momentum equations for a Newtonian fluid are called the Navier-Stokes equations, and in particular showing existence and smoothness of solutions to eqs. (2.9) and (2.10), given some smooth initial conditions, is one of the Clay Mathematics Institute Millennium Problems [24].

Thus, by assuming constant density and viscosity, which in particular implies a temperature independence, the momentum and mass equations have been decoupled from the energy equation. The central object has become the velocity field u_i, while the pressure(-like) field p should adjust in order to satisfy the kinematic (as opposed to dynamic, i.e. there is no explicit force involved) constraint in eq. (2.10). Applying the divergence operator on eq. (2.9), utilizing eq. (2.10), an equation of elliptic character is aquired for the pressure, implying an immediate global influence (stemming from the constant density approximation). Note that adding a conservative force $f_i = \nabla_i \phi$ (such as gravity) to eq. (2.9) leads to the same equation with the change of variable $p \to \widetilde{p} = p - \rho\phi$. Eqs. (2.9) and (2.10) are often scaled using a typical length d and time d/U, giving

$$\frac{\partial u_i^*}{\partial t^*} + u_j^* \frac{\partial u_i^*}{\partial x_j^*} = -\frac{\partial p^*}{\partial x_i^*} + \frac{1}{Re} \frac{\partial^2 u_i^*}{\partial x_j^{*2}} \tag{2.11}$$

and

$$\frac{\partial u_j^*}{\partial x_j^*} = 0, \tag{2.12}$$

where

$$u_i^* = \frac{u_i}{U}, \quad p^* = \frac{p}{\rho U^2}, \quad x_i^* = \frac{x_i}{d}, \quad t^* = \frac{Ut}{d},$$

and $Re = Ud/\nu$ is a similarity parameter called the Reynolds number. Therefore, as can be seen in eq. (2.11), similar systems over a large range of scales should be expected to give dynamically similar flow fields, given that their Reynolds numbers are the same. The size of the Reynolds number also signals whether the flow is likely to be *laminar* ($Re \sim 1$) or *turbulent* ($Re \gg 1$). It should be appreciated how a vast range of different flow physics, involving both gases and liquids, appear to be captured by such a ”simple” set of equations as the ones given above.

2.1.5 Initial and boundary conditions

A well-posed problem also requires appropriate initial, $\psi(x, 0) = \psi^o(x)$, and/or boundary conditions for the different fields. Typically, boundary conditions are either of Dirichlet type, $\psi(x, t) = h(x)$ for x on the boundary, or of Neumann type, $\hat{n} \cdot \nabla\psi(x, t) = h(x)$ for x on the boundary, where $\hat{n} \cdot \nabla$ is the derivative in the normal direction $\hat{n}$ to the boundary. If a wall is impermeable, a Dirichlet condition for the velocity component in the normal direction is necessary, $u \cdot \hat{n} = 0$. A Dirichlet condition for the tangential velocity at a solid wall, where the flow velocity takes on the velocity of the wall, is typically used, and is called a no-slip condition.

2.1.6 Velocity derivatives

Integrating eq. (2.8) over some region Ω, assuming a constant density and viscosity, an external force $f_i = 0$, and a velocity field vanishing on the boundary

$\partial\Omega$, gives the expression

$$\frac{d}{dt}\int_{\Omega}\frac{1}{2}\rho u_i u_i dV = -\int_{\Omega}\epsilon dV$$

for the dissipation rate per unit volume $\epsilon = 2\nu s_{ij}s_{ij}$ of kinetic energy. Thus, because of energy conservation (in the full equations) and entropy considerations, there is no positive source term. However, a significant part of fluid dynamics involves the creation/destruction of vorticity. The matrix $\partial u_i/\partial x_j = s_{ij} - \frac{1}{2}\omega_{ij}$ contains 9 terms, which may be divided into a symmetric part s_{ij} containing 6 unique terms, and an anti-symmetric part ω_{ij} containing the remaining 3 terms. The symmetric part is recognized as the strain rate tensor, given in eq. (2.4), while the anti-symmetric part is represented by the vorticity vector ω_i, $\omega_{ij} \to \omega_k$,

$$\omega_i = \varepsilon_{ijk}\frac{\partial u_k}{\partial x_j},$$

where ε_{ijk} is the Levi-Civita symbol. While s_{ij} represents a shearing deformation of the fluid element, the vorticity represents a rotation the fluid element. The governing equation for the vorticity, again assuming constant density and viscosity, is

$$\frac{\partial\omega_i}{\partial t} + u_j\frac{\partial\omega_i}{\partial x_j} = \omega_j s_{ij} + \nu\frac{\partial^2\omega_i}{\partial x_j^2} + \varepsilon_{ijk}\frac{\partial f_k}{\partial x_j}. \tag{2.13}$$

In particular, the term $\omega_j s_{ij}$ is responsible for the vortex stretching/compression and tilting. The analogy of kinetic energy $\frac{1}{2}u_i u_i$ for the vorticity is called the enstrophy, $\frac{1}{2}\omega^2 \equiv \frac{1}{2}\omega_i\omega_i$. By multiplying eq. (2.13) with ω_i, and summing over i, gives the governing equation for the enstrophy,

$$\frac{\partial\frac{1}{2}\omega^2}{\partial t} + u_j\frac{\partial\frac{1}{2}\omega^2}{\partial x_j} = \omega_i\omega_j s_{ij} + \nu\omega_i\frac{\partial^2\omega_i}{\partial x_j^2} + \varepsilon_{ijk}\omega_i\frac{\partial f_k}{\partial x_j}.$$

The enstrophy production, assuming no external forces are present, is given by $\omega_i\omega_j s_{ij}$. It may be noted that both vorticity and strain need to be present at the same spatiotemporal location for the production to be non-zero. The corresponding equation for the strain rate is

$$\frac{\partial s_{ij}}{\partial t} + u_j\frac{\partial s_{ij}}{\partial x_j} = -s_{ik}s_{kj} - \frac{1}{4}(\omega_i\omega_j - \omega^2\delta_{ij}) - \frac{\partial^2 p}{\partial x_i\partial x_j} + \nu\frac{\partial^2 s_{ij}}{\partial x_j^2} + f_{ij}$$

where $f_{ij} \equiv \partial f_i/\partial x_j + \partial f_j/\partial x_i$, and for the contraction $s^2 \equiv s_{ij}s_{ij}$,

$$\frac{\partial\frac{1}{2}s^2}{\partial t} + u_j\frac{\partial\frac{1}{2}s^2}{\partial x_j} = -s_{ij}s_{ik}s_{kj} - \frac{1}{4}\omega_i\omega_j s_{ij} - s_{ij}\frac{\partial^2 p}{\partial x_i\partial x_j} + \nu s_{ij}\frac{\partial^2 s_{ij}}{\partial x_j^2} + s_{ij}f_{ij}.$$

2.1.7 Fluctuations from a base flow

It is sometimes of interest to study fluctuations (u_i', p') from a known base flow (U_i, P), which classically is a steady state solution of the NS equations. Putting the decomposition $(u_i, p) = (U_i + u'_i, P + p')$ into eqs. (2.9) and (2.10) gives

$$\frac{\partial u'_i}{\partial t} + U_j \frac{\partial u'_i}{\partial x_j} + u'_j \frac{\partial U_i}{\partial x_j} + u'_j \frac{\partial u'_i}{\partial x_j} = -\frac{1}{\rho}\frac{\partial p'}{\partial x_i} + \nu \frac{\partial^2 u'_i}{\partial x_j^2}, \tag{2.14}$$

and

$$\frac{\partial u'_j}{\partial x_j} = 0. \tag{2.15}$$

Note that no assumption has been made regarding the size of the fluctuations (u'_i, p') in eqs. (2.14) and (2.15). Eq. (2.14) becomes linearized by removing the term $u'_j \partial u'_i / \partial x_j$, which is described in more detail in Section (3.1).

2.2 Flow instability

Even if a steady state solution to the governing equations is found, with appropriate boundary conditions, does not necessarily mean that the corresponding flow will be seen in nature. The solution also has to be *stable*. Stability theory studies how disturbances/fluctuations u', from a given base flow U, evolve in space and time, (c.f. eqs. (2.14) and (2.15)). However, being able to define whether or not a base flow is stable is not a trivial task, since, beside the computational requirements, the fluctuation field may display very complicated, nonlinear behaviour.

To begin with, a norm $|| \cdot ||$ needs to be selected in order to determine the size/strength of the fluctuation field. A common example is the energy (L2) norm

$$||u'||_2 = \left(\int_\Omega |u'(x,t)|^2 dV \right)^{1/2},$$

considering the spatial domain Ω, assuming that $u' \in L^2(\Omega)$. Note that for extended regions Ω, the disturbances may move around in the domain without affecting the norm. The moving disturbances may at the same time display very intricate temporal behaviour. For example, a disturbance might grow initially, but decay asymptotically in time, displaying so-called *transient growth.* To be able to make sense of such complexity, simplifications and accompanying classifications need to be made.

The most appropriate framework in which to study disturbances may also vary; linear/nonlinear analysis, modal/nonmodal, local/global, etc. Note that the above discussion, considering the stability of the base flow U, could be extended by considering the stability of the resulting, generally time dependent, field $u = U + u'$, and so on. The increasing complexity should be clear, and the tools necessary to handle these situations are very limited. Nevertheless, this type of scenario is seen as a possible route to turbulence, which is discussed at the end of the chapter.

More general information regarding stability and transition of flows can be found in Schmid and Henningson [62].

2.2.1 Local and global stability analysis

Stability analysis may be divided into the two categories *local* and *global*, regarded in the sense of Theofilis [71]. In a local stability analysis there are assumptions made regarding the homogeneity of the base flow. In particular, base flows with *parallel* streamlines are considered, $\vec{U} = (U(y), 0, 0)$, where y is the wall normal coordinate. A *local linear* stability analysis in this case, with a homogenous base flow in the x and z directions, would prompt the ansatz

$$u_i'(x, y, z, t) = \widetilde{u}_i(y) \exp(i(k_x x + k_z z - \omega t))$$

for the fluctuations u_i'. Insertion into the linearized form of eq. (2.14) leads to an eigenvalue problem for $\widetilde{u}_i$. In fact, the equation for the normal component $\widetilde{u}_2$ is the famous *Orr-Sommerfeld equation.* Generally, the parameters k_x, k_z, and ω, can all be complex. In the *temporal* stability problem $k_x, k_z \in \mathbb{R}$ and $\omega \in \mathbb{C}$, implying spatial periodicity and temporal oscillations together with growth/decay, while in the *spatial* stability problem the situation is reversed. In practice, for the temporal stability problem, the wavenumbers are specified while ω is treated as an eigenvalue. Note that the division into temporal and spatial analyses is "artificial", in the sense that it is done for mathematical convenience, and that there are no widely accepted a priori means to determine whether a temporal or a spatial approach should be taken for a given case.

Within the local linear stability framework, the spatial extent is infinite. The consequence when considering a local linear stability analysis, in its application to real flows, is the need to assume a variation of the base flow on length scales much larger than those of the disturbances, which clearly provides significant limitations in its use. A *global* stability analysis instead considers disturbances evolving on a base flow with *at most* one homogeneous direction. The general belief appears to be that the local (when applicable) and global instability studies will show similar results, at least qualitatively, when the local instability is present within a large enough region. However, any precise connection between local and global stability analyses does not exist at present time.

The terms *BiGlobal* and *TriGlobal* analysis were coined by Theofilis [70, 71], referring to global linear stability analysis with respectively two and three inhomogeneous directions of the base flow. With additional inhomogeneities, the stability analysis inevitably becomes less general, and specific flow situations instead become the focus. Note that while these methods of analysis consider small perturbations, the patterns of the unstable modes are still often reflected in the resulting large amplitude patterns of the flow.

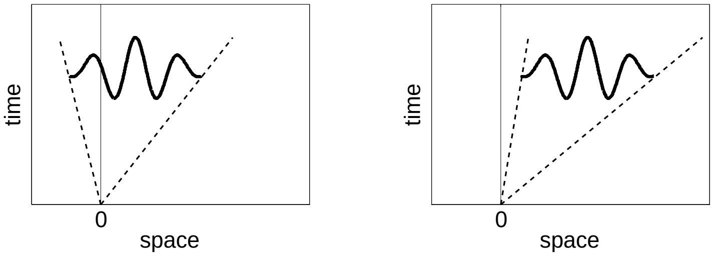

Figure 2.1: Left: absolute instability. Right: convective instability

Also within the local stability framework, regarding *spatio-temporal* instability, a division into *absolute* and *convective* instability may be considered based on the *impulse response* of the system (the input is a "kick" giving all frequencies) [22]. An absolute instability is when the disturbance grows in place, both upstream and downstream, while a convective instability is when the disturbance grows while being convected downstream. A schematic of the two types of instability can be seen in Fig. (2.1). Note that convective instabilities, which are periodically triggered, such as perhaps the flow at a trailing edge, may be treated as spatial modes in the long-time limit.

2.2.2 Local inviscid instabilities

In the days of Kelvin and Rayleigh, during the 19th century, numerous discussions took place regarding the role of viscosity. The prevalent idea was that viscosity only acts to damp instabilities, so the simplification to inviscid conditions was justified. A well known example is the inviscid Kelvin-Helmholtz (KH) instability, which considers the simple discontinuous profile seen in Fig. (2.2) and is unstable for *all* wavelengths. Turning to a more realistic velocity profile, Rayleigh's inflection point theorem states that a *necessary*, but not sufficient, condition for inviscid instability is the presence of an inflection point in the interior of the domain, see Fig. (2.2). A consequence of the introduction of a length scale is the stability of short wavelengths. Flows which could be inviscidly unstable, containing an inflection point in the interior of the flow, include jets, wakes, and boundary layers with a strong adverse pressure gradient.

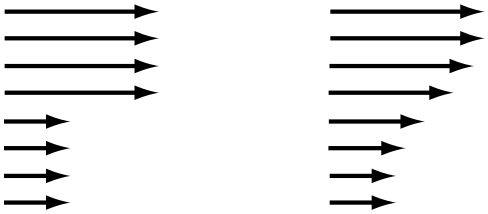

Figure 2.2: Left: base flow for an inviscid Kelvin-Helmholtz instability. Right: more realistic base flow involving a non-zero length scale and an inflection point.

The inviscid centrifugal stability criterion by Rayleigh should also be mentioned. A swirling flow with a uniform axial velocity, where the azimuthal velocity $U_\theta = U_\theta(r)$ depends only on the radial location, is stable to *axisymmetric* $(m = 0)$ perturbations if

$$\frac{d}{dr}(rU_\theta)^2 > 0.$$

This criterion has been shown to be *necessary* and *sufficient* (Synge, 1933) [13].

Besides swirling flows, a centrifugal instability gives rise to the secondary flow seen after a pipe bend, with two counter-rotating axial vortices. Streamlines of such vortices, called *Dean vortices*, are shown in Fig. (2.3).

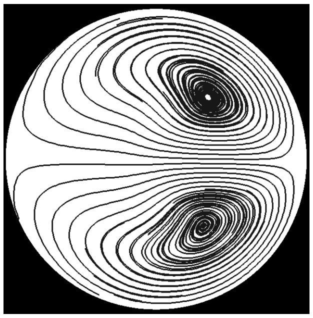

Figure 2.3: Dean vortices. In-plane streamlines showing the secondary flow after a pipe bend. The fluid in the centre is flowing from right to left.

2.2.3 Small and large disturbances

Wall-bounded flows often do not have an inflection point in the interior, and so are not inviscidly unstable. This was handled with some unease in the community, since wall-bounded flows of course are known to become unstable, and it was attributed to the non-parallel nature of real flows and/or nonlinear effects. A paradigm shift came with the realization that viscosity, in certain circumstances, can lead to instability. These instabilities found in boundary layer flows, as predicted by the Orr-Sommerfeld equation (which includes viscosity), are called Tollmien-Schlichting (TS) waves. Using the Orr-Sommerfeld equation, a critical Reynolds number can be obtained for channel flow (plane Poiseuille flow) at $Re_{cr} = 5772$.

The instabilites referred to above, which can be obtained as eigensolutions of the linearized versions of the governing equations, are considered to come from "small" (infinitesimal) disturbances which grow exponentially. However, experimental studies have shown instability for channel flow at much lower Reynolds numbers than the critical value given above. Furthermore, cylindrical pipe flow (or Poiseuille/Hagen-Poiseuille flow) and plane Couette flow are found to be unconditionally stable to small disturbances. As a consequence, one has been able to keep pipe flow laminar for high Reynolds numbers by reducing the disturbance level in the flow, which includes having a very low noise level in the incoming flow. The failure to predict the transitions in these flows have prompted other alternative instability mechanisms, based on "large" (finite) disturbances. A characteristic of these systems is that, while being stable to small disturbances, they become sensitivity to large disturbances above a certain Reynolds number. In addition, the sensitivity generally also increases with increasing Reynolds number. This implies that, for a sufficiently high Reynolds number, the flow will transition because of the inevitability of a certain disturbance level.

A candidate for the (main) transition mechanism in many of these flows is *nonlinear growth*. Analysis of mechanisms based on the nonlinear nature of the equations could include, borrowing notions from dynamical systems theory, basins of attraction and attractor dimension [27, 19]. An attractor, a possible feature of nonlinear dissipative systems, represents a typical behaviour of a system based on the initial conditions. The initial conditions in turn need to be within the basin of attraction of the attractor. Another candidate is *linear transient growth*, also called algebraic growth. This method of growth hinges on the highly non-normal nature of the linearized equations, meaning that the eigenvectors can be far from orthogonal, for high Reynolds number flows. The implication is that some disturbances may grow temporarily before they decay, even though the linearized equations predict monotonic decay for all eigenvectors. The growth factor may be significant, and has been found up to order 10^5 [72]. As such, the disturbances may grow large enough for nonlinear effects to become important. Examples of linear transient growth in cylindrical pipe flow, of disturbances entering an axisymmetric sudden 1:2 expansion, were given by Cantwell *et al.* [8], shown schematically in Fig. (2.4). The fluctuation energy came from an inflectional instability mechanism of the separated shear layer, with the optimal structure reaching a maximum just upstream of the reattachment point, after which it decayed in the downstream pipe. Note that this flow has been found to be unstable to small disturbances, with a critical Reynolds number $Re_{cr} = 3273$ [59], while the practical transition regime has been found in the range $Re = 1000 - 3000$. Therefore, similarly to channel flow, it has been argued that linear transient growth is more important in this flow than the instability of small disturbances. However, if the disturbance level is kept very low, the critical Reynolds number given above again becomes important. Also note the need for a global analysis in this flow, since a local analysis can give very different results depending on where in the flow it is performed.

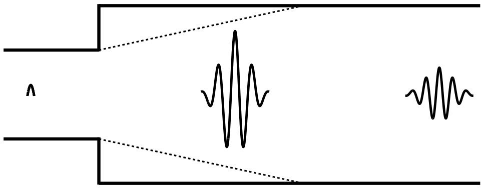

Figure 2.4: Schematic showing the linear transient growth of a disturbance passing through a circular pipe with a sudden expansion [8].

It should be emphasised that linear instabilities can be important in the fully nonlinear regime, and at higher Reynolds numbers, far beyond the transition region. In particular, in the same way that free shear layers show coherent structure which reflect a KH instability of the mean flow, wall shear layers may show coherent structures which reflect the linear transient growth.

2.2.4 Instability and flow patterns in swirling flow

Helical modes are often encountered in swirling flows. As stated in Leibovich & Kribus [34], *"As a rule, vortex flows tend to* [be] *less stable to non-axisymmetric perturbation*[s] *than to axially symmetric ones"*. For example, the radial component of a flow mode representing a *precessing vortex core* (PVC), for a high swirl case at a sudden pipe expansion, is shown in Fig. (2.5). The symmetry of this mode, which has an azimuthal wavenumber $|m| = 1$, implies a displacement of the vortex core, as sketched to the left in Fig. (2.6). The displacement is not static, but rotates, giving the vortex precession. Furthermore, an $|m| = 2$ mode, sketched in the middle of Fig. (2.6), represents a "squeezing" of the vortex core, and so on for higher $|m|$-values. The higher $|m|$-values give rise to more complex shapes, and might therefore be believed to be connected to more specialized mechanisms.

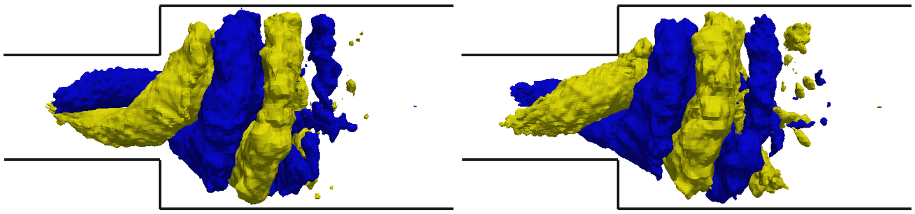

Figure 2.5: Positive/negative isocontours of the radial component of a flow mode representing a PVC at a sudden pipe expansion (bulk flow from left to right). The left and right images represent two different times, showing the precession.

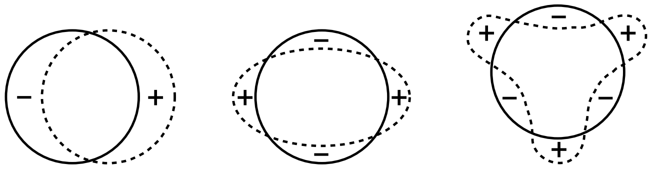

Figure 2.6: Effect of different radial velocity modes on a vortex core. Left: $|m| = 1$, dipole, middle: $|m| = 2$, quadrupole, right: $|m| = 3$, hexapole. The solid and dashed lines represent the base and disturbed configurations, respectively, and the signs represent the transport of some positive quantity (e.g. the axial velocity).

Two helical flow structures above a burner, for a flow with a low swirl level, are shown in Fig. (2.7). The mean flow rotates in the negative direction (right hand rule). The mode on the left has been seen to rotate counter to the mean azimuthal flow direction, while the mode on the right is co-rotating. The mode on the right also winds, or the "arms" of the structure turn, in a direction perpendicular to the mean flow. This observation makes it tempting to connect the structure to a KH roll-up (of the inner shear layer). This is in contrast to centrifugal instabilities, which give rise to vortices that are parallel to the base flow, as exemplified by Taylor and Görtler vortices. The mode on the left, on the other hand, appears a bit more elusive. However, since it is close to the wall (where the azimuthal velocity drops to zero due to the no-slip condition), and winding in the same general direction as the base flow, it could very well come from a centrifugal instability.

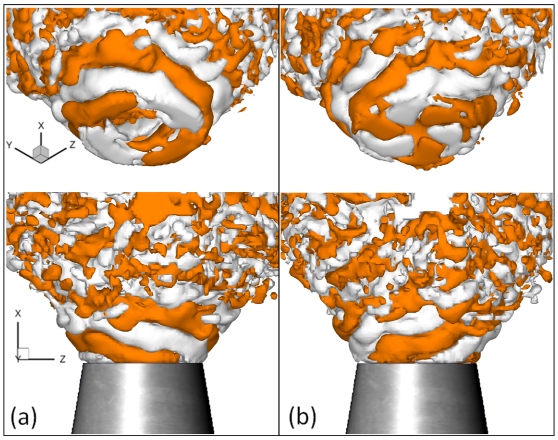

Figure 2.7: Azimuthal vorticity of two flow modes of an LES simulation of a low swirl burner, given at two different angles. Left: $|m| = 2$, right: $|m| = 3$.

Predicting the fixed point frequencies of these type of helical structures is not a trivial task. However, some intuition may be developed by considering them to be "solid objects". In particular, if the structure is spinning with frequency f, it would give the fixed point frequency $|m|f$. On the other hand, if it is being transported with velocity U in the axial direction, it would give the fixed point frequency U/L, where L is the axial wavelength of the mode. Fig. (2.8) illustrates this simple mechanism of rotation.

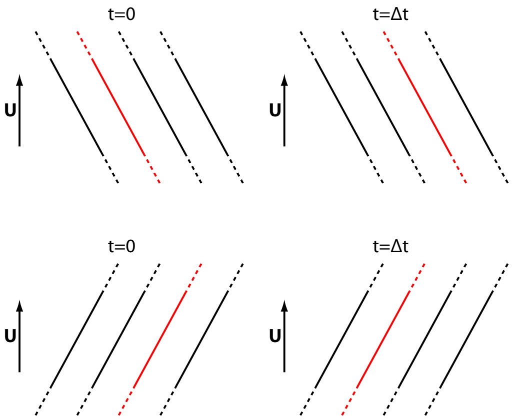

Figure 2.8: Illustration of the (apparent) rotation of helical structures by convection in the axial direction.

2.2.5 Bifurcation analysis and weak nonlinearity

Bifurcation analysis is typically considered in the field of ordinary differential equations (ODEs), where the number of degrees of freedom is a fixed finite number. For partial differential equations (PDEs), on the other hand, the number of degrees of freedom may vary, or be infinte, and much less is known in general. However, in many situations it should be possible to effectively reduce a PDE to a finite dimensional ODE. In particular, this assumption is implicit in the very act of spatially discretizing the equations of motion which, for a fluid, is motivated by the smearing effect of viscosity. Alternatively, the spatial dependence of a flow may be assumed to be approximately known, considering truncated series of Fourier modes or POD modes. Sometimes even a phenomenological model may be sufficient, where some particular feature is captured by an ODE or a system of ODEs.

General theory

Consider a dynamical system depending on a parameter $\gamma \in \mathbb{R}$,

$$\frac{du}{dt} = A(u, \gamma), \tag{2.16}$$

where $A : \mathbb{R}^n \times \mathbb{R} \to \mathbb{R}^n$ is continuously differentiable. A qualitative change in the structure of the solution $u \in \mathbb{R}^n$, or in the number of solutions, as the control parameter γ (e.g. the Reynolds number or swirl number) is continuously altered is called a *bifurcation*. Since the parameter in this case is a single number, only so-called *codimension-one* bifurcations are considered (varying several parameters can of course give more complicated behaviour).

A *local* bifurcation analysis is based on the stability properties of a steady state (u_0, γ_0), $A(u_0, \gamma_0) = 0$. Consider the eigenvalues $\{\lambda_k\}_{k=1}^n$ of the Jacobian

A_u evaluated at (u_0, γ_0). A fixed point where all the eigenvalues have non-zero real parts, $\Re(\lambda_k) \neq 0$, $\forall k$, is called a *hyperbolic fixed point.* Since the Jacobian is invertible at a hyperbolic fixed point, there must also be a unique solution $u = u(\gamma)$ in a neighbourhood of the fixed point, by the Implicit function theorem. By the Hartman-Grobman theorem, the full nonlinear system is equivalent to its linearization in a neighbourhood of a hyperbolic fixed point. Thus, the eigenvalues $\{\lambda_k\}_{k=1}^n$ determine the local stability properties at a hyperbolic fixed point. In particular, if all the eigenvalues have a negative real part, $\Re(\lambda_k) < 0$, $\forall k$, the fixed point is stable to small disturbances.

Thus, moving along a branch of stable solutions, while varying γ, interesting new dynamics only appears when a fixed point becomes *non-hyperbolic.* Assuming that only the real part of one eigenvalue becomes zero such that $\Re(\lambda_m) = 0$ while $\Re(\lambda_k) \neq 0$ for $k \neq m$. This is the most common situation, but the imaginary part $\Im(\lambda_m)$ may either be zero or come as a complex conjugate pair (which in a sense only represents one eigenvalue). If $\Im(\lambda_m) = 0$, the bifurcation is called *stationary,* while if $\Im(\lambda_m) \neq 0$, it is called a *Hopf bifurcation.* For a stationary bifurcation, it is possible to *locally* reduce the high order system to (basically) a one-dimensional system, by invoking Centre manifold theory. The interesting dynamics takes place on the so-called centre manifold, which in this case is one-dimensional, while the rest of the space belongs to the stable manifold.

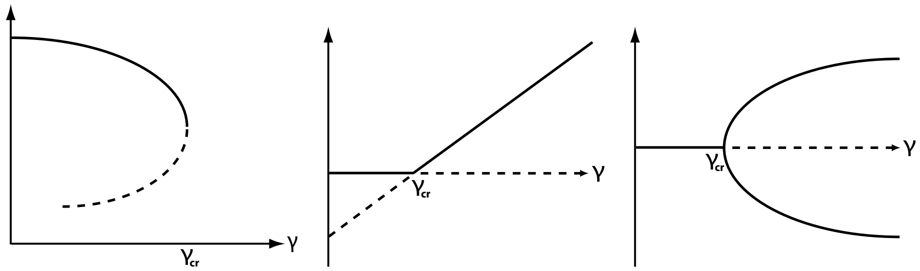

Figure 2.9: Examples of bifurcation diagrams. The vertical axis shows a quantity, on the centre manifold, reflecting a characteristic feature of the system, while the horizontal axis shows the bifurcation parameter γ, including the critical value γ_{cr}. Left: turning point, middle: transcritical, right: supercritical pitchfork. The solid lines represent stable states while the dashed lines represent unstable states.

The simplest stationary bifurcation type, where the fewest assumptions are made, is the turning point bifurcation. For the turning point bifurcation, as the control parameter γ is increased/decreased, two states disappear. With some further restrictions, in particular regarding the symmetry, the transcritical and pitchfork bifurcations can be obtained. For the transcritical bifurcation, as the control parameter is varied, two states cross paths, while for the pitchfork bifurcation, one state is followed by three states. The above three stationary bifurcations are the basic types that are usually encountered, and examples are shown in Fig. (2.9). The notions of bifurcation and stability are also intimately related, as is shown in Fig. (2.9) where the dashed lines are used to indicate unstable states. For the Hopf bifurcation, the reduced order system is no longer one-dimensional, but instead two-dimensional. The Hopf bifurcation typically marks a transition from a steady state to an unsteady periodic state, or more precisely a limit cycle, where the imaginary part gives the frequency for the linearized system, $\Im(\lambda_m) = 2\pi f$, where f is the frequency.

For more details regarding bifurcation analysis one may refer to e.g. Seydel [63].

Examples for fluid flow

The canonical example when considering bifurcation analysis is the flow past a circular cylinder. The flow becomes globally unstable at a critical Reynolds number $45 \leq Re_{cr} \leq 47$ ($\gamma = Re$), after which the global mode starts to grow exponentially, with an amplitude that finally saturates through nonlinear effects giving the well-known von Karman vortex street. A representation of a von Karman street, for $Re = 400$, can be seen in Fig. (2.10). The figure shows the time evolution of the flow structure, where at least two images are needed to capture the downstream transport. However, the single frequency nature ($St \approx 0.24$) of the mode should serve as an indication that the full von Karman street is not captured. Note that three dimensional flow effects, for the flow around a cylinder, start to play a role at $Re \sim 200$ and above.

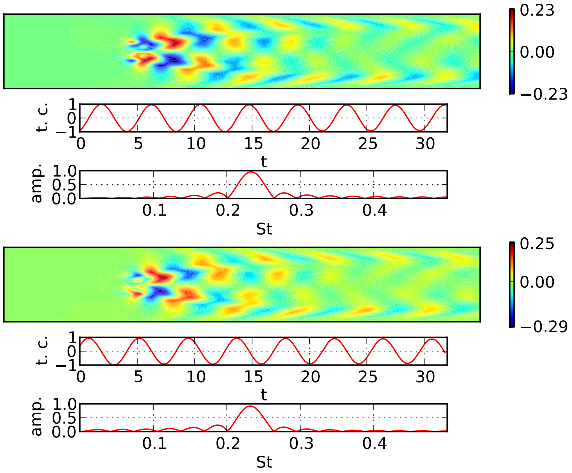

Figure 2.10: Axial component of a flow mode representing the von Karman street behind a stationary cylinder. The time coefficients (t. c.) represent the time variation of the strength of the mode. The incoming base flow, from left to right, is of top hat character with (normalized) axial velocity $U^* = 1$.

For the flow past a cylinder, a separation may be made between structures arising from the wake and possible boundary layer instabilities, where the von Karman vortex street is a consequence of the wake profile. The von Karman shedding comes from a supercritical Hopf bifurcation, and the amplitude of oscillation follows a Landau equation. The Landau equation gives a saturated oscillation amplitude which, for $Re \gtrsim Re_{cr}$, scales as

$$A_{sat} \propto \sqrt{Re - Re_{cr}},$$

as well as a nonlinear correction to the oscillation frequency seen during the linear growth. The saturation amplitude A_{sat} could be, e.g., the axial velocity fluctuation at some point in the wake. Thus, the amplitude (not regarding the phase factor) looks like it traces a supercritical pitchfork bifurcation, the (positive upper branch of the) scenario shown to the right in Fig. (2.9). A saturation amplitude following this trend (as the control parameter is varied) constitutes strong evidence for the existence of a supercritical Hopf bifurcation. However, an even more ambitious study would include the transient behaviour, from linear growth to nonlinear saturation. When checking whether or not a given oscillation is a self-sustained process, like for the flow past a cylinder, the amplitude for every point in the flow (experimental or numerical) needs to follow the *same* Landau equation (same coefficients) [22].

The PVC, in an experimental setup of a swirling flow experiencing a sudden expansion, has been seen to be a supercritical Hopf bifurcation [46]. The amplitude of oscillation, at the same Reynolds number (based on the axial flow), was seen to scale as

$$A_{sat} \propto \sqrt{Sw - Sw_{cr}}$$

for the swirl number Sw ($\gamma = Sw$). This implies that the structure seen in Fig. (2.5) is a self-sustained oscillating structure, in a way analogous to the von Karman shedding.

Examples of transcritical bifurcations can be found in inviscid studies of *vortex breakdown*, while turning point bifurcations can be found in corresponding viscous studies [34, 79, 35, 33, 78]. The bifurcation parameter in these cases is the swirl level (at a given Reynolds number), while the vertical axis may represent the minimum axial velocity along the centre axis of the flow domain (which should be negative for bubble-like vortex breakdown, by definition). From the sketch of the turning point bifurcation to the left in Fig. (2.9), as the swirl level is increased beyond the critical value, the solution will abruptly "fall down" to a solution with a reversed flow on (parts of) the centre axis.

However, for low Reynolds number swirling pipe flows, both with and without a sudden expansion, the transition to vortex "breakdown" as the swirl level is increased is gradual, and no turning point bifurcation is present. The critical swirl level is furthermore seen to get *larger* for larger Reynolds numbers for swirling flows in straight pipes, while the critical swirl level is seen to get *smaller* for larger Reynolds numbers for pipes with a sudden expansion [54]. The physical reason behind this behaviour is believed to be the diminishing swirl strength in the shear layers of the sudden expansion, which is more pronounced for smaller axial bulk velocities (with the Reynolds number defined in terms of the axial bulk flow). Keep in mind that these are only rough trends, and that the evolution of these flows cannot be determined by knowing just two numbers (the Reynolds number and the swirl number) [36].

2.2.6 Transition and strong nonlinearity

The transition from laminar to turbulent flow in general appears to be more rapid in flows which may be inviscidly unstable, such as jets and wakes, than in wall-bounded flows without an adverse pressure gradient (no inflection point). Even for channel flow with a Reynolds number above the critical, the growth rates are modest. The transition to turbulence in these cases, with a Reynolds number above the critical, begin with TS waves and are said to take the "natural path". Other routes to turbulence in zero-pressure gradient (ZPG) wall-bounded flows are called *bypass transitions*, which is a term that not always includes linear transient growth. These are transition scenarios which rely on the specific nature of the incoming disturbances.

Landau's idea for transition was that the type of primary instability following his equation, introducing a frequency into the flow, would be followed by a secondary instability (analysed using Floquet theory) introducing a second frequency. These bifurcations would continue and eventually enough frequencies would have been introduced for the flow to be considered turbulent. However, this idea was superseded by the advent of *chaos*, where it was discovered that *only very few* bifurcations were needed before the flow became turbulent. This was a lesson which came about by studying *closed* flows, in particular Taylor-Couette flow [17].

Investigations of strongly nonlinear instabilities include simulations of the full Navier-Stokes equations, perhaps together with POD and/or DMD for post-processing. Another approach is to look at the fluctuation energy K_Ω,

$$K_\Omega = \int_\Omega \frac{1}{2} u_i' u_i' dV,$$

where the fluctuating velocity components are integrated over the domain Ω. Multiplying eq. (2.14) by u_i', summing over i and integrating over Ω, one obtains

$$\frac{dK_\Omega}{dt} = \int_\Omega u_i' \frac{\partial u_i'}{\partial t} dV = -\int_\Omega u_i' u_j' \frac{\partial U_i}{\partial x_j} dV - \nu \int_\Omega \frac{\partial u_i'}{\partial x_j} \frac{\partial u_i'}{\partial x_j} dV, \tag{2.17}$$

given that the domain is static, and that the fluctuations either vanish at the boundaries ($\partial\Omega$) or the boundary conditions are periodic [13]. Equation (2.17) (in its dimensionless form) is called the *Reynolds-Orr equation.* Note that no assumptions have been made regarding the size of the fluctuations, and that, since the third order terms vanish (because they only redistribute energy), the equation is in fact independent of the scale of the fluctuations. As was pointed out by Tsinober [73], the same is not true for the velocity derivatives, i.e. the corresponding equations for the fluctuations of the vorticity and the strain rate both include third order terms. Also note that the first term on the right hand side of eq. (2.17) represents a transfer of energy between the base flow and the fluctuations, and that the second term, the viscous term, is always non-negative i.e. dissipative. Considering a *strict monotonic* decrease in the fluctuation energy, $dK_\Omega/dt < 0$, K_Ω may be regarded as a Lyapunov functional. Such a way of determining stability properties is called an *energy method*, and eq. (2.17) may be seen as setting a restriction on the Reynolds number. The restriction to monotonic decrease when determining stability, however, is typically too strong to be useful, which should be even further emphasised when the continuity equation for the fluctuations, eq. (2.15), is not fulfilled.

2.3 Turbulence

The archetypal turbulent flows basically make up three groups, grid-like flows, free-shear flows (mixing layers, jets, wakes), and wall-bounded flows [50]. However, the different types are of course often seen, typically interacting, in a single system (not least in industry). What separates so-called "grid turbulence", with a vanishing or spatially nonvarying base (mean) flow, from the rest is that it is not self-sustaining, and eventually disappears if left to its own devices. This can be seen in eq. (2.17), where the first term on the right hand side (the production term) vanishes. Due to the elusive nature of turbulence in fluid flow, no consensus regarding its definition has emerged. In fact, the level of theoretical progress made from first principles (i.e. the Navier-Stokes equations) is *extremely* limited. Even the very question(s) to be answered appears to be difficult to pin down. However, some qualitative features exist, around which there is little dispute, that should be fulfilled for *all* turbulent flows.

- Long-term unpredicatability and apparent spatio-temporal randomness, both intrinsic to the system
- Three-dimensional flows with a high degree of strain/dissipation and vorticity
- Strongly diffusive, with enhanced transport of momentum, energy, etc.
- Wide range of length and time scales, with many interacting degrees of freedom

Because of the inherent difficulties in treating turbulent flows, a lot of focus has been placed on phenomenological aspects, such as categorizations of length and time scales. The notion of a *smallest* length scale, through ideas put forward by Kolmogorov, is a length scale below which dissipative effects completely dominate, thereby effectively removing any variation on scales below it. However, the very term 'scale' is unfortunately not well defined, rather being an appeal to ones intuition, but is often considered in terms of Fourier modes. The smallest scale was proposed to depend *only* on the kinematic visocity ν and the dissipation rate per unit of mass ϵ. Through a dimensional analysis the so-called

Kolmogorov length scale l_η is obtained,

$$l_\eta = \left(\frac{\nu^3}{\epsilon}\right)^{1/4}.$$

Thus, the claim is that the (mathematically) infinite dimensional velocity field u_i actually has a smallest length scale l_η. Comparing l_η to the integral length scale l_o, roughly on the order of the geometrical constrictions, assuming an energy transfer rate $\epsilon \sim u_\eta^3/l_\eta \sim u_o^3/l_o$, gives

$$\frac{l_o}{l_\eta} \sim \frac{l_o}{\left(\nu^3 l_o/u_o^3\right)^{1/4}} = \left(\frac{u_o l_o}{\nu}\right)^{3/4} = Re_{l_o}^{3/4}. \tag{2.18}$$

Therefore, as the Reynolds number increases, a substantial increase in the number of degrees of freedom should be expected. However, it should be noted that ϵ may vary substantially, not just in space, but also in time.

Kolmogorov furthermore brought forward the idea that, for large Reynolds number ($l_o \gg l_\eta$), there should be a range of scales independent of both the geometry/large scale (l_o) features of the flow *and* the viscosity ν. The flow evolution over this range of scales was expected to be a transfer of energy, with a very low level of dissipation, from the large scales (l_o) to the small scales (l_η). The distribution of fluctuation energy K over this range of scales, called the *internal subrange*, was therefore argued to *only* depend on the dissipation rate ϵ and wave number κ, giving

$$K \propto \epsilon^{2/3}\kappa^{-5/3},$$

again based on dimensional considerations. The inertial subrange together with the dissipative scales are often referred to as the *universal equilibrium range* because of their (supposed) independence from the large scales. The universal equilibrium subrange ties in to the notion of a *turbulence cascade*, with a unidirectional transfer of energy from large scales to small scales, and finally to heat. A schematic of the different regions are shown in Fig. (2.11), where P (production) represents the first term on the right hand side in eq. (2.17). The figure tries to represent a generic situation where energy is being fed into the system through the largest scales.

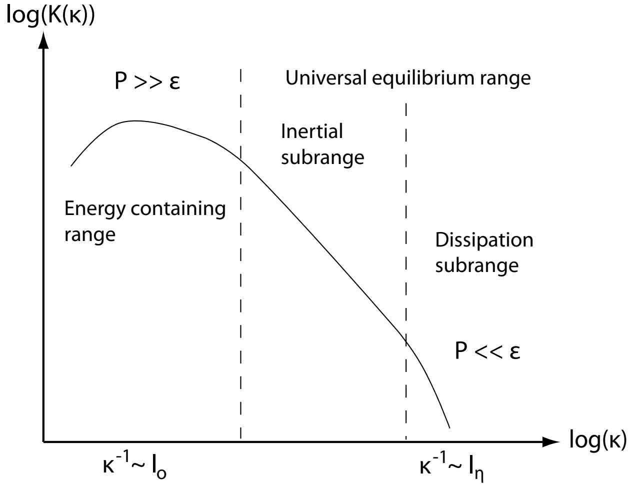

Figure 2.11: Turbulence energy distribution over wavenumbers κ.

It is important to keep in mind that the above separation into different wavenumber regions is only based on phenomenology. For example, the existence of any universality in turbulence is far from clear. Note also that, since turbulence is such a complex phenomenon, it cannot, by any means, be exhausted by such a thing as e.g. an energy spectrum. However, from an engineering point of view, leaving aside the fundamental aspects, many of these problems can often be avoided with rather good results in terms of statistical flow data.

More general information regarding turbulent flow can be found in e.g. Pope [52], with more conceptual issues treated in Tsinober [73, 74].

Chapter 3

Stability analysis - methodology

Linear stability analysis has long served as a tool to study the stability properties of nonlinear systems. This has typically meant the evolution of infinitesimal disturbances on given steady, often simple, base flow. In a step further, stability analysis also lends itself quite readily to periodically varying base flow, where one may follow changes in a stroboscopic manner at a time interval equal to the period. The desire to extend the methods of stability analysis beyond that of steady and periodic base flow of course exists, and is driven by the real world, where a turbulent flow is the rule rather than the exception. For example, the idea of looking at *linear* stability properties of *mean* flow has been found to yield good results in some cases, while not in others [65], and still lacks a rigorous foundation.

Rising use of experimental methods such as high-speed *particle image velocimetry* (PIV), giving velocity fields along planes, sparks interest in post-processing methods for snapshot sequences, since boosting the sampling rate for the laser/camera systems typically is of *no use* if the goal is to obtain statistical quantities. In fact, it may even have negative effects because of the possibility of an increased correlation between the samples. For experimental studies, where no governing equations are known, *data-based* as opposed to *model-based* procedures for extracting dynamic information become necessary.

Among the primary interests in this thesis is global *nonlinear* stability analysis, where the full Navier-Stokes equations are used, whereafter the results are processed using one or both of the data-based decomposition methods *proper orthogonal decomposition* (POD) [37, 66] or *dynamic mode decomposition* (DMD) [55, 61]. While POD is a statistical method, DMD is a stability analysis tool with connections to linear global modes. The need for such methods is often crucial, especially for numerical simulations where the amount of data to process can be immense. Methods for extracting linear global modes are discussed in Section (3.1), after which a certain approach to the complimentary linear transient growth analysis is introduced in Section (3.2). A review of POD analysis is given in Section (3.3), and the more recent DMD analysis makes up Section (3.4.1).

3.1 Global linear instability

This section focuses on TriGlobal mode analysis, where no assumptions regarding the homogeneity of the base flow is made. After linearization, eq. (2.14) turns into

$$-u'_j \frac{\partial U_i}{\partial x_j} - U_j \frac{\partial u'_i}{\partial x_j} - \frac{\partial p'}{\partial x_i} + \nu \frac{\partial^2 u'_i}{\partial x_j \partial x_j} = \frac{\partial u'_i}{\partial t} \tag{3.1}$$

with

$$\frac{\partial u'_j}{\partial x_j} = 0 \tag{3.2}$$

where $U_i = U_i(x, y, z)$ represents the base flow while u'_i and p' are the fluctuations being solved for. Solving for eqs. (3.1) and (3.2) directly, given some initial fluctuation field and appropriate boundary conditions, may be called linear global *nonmodal* analysis. Letting u'_i and p' have an exponential time dependence, $u'_i(x, y, z, t) = \widetilde{u}'_i(x, y, z)e^{\lambda t}$ and $p'(x, y, z, t) = \widetilde{p}'(x, y, z)e^{\lambda t}$, eq. (3.1) turns into

$$-\widetilde{u}'_j \frac{\partial U_i}{\partial x_j} - U_j \frac{\partial \widetilde{u}'_i}{\partial x_j} - \frac{\partial \widetilde{p}'}{\partial x_i} + \nu \frac{\partial^2 \widetilde{u}'_i}{\partial x_j \partial x_j} = \lambda \widetilde{u}'_i. \tag{3.3}$$

The eigenvectors $\widetilde{u}'_i$ and $\widetilde{p}'$ to eqs. (3.2) and (3.3), together with appropriate boundary conditions, are called linear *global modes* [71]. The mode with the largest real part $\Re(\lambda)$, given that the (initial) fluctuation field has a nonzero projection on the corresponding eigenvector, will dominate after a sufficiently long time. Especially, if $\Re(\lambda) > 0$, the mode(s) will grow exponentially. Of course, if the fluctuations grow large, nonlinear effects will start to become important. However, for a non-normal Jacobian, a superposition of the different global modes, or perhaps rather solutions to eqs. (3.1) and (3.2) given some initial fluctuation field, can lead to substantial fluctuation growth even if all global modes decay, $\Re(\lambda) < 0$ [60]. More on this in Section (3.2).

A possible method to solve for the corresponding, typically very large, *discretized* eigenvalue problem is to use the *Arnoldi method*, Section (3.1.1), or perhaps the improved *implicitly restarted Arnoldi method*, Section (3.1.2).

3.1.1 Arnoldi method

The $N \times N$ matrix governing the evolution will be denoted by A. Since N is generally very large, ordinary methods for calculating eigenvalues, such as the QR method, are not readily applicable. Therefore, some more appropriate procedures are needed. For example, in the power iteration procedure, A is repeatedly applied to an initial vector x in order to obtain the eigenvalue with the largest magnitude [57]. More generally, a function f of A can be considered, where the power iteration procedure gives the eigenvalue of $f(A)$ with the largest magnitude. However, using power iteration, a lot of information is discarded. Instead, one can make use of the intermediate vectors by constructing the subspace

$$K_m(A, x) = \text{span}\left\{x_0 = x, x_1 = Ax, ..., x_{m-1} = A^{m-1}x\right\}$$

which is called a *Krylov subspace*. Note that no matrix-matrix multiplications are needed. For the *Arnoldi method* an orthonormal basis is created for the Krylov subspace, by making use of the Gram-Schmidt procedure. With $\langle \cdot, \cdot \rangle$ denoting an inner product, the algorithm looks as follows:
Make an initial guess $v_1 = x$, then for $j = 1$ to m

1. Form
$$R^{[j]} = Av_j$$
2. Compute Gram-Schmidt coefficients
$$h_{ij} = \langle v_i, R^{[j]} \rangle, \quad \text{i = 1, 2, ..., j}$$
3. Remove previously spanned directions
$$q_j = R^{[j]} - \sum_i^j h_{ij} v_i$$
4. Compute the norm
$$h_{j+1,j} = \langle q_j, q_j \rangle^{1/2}$$
5. Normalize
$$v_{j+1} = \frac{q_j}{h_{j+1,j}}$$

The elements h_{ij} are collected in the matrix

$$(\underline{H}_m)_{ij} = \begin{cases} h_{ij} & \text{for } i = 1, 2, .., m+1,\ j = 1, 2, ..., m \\ 0 & \text{filling the rest of the } (m+1) \times m \text{ matrix} \end{cases}$$

This leads to

$$AV_m = V_m \underline{H}_m$$

or

$$AV_m = V_m H_m + h_{m+1,m} v_{m+1} e_m^T \tag{3.4}$$

where the upper Hessenberg matrix H_m are the first m rows of $\underline{H}_m$, the matrix $V_m = [v_1\ v_2\ ...\ v_m]$, and the column vector $(e_m)_i = \delta_{im}$. Applying V_m^T from the left on eq. (3.4) gives

$$V_m^T A V_m = V_m^T V_m H_m + V_m^T h_{m+1,m} v_{m+1} e_m^T = H_m$$

since $\{v_i\}_{i=1}^{m+1}$ are all orthonormal by construction. Thus, H_m is the projection of A onto the m-dimensional Krylov subspace $K_m(A, x)$. If the residual, the second term on the right hand side in eq. (3.4), becomes "small", the eigenpairs of H_m, $H_m y = \sigma y$, are approximate eigenpairs of A,

$$A(V_m y) = (AV_m)y \approx (V_m H_m)y = V_m(H_m y) = V_m(\sigma y) = \sigma(V_m y).$$

Thus, if it is possible to neglect the residual, H_m and A share eigenvalues, called the Ritz (eigen)values, while the eigenvectors, the Ritz (eigen)vectors, are related through the product $V_m y$. The problem of solving an eigenvalue problem of an $N \times N$ matrix is thereby reduced to that of an $m \times m$ Hessenberg matrix, which can be a huge win since typically $N \gg m$. If the residuals are deemed too large the subspace is expanded, V_{m+1}, V_{m+2}, and so on, until a satisfactory level is reached. Especially note that the residual for eigenpair (σ_i, y_i),

$$h_{m+1,m} v_{m+1} e_m^T y_i$$

is small for all i if $h_{m+1,m}$ is small. Unfortunately, not very much is known in general about the convergence properties of the Arnoldi method.

3.1.2 Implicitly restarted Arnoldi method

For large m the eigenvalue problem for the Hessenberg matrix H_m, typically solved using the QR method, may become prohibitively expensive. Additionally, having to keep a lot of the vectors $\{v_i\}$ orthogonal, and retaining a lot of vectors in memory, are unfortunate features of the standard Arnoldi algorithm. A way to avoid these features is by introducing the notion of *restarting* the process by creating a more appropriate starting vector v_1. The basic idea behind the *implicitly restarted Arnoldi* (IRA) algorithm is to filter out unwanted "eigendirections" from the original starting vector (v_1) by using the most recent spectral information together with a clever filtering technique.
Let m be the number of eigenvalues that are desired. Use the Arnoldi algorithm to find M ($M > m$) approximate eigenvalues of A, $\{\sigma_i\}_{i=1}^M$, from

$$AV_M = V_M H_M + h_{M+1,M} v_{M+1} e_M^T, \tag{3.5}$$

where the eigenvalue estimates are ordered such that the leading ones have some specific property, e.g. $\Re(\sigma_i) \geq \Re(\sigma_j)$ for $j > i$. The goal is to filter out the directions of the eigenvectors $\{y_i\}_{i=m+1}^M$ from the starting vector. For example, trying to filter out y_{m+1}, subtract $\sigma_{m+1} V_M$ from eq. (3.5),

$$(A - \sigma_{m+1} I)V_M = V_M(H_M - \sigma_{m+1} I) + h_{M+1,M} v_{M+1} e_M^T$$

and construct the QR decomposition

$$Q^{(1)} R^{(1)} = H_M - \sigma_{m+1} I.$$

Multiplying with $Q^{(1)}$ from the right to get

$$(A - \sigma_{m+1} I)V_M Q^{(1)} = (V_M Q^{(1)})(R^{(1)} Q^{(1)}) + h_{M+1,M} v_{M+1} e_M^T Q^{(1)}$$

leads one to finally write

$$AV_M^{(1)} = V_M^{(1)} H_M^{(1)} + h_{M+1,M} v_{M+1} e_M^T Q^{(1)}$$

where $V_M^{(1)} \equiv V_M Q^{(1)}$ and $H_M^{(1)} \equiv R^{(1)} Q^{(1)} + \sigma_{m+1} I$. Thus, the method is based on a shifted QR algorithm, which preserves the Hessenberg form, giving a *new* Arnoldi decomposition *which is equivalent to the decomposition that would have been obtained if the Arnoldi process was initiated with the filtered vector.* The algorithm looks as follows:

1. Compute the M eigenvalues of H_M $(m < M \ll N)$
2. Apply the shifted QR algorithm $M - m$ times, with shifts σ_{m+1}, σ_{m+2}, ..., σ_M, to compute a new Arnoldi decomposition with a filtered starting vector
3. Go back to 1 if the (m) wanted eigenpairs have not converged

Matrix transformations are often needed to select eigenpairs when the wanted eigenvalues are not the ones with the largest magnitude. Another reason for needing matrix transformations is that eigenvalues that are not *well separated* may lead to slow convergence of the algorithm, or even convergence to the wrong eigenvalues.

3.2 Optimal linear transient growth

Consider the time evolution of the fluctuation field u', governed by eqs. (3.1) and (3.2),

$$u'(t) = \mathcal{A}(t) u'(0).$$

Here the interest is in the *maximum energy growth of any initial fluctuation field, $u'_0 \equiv u'(0)$, after some time t.* Again, note that even if all the eigenmodes of a system are decaying, as given in Section (3.1), a superposition of some of the modes may still give rise to large fluctuations $u'(t)$ in the short term [60]. Consider $||u'_0||^2 \equiv \langle u'(0), u'(0) \rangle = 1$, using an inner product $\langle \cdot, \cdot \rangle$, and the relative energy at time t becomes

$$K(t) = \langle u'(t), u'(t) \rangle = \langle \mathcal{A}(t) u'_0, \mathcal{A}(t) u'_0 \rangle = \langle u'_0, \mathcal{A}^*(t) \mathcal{A}(t) u'_0 \rangle$$

after introducing the adjoint operator $\mathcal{A}^*$ (which is usually calculated using partial integration in the infinite dimensional case). The Euclidian inner product, considering the finite dimensional discrete (matrix) problem, gives

$$K(t) = (u'_0)^T \mathcal{A}^T(t) \mathcal{A}(t) u'_0.$$

Thus, the interest is in the eigenvalue decomposition of $\mathcal{A}^T(t)\mathcal{A}(t)$, and particularly the eigenvalue λ_i with the largest magnitude together with its accompanying normalized eigenvector w_i. This would then give the largest possible increase in energy any disturbance could have gained after a time t. It may also be recognized that the (full) *singular value decomposition* (SVD) of $\mathcal{A}(t)$ could be considered instead,

$$\mathcal{A}(t)w_i = (\lambda_i)^{1/2}v_i.$$

Here not only the energy increase is seen, but also how the spatial structure of the initial fluctuation field w_i has evolved into v_i after time t.

3.3 Proper orthogonal decomposition

Proper orthogonal decomposition may be seen as an optimal way of compressing a sequence of data. For a flow field, this implies the extraction of the most energetic flow structures. Consider the set of time dependent quantities $\{u_i(t)\}_{i=1}^N$, which in this thesis will be (three-component) velocities, possibly with the mean values subtracted, at $N/3$ spatial sample points. The method is based on a correlation matrix M

$$M_{ij} = \langle u_i u_j \rangle \tag{3.6}$$

where $\langle \cdot \rangle$ will refer to time averaging. Eigenvectors corresponding to the largest eigenvalues of the matrix (3.6) reflect the *most energetic* "directions" and the regions with the *strongest correlations*. This eigenvector decomposition has a whole plethora of different names, one of them being *proper orthogonal decomposition* (POD). The matrix M is seen to contain a set of two-point correlations, which may be obtained using two hot-wire probes collecting data simultaneously at two different spatial locations. However, today data is often sampled simultaneously over a range of space, such as over a 2-D plane for PIV (or possibly 3-D for tomographic PIV) or over a 3-D domain for DNS/LES/(U)RANS. An alternative method, less computationally expensive than calculating eigenpairs for the $N \times N$ matrix M, called the *method of snapshots* [66], is presented below.

Consider the set of vectors $\{u(t_k)\}_{k=1}^m$, $u(t_k) \in \mathbb{R}^N$. Placing the vectors in a matrix U,

$$U \equiv [u(t_1)\, u(t_2)\, \ldots\, u(t_m)] \in \mathbb{R}^{N \times m},$$

an $N \times N$ correlation matrix (neglecting the scaling factor m^{-1}) can be formed,

$$(UU^T)_{ij} = \sum_{k=1}^{m} u_i(t_k) u_j(t_k), \tag{3.7}$$

where $(UU^T)_{ij} = mM_{ij}$ if m is large enough. The (thin) SVD may be considered for calculating the eigenpairs of (3.7),

$$U = V\Sigma W^T \tag{3.8}$$

where $V \in \mathbb{R}^{N \times m}$ and $W \in \mathbb{R}^{m \times m}$ are orthonormal matrices and $\Sigma \in \mathbb{R}^{m \times m}$ is a diagonal matrix with nonnegative entries. Thus, instead of solving the (generally large) eigenvalue problem for $UU^T = V\Sigma^2 V^T$, the (generally small) eigenvalue problem for $U^TU = W\Sigma^2W^T$ may be solved, and $V = UW\Sigma^{-1}$. The existence of an invertible Σ requires that the columns of U ($\{u(t_k)\}_{k=1}^m$) are linearly independent. The eigenvectors of (3.7), the POD modes, are the columns v_i of V with the corresponding eigenvalues $\sigma_i^2 \equiv \Sigma_{ii}^2$. Thus, the matrix (3.7) (which is symmetric positive semidefinite) gives orthogonal eigenvectors with real nonnegative eigenvalues, which are sorted so that $\sigma_1^2 \geq \sigma_2^2 \geq ... \geq \sigma_m^2$.

The (normalized) POD basis $\{v_i\}_{i=1}^m$, $v_i \in \mathbb{R}^N$, is optimal (or "proper") in the sense that, given any trunction limit $q \in \mathbb{N}$ ($q \leq m$), the expression

$$\sum_{k=1}^{m} ||u(t_k) - \sum_{i=1}^{q} \tilde{a}_i(t_k)\tilde{v}_i||_2^2$$

is minimized (for the l^2-norm) when $\tilde{v}_i = v_i$ and $\tilde{a}_i(t_k) = a_i(t_k)$, where the coefficients $a_i(t_k)$ are simple projections,

$$a_i(t_k) \equiv v_i^T u(t_k). \tag{3.9}$$

The values $a_i(t_k) \in \mathbb{R}$ are referred to as the *time coefficients.* Considering the trace of (3.7) it is seen that, with $\langle u_i^2 \rangle = \frac{1}{m}\sum_{k=1}^m u_i^2(t_k)$,

$$m\sum_{i=1}^{N}\langle u_i^2 \rangle = \sum_{i=1}^{m}\sigma_i^2,$$

which follows since the rest of the $N - m$ eigenvalues of matrix (3.7) are zero valued. Thus, the eigenvalues are related to the mean "energy" of the field, which becomes actual (kinetic) energy when u represents a velocity field. In cases where fluctuations ($u \rightarrow u'$) are considered, it of course instead corresponds to the mean fluctuation energy.

Decisions about how many modes to consider may be based on the fraction of the total energy to be captured. As for any successful modal decomposition, the number of relevant modes should be small. The typical expectation is that the most energetic modes should represent large scale structures (which is not necessarily true) and that modes of lower energy should represent smaller scale structures, or "noise", which are typically ignored. A partial reconstruction of a field using POD modes may then act as a low pass filter.

Given that the fields $u(t_k)$ were sampled at a fixed time interval, which is otherwise not necessary, the time coefficients can easily be used to extract the frequency content of the modes. A better frequency analysis may even be obtained for the time coefficients compared to using point data in the flow field, since the decomposition can work as a filter. The POD modes, in contrast to DMD modes, may contain multiple frequencies. Note that the sampling interval has to be taylored for the specific flow frequencies that are of interest. It may especially be mentioned that for modes of a *traveling wave* character, often two close lying (in terms of eigenvalues/energy content) modes are found, which are phase shifted 90° from one another in time, seen in the time coefficients. A traveling wave is on the other hand captured in only one mode for a DMD analysis (a DMD mode gives two fields, one ”real” and one ”imaginary”). Note that for a standing wave only one field is necessary, for both POD (one mode) and DMD (real *or* imaginary part gives large values).

Also considering the columns of W in eq. (3.8), which are orthonormal as well, results in what is called a *bi-orthogonal decomposition* (BOD) of U. The columns of W are known to correspond to the eigenvectors of

$$(U^T U)_{ij} = \sum_{k=1}^{N} u_k(t_i) u_k(t_j). \tag{3.10}$$

Thus, for eq. (3.7), *spatial* correlations are considered (where time is averaged out), whereas for eq. (3.10), *temporal* correlations are considered (where space is averaged out). The columns of V (the POD modes) are in this context called the *topos* and the columns of W the *chronos*. The chronos modes are furthermore proportional to the time coefficients, implying that the time coefficients for different modes are orthogonal ($a_i^T a_j = 0,\ i \neq j$). In the next section DMD analysis is considered, which may be viewed as a complement to POD analysis.

3.4 Koopman analysis

Koopman modes, for nonlinear dynamics, may be thought of as the analogue of normal modes for linear dynamics [40]. The Koopman operator for nonlinear systems is a linear operator, which does not involve linearization. However, the price to pay is that the Koopman operator is infinite dimensional. Consider the dynamical system

$$\dot{z} = f(z)$$

on the state space M ($z \in M$), where f in general is nonlinear. For a state z, denote the solution at a time t later by $S^t z$. Introduce the *observable* $g : M \to \mathbb{R}^p$, which may give e.g. a section of the flow field as its codomain. The Koopman operator K^t is then defined by

$$K^t g(z) = g(S^t z).$$

The spectral properties of K^t are of particular interest. In the context of a sequence of fields $\{u(t_i)\}_{i=1}^{\infty}$, with $t_{i+1} = t_i + \Delta t$, the Koopman operator $K \equiv K^{\Delta t}$ is given by $Ku(t_i) = u(t_{i+1})$. Considering the sequence $U \equiv [u(t_1)\, u(t_2) \ldots]$, this can in turn be written as

$$KU = US$$

for the infinite dimensional shift operator S,

$$S = \begin{bmatrix} 0 & 0 & 0 & \ldots \\ 1 & 0 & 0 & \ldots \\ 0 & 1 & 0 & \\ \vdots & & \ddots & \ddots \end{bmatrix}.$$

Since the spectral properties of S are not attainable, an approximation to the Koopman operator is given by Dynamic mode decomposition.

3.4.1 Dynamic mode decomposition

Dynamic mode decomposition (*DMD*) is a recently developed (Rowley *et al.* [55], Schmid [61]) data-based method for extracting dynamic information from a data set sampled at a fixed temporal(/spatial) interval. While POD modes are separated out based on their energy content, DMD modes are separated out based on their frequency and rate of growth/decay.

Consider a set of (column) vectors $\{u_k\}_{k=1}^{m}$, $u_k \equiv u(t_k) \in \mathbb{R}^N$, sampled at a fixed time interval Δt, with all but the last one placed in the matrix U_1^{m-1},

$$U_1^{m-1} \equiv [u_1\, u_2\, \ldots\, u_{m-1}] \in \mathbb{R}^{N\times m-1}.$$

Proceed by writing the last vector as a linear combination of the previous $m-1$ vectors, assuming that they are linearly independent, plus some residual term,

$$u_m = \sum_{k=1}^{m-1} c_k u_k + r.$$

The weights c_k are obtained through a least square calculation so as to minimize the residual r. The hope is that m is sufficiently large so that the residual can be neglected. Letting A denote the matrix that leads from one state to the next, $u_{k+1} = Au_k$, gives

$$AU_1^{m-1} = U_1^{m-1}C + re_{m-1}^T \tag{3.11}$$

for the so-called companion matrix C,

$$C = \begin{bmatrix} 0 & 0 & \ldots & 0 & c_1 \\ 1 & 0 & & 0 & c_2 \\ 0 & 1 & & 0 & c_3 \\ \vdots & & \ddots & & \vdots \\ 0 & 0 & \ldots & 1 & c_{m-1} \end{bmatrix} \tag{3.12}$$

and $(e_{m-1})_i = \delta_{i,m-1}$. Note that A is a finite dimensional approximation to K. The Arnoldi procedure and eq. (3.4), which is an orthonormal decomposition with its accompanying Hessenberg matrix, may be compared with that of eq. (3.11), where some of the columns of U_1^{m-1} can be almost parallel. The problem now becomes one of finding eigenpairs ($\sigma_i \in \mathbb{C}, x_i \in \mathbb{C}^{m-1}$) for the matrix $C \in \mathbb{R}^{m-1\times m-1}$,

$$Cx_i = \sigma_i x_i. \tag{3.13}$$

The (approximate) eigenvectors of A, $U_1^{m-1}x_i$, are called *dynamic/DMD modes*. The associated eigenvalues can in turn be written as $\sigma_i \equiv e^{\lambda_i \Delta t}$. Here one may consider the imaginary part $\Im(\lambda_i) = 2\pi f_i$, for the frequency f_i, while the real part $\Re(\lambda_i)$ determines the growth/decay rate. A concern about this method of extracting dynamic modes is that the companion matrix (3.12), because of its (sparse) structure, may be very sensitive to noise. Another method was proposed (Schmid [61]) which is based on the (thin) SVD

$$U_1^{m-1} = V\Sigma W^T,$$

where the columns of $V \in \mathbb{R}^{N\times m-1}$ are the POD modes of U_1^{m-1}. The equation $AU_1^{m-1} = U_2^m$ gives

$$AV\Sigma W^T = U_2^m \Rightarrow V^T AV = V^T U_2^m W\Sigma^{-1} \equiv \widetilde{C}$$

given that Σ is invertible (all the singular values are positive), which is the case if the columns of U_1^{m-1} are linearly independent. Since $V^T(AV)$ represents a projection of A onto the column space of V (and therefore onto the column space of U_1^{m-1}) there is no residual involved in the expression. In this case the eigenvalue problem to solve is

$$\widetilde{C} y_i = \sigma_i y_i.$$

In contrast to the companion matrix C, the matrix $\widetilde{C}$ is in general full. The dynamic modes from the companion matrix approach are proportional to Vy_i. In the software that was used for this thesis, both the methods could be applied, and the modes were ranked according to their magnitudes $||U_1^{m-1}x_i||_2$, with the normalization

$$||x_i||_2^2 = \sum_{j=1}^{m-1} |(x_i)_j|^2 = \Re(x_i)^T \Re(x_i) + \Im(x_i)^T \Im(x_i) = 1$$

(of the eigenvectors in (3.13)). The same normalization ($||x_i||_2 = 1$) was used for the SVD approach. The magnitudes only have meaning relative to each other, and the mode with the largest magnitude often comes to reflect the mean flow. Thus, the choice of important modes can be based on the relative magnitudes of the modes, the frequencies, and the rates of growth/decay.

If A is a linear operator DMD analysis reduces to a linear stability analysis, while for periodic flow, with $u_m = u_1$, DMD reduce to a discrete Fourier transform ($\lambda_k = 2\pi ik/(m-1)$). Perhaps more surprisingly, if the mean is removed, $u_i \rightarrow u_i - m^{-1}\sum_{k=1}^{m} u_k$, $i = 1, 2, ..., m$, DMD also reduces to a discrete Fourier transform [9]. The real parts $\Re(\lambda_i) = 0$, $\forall i$, and the frequencies $\Im(\lambda_i)/2\pi$ come in steps of $\Delta f = 1/(m\Delta t)$. The lowest frequency to be captured becomes $1/(m\Delta t)$, where there is otherwise no theoretical lower bound. Furthermore, the mode energies might drop of slowly for non-periodic data, along with other (well-known) restrictions for the DFT.

Decompositions for more general cases, not considering a linear operator or a periodic flow, are up for interpretation. DMD analysis lends itself particularly well to cases where only a few dominant frequencies are present in the flow. Note that while POD modes may largely separate different frequencies in certain circumstances, it does not do so by design. Difficulties arise when there are no dominating frequencies in the flow. This can especially be the case for very turbulent flows where there is a large variability in the frequency content, and where structures, for example, appear in bursts at irregular intervals. Since the growth/decay rates ($\Re(\lambda_i)$) can be very sensitive to this type of "noise", only *relative* values are usually considered.

The SVD approach was used for all of the cases in this thesis, except for the VT40 burner. The main reason for this was based on the code, where the SVD approach did not require all of the data to be read into memory at once. However, for all of the cases and tests where the SVD and companion matrix approaches for calculating the DMD were compared, they gave nearly identical results.

The way a DMD and/or POD analysis was typically performed, was to first obtain time sequences of the quantity of interest at some different points in the flow. Based on the frequencies that were extracted, a decision was made regarding how often to sample, and for how long. Note that both DMD and POD are subject to the Nyquist criterion. As already mentioned, DMD is a fairly new method, and more guidelines are needed.

3.4.2 Extended DMD

To be able to couple different fields, such as a flame to a flow, an extended version of DMD (EDMD) has been suggested. Consider a set of fields $\{\phi_k\}_{k=1}^{m}$, $\phi_k \in \mathbb{R}^p$, sampled simultaneously with the set $\{u_k\}_{k=1}^{m}$. Put into matrix form $\Phi_1^{m-1} \equiv [\phi_1\, \phi_2\, \ldots\, \phi_{m-1}]$, mode i can be obtained from

$$\Phi_1^{m-1} x_i \tag{3.14}$$

where x_i is a result of the DMD analysis of $\{u_k\}_{k=1}^{m}$, see eq. (3.13). Note that the dimension of ϕ (p) does not need to be the same as the dimension of u (N). The method is analogous to Extended POD (EPOD) [38, 4]. In [4], the flow field inside a model engine cylinder was sampled during the intake stroke using PIV. The method was used to calculate flow modes in the entire sample region, based on a POD analysis in a subdomain. Using this approach, focus could be placed on the relatively weak events in the subdomain. A different application, a flame-flow coupling, considering simultaneously sampled PIV and OH-PLIF data, was carried out in [14]. An annular burner with an unsteady laminar flame was studied, both with and without acoustic excitation.

Chapter 4

Chaotic time series analysis

Dynamical systems, even low-dimensional ones, can give rise to very complicated phase space trajectories. For dissipative systems, these trajectories generally end up on subsets of the phase space, on so-called *attractors*. Attractors determine the typical behaviour of the systems, where simple attractors include stable (zero-dimensional) fixed points and (one-dimensional) limit cycles. In particular, seemingly high-dimensional fluid systems may turn out to result from low-dimensional attractors. A trajectory which starts within an attractors *basin of attraction* will inevitably tend towards the attractor. For a given system, there may be multiple attractors, and therefore multiple basins of attraction. Analysing these systems, particularly chaotic systems, can be difficult. The perceived complexity, in part, comes from tools originally built for linear systems. Notably, spectral analysis has a problem with separating (low-dimensional) dynamics from (high-dimensional) noise. The difficulty becomes even more palpable when the underlying dynamical system is unknown, and only a scalar time series is available, which is frequently the case for experimental data. A popular approach, for sample data $u(k) \in \mathbb{R}$, $k = 1, 2, ..., N$, is to consider a *time delay embedding.* This involves creating a d_E-dimensional space containing points $y \in \mathbb{R}^{d_E}$, built using time delays,

$$y(k) = [u(k)\ u(k+T)\ u(k+2T)\ ...\ u(k+(d_E-1)T)], \tag{4.1}$$

where T is the time delay (which in this context is an integer) and d_E is the embedding dimension. Thus, a trajectory in the embedding space is given by the evolution $y(k) \to y(k+1)$. The goal is to use the trajectory in the embedding space to capture the dynamics of the original multi-dimensional system. The formal requirements for this type of embedding are given by Takens' theorem [69]. After the attractor has been unfolded, in the d_E-dimensional embedding space, invariant properties may be evaluated, in particular the attractor dimension and the global Lyapunov spectrum. These invariants help characterize the system, and give useful information regarding the dynamics. While the attractor dimension says something about the amount of information needed to describe the system, the Lyapunov spectrum provides information about e.g.

predictability. It may be noted that when the attractor dimension is not an integer, which is generally the case for chaotic systems (using any reasonable definition of dimension), the attractor is called *strange*. A review of the analysis of chaotic time series is given by Abarbanel *et al.* [1].

In Section (4.1), a method to evaluate the appropriate time delay T is given, followed in Section (4.2) by a procedure used to calculate the smallest possible embedding dimension d_E. Different definitions of the attractor dimension are discussed in Section (4.3), while the global Lyapunov spectrum is considered in Section (4.4).

4.1 Time delay

Any time delay T, referring to eq. (4.1), should work if an infinite amount of infinitely precise data is available. However, in practice, some appropriate value needs to be chosen. The value should preferably be sufficiently large so that the new step is clearly separated from the previous step, and yet not so large that the correlation with the previous step has vanished. A possible choice in determining T is to use the first zero of the autocorrelation function $\langle u(k+T)u(k)\rangle_k$. However, a better nonlinear alternative is typically to use the *average mutual information*. The mutual information, considering two systems A and B, is

$$I_{AB}(a,b) = \log_2\left(\frac{P_{AB}(a,b)}{P_A(a)P_B(b)}\right),$$

where $a \in A$, $b \in B$, and P represents the corresponding probability distributions (single P_A, P_B, and joint P_{AB}). In particular, $P_{AB}(a,b) = P_A(a)P_B(b)$ gives $I_{AB}(a,b) = 0$, i.e. the events say nothing about one another. Taking the average of the mutual information gives

$$I_{AB} = \sum_{a,b} P_{AB}(a,b) I_{AB}(a,b).$$

In this case, considering the above time series, $u(k) \in A$ and $u(k+T) \in B$, leading to

$$I(T) = \sum_k P(u(k), u(k+T)) \log_2\left(\frac{P(u(k), u(k+T))}{P(u(k))P(u(k+T))}\right). \tag{4.2}$$

Practically, the first local minimum is used, $T = T_m$, $(dI/dT)(T_m) = 0$ (and a positive second derivative). However, when there is no such minimum, a value T where $I(T) \approx I(0)/5$ may be used instead [1].

4.2 Embedding dimension

There exists several methods attempting to calculate the minimum embedding dimension d_E, for example using singular value decomposition. If the attractor dimension d_A is known, which is generally not an integer, Takens' theorem says that $d_E > 2d_A$ is sufficient. However, this estimate is often too conservative, and smaller embedding dimensions may be possible to obtain. Note that when the embedding dimension is larger than necessary, not only do the computational requirements increase, but the additional dimensions are also filled with noise for contaminated signals. The most popular method to extract the embedding dimension appears to be the *false nearest neighbour* approach [31]. The steps proceed as follows:

1. Consider the points $y(k)$ (from eq. (4.1)) for $d_E = 1$, $y(k) = [u(k)]$, for all k.

2. Find the nearest neighbour to $y(k)$, $y^{NN}(k)$, considering the metric $R_d(k)$,

$$R_1^2(k) = (u(k) - u^{NN}(k))^2.$$

3. Add a new dimension so that $d_E = 2$, $y(k) = [u(k)\ u(k+T)]$.

4. Check if $y(k)$ and $y^{NN}(k)$ are still "neighbours". If the criterion

$$\frac{|u(k+T) - u^{NN}(k+T)|}{R_1(k)} > R_T$$

is true, for some threshold value R_T, the points $y(k)$ and $y^{NN}(k)$ are considered to be *false neighbours.* If the expression is not true, calculate

$$R_2^2(k) = R_1^2(k) + (u(k+T) - u^{NN}(k+T))^2$$

and check if

$$\frac{R_2(k)}{R_A} > 2 \tag{4.3}$$

where R_A is the "size" ("radius") of the attractor, often taken to be the standard deviation of the data ($std(u)$). If expression (4.3) is true, $y(k)$ and $y^{NN}(k)$ are false neighbours. This second criterion is especially important for noisy environments.

5. Find *new* nearest neighbours for $d_E = 2$, for all k, and evaluate how many of them are false by continuing the recipe given above.

Continue adding dimensions ($d_E = 3, 4, ...$) until there are no false neighbours left, or a negligable amount. The general criteria look like

$$\frac{|u(k+dT) - u^{NN}(k+dT)|}{R_d(k)} > R_T$$

and

$$\frac{R_{d+1}(k)}{R_A} > 2.$$

A value for the threshold R_T needs to be chosen, where $R_T = 10 - 20$ appears to be in use. The above algorithm not only gives a value of the minimum embedding dimension, but it also provides an estimate of the error one makes in using a dimension that is too small, since the number of false neighbours is checked for each dimension.

4.3 Attractor dimension

Inside an embedding space, where the attractor has been completely unfolded, the attractor dimension d_A may be evaluated. There exists many different definitions of the attractor dimension, several of which should give very similar values, at least for simple fractals. With the embedding space partitioned into elements, a common feature in evaluating a dimension is to analyse how a bulk property of the elements change with the element size (or "radius"). Consider an attractor covered by "boxes" with side length r. The number of boxes N needed to cover the attractor, in the limit $r \to 0$, leads to the *box-counting dimension* D_0, $D_0 = \lim_{r\to 0} \log N/ \log r^{-1}$. Further generalization gives the *information dimension* D_1 and the *correlation dimension* D_2. The information dimension is defined as

$$D_1 = \lim_{r\to 0} \frac{-\sum_i p_i \log p_i}{\log r^{-1}},$$

where the probability $p_i = n_i / \sum_k n_k$ for the number of points n_i inside element i of the embedding space. r is again the size of an element. Note that while the box-counting dimension only checks if the elements (boxes) are nonempty, p_i for the information dimension is proportional to the number of points inside the element. The correlation dimension is defined as

$$D_2 = \lim_{r\to 0} \frac{\log \sum_i p_i^2}{\log r^{-1}},$$

involving the probability of finding pairs of points inside the elements. The correlation dimension is typically estimated using the Grassberger-Procaccia correlation function $C_2(r)$,

$$C_2(r) = \frac{2}{N(N-1)} \sum_{i\neq j}^{N} H(r - ||y(j) - y(i)||), \tag{4.4}$$

where H is a step function ($H(x) = 1$ for $x > 0$, $H(x) = 0$ for $x < 0$). The correlation dimension is then estimated by plotting $\log C_2(r)$ against $\log r$, for small r, where the dimension is given by the slope.

A different way of extracting a useful quantity is based on the Lyapunov exponents $\{\lambda_i\}$, introduced in the next section, ordered such that $\lambda_i \geq \lambda_j$ if $i < j$. The *Kaplan-Yorke dimension* D_{KY} is defined as

$$D_{KY} = m + \frac{\sum_{i=1}^{m} \lambda_i}{|\lambda_{m+1}|},$$

where m is the maximum value under the condition that $\lambda_1 + \lambda_2 + ... + \lambda_m > 0$. As was strongly suggested in [5], this implies that the first $m + 1$ exponents are in some sense of fundamental importance to the character of the attractor. Note that when the sum of *all* exponents is negative, the system is dissipative. While the first m directions have a space-filling character, with its positive sum of exponents, the addition of the $(m + 1)$st direction gives a negative sum and a collapse onto a fractal. Displacements in the additional directions, with more negative exponents, decay rapidly onto the attractor and are of less interest. The Kaplan-Yorke conjecture states that $D_{KY} = D_1$ for "typical" systems.

4.4 Global Lyapunov spectrum

Lyapunov exponents provide information about the evolution of nearby trajectories, where a positive exponent implies exponential divergence in its corresponding direction. The Lyapunov spectrum is the set of all (important) Lyapunov exponents. While evaluating the eigenvalues of the linearized dynamics locally leads to the local Lyapunov spectrum, taking into account the entire attractor gives the global Lyapunov spectrum. To calculate the global Lyapunov spectrum, which is an invariant characterizing and classifying the attractor, information is needed about how neighbouring points evolve along the attractor. The evolution of small disturbances can be obtained from

small disturbance at step k+1 =
*Jacobian(k)*Jacobian(k-1)...Jacobian(1)*small disturbance at step 1*

if the Jacobian matrices at the different steps are known ("*" is matrix multiplication). Note that the disturbances need to stay small for the linearized dynamics to be valid. The goal is to extract the full set of exponents, or at least those which are "strongly involved" in the dynamics of the attractor, and not just the largest exponent. This section is based on the work in [5, 7].

Consider the small displacement vector $z^r(k;0) \equiv y^r(k;0) - y(k)$ around $y(k)$, for the rth nearest neighbour, after time T_2, $z^r(k;T_2)$. The components are

$$z^r_\alpha(k;0) = u(k_r + (\alpha - 1)T) - u(k + (\alpha - 1)T)$$

and

$$z^r_\alpha(n;T_2) = u(k_r + T_2 + (\alpha - 1)T) - u(k + T_2 + (\alpha - 1)T)$$

for $\alpha = 1, 2, ..., d$ and $r = 1, 2, ..., N_b$. k_r is the index for the rth nearest neighbour. If the dynamics is written as

$$y(k + T_2) = F(y(k)),$$

the displacements evolve according to

$$z^r(k;T_2) = y^r(k;T_2) - y(k + T_2) = F\left(y(k) + z^r(k;0)\right) - F(y(k)).$$

A Taylor expansion leads to

$$z_\alpha^r(k;T_2) = \frac{\partial F_\alpha}{\partial y_\beta} z_\beta^r(k;0) + \frac{1}{2!}\frac{\partial^2 F_\alpha}{\partial y_\beta y_\gamma} z_\beta^r(k;0) z_\gamma^r(k;0)$$

$$+\frac{1}{3!}\frac{\partial^3 F_\alpha}{\partial y_\beta \partial y_\gamma \partial y_\delta} z_\beta^r(k;0) z_\gamma^r(k;0) z_\delta^r(k;0) + H.O.T.$$

where the derivatives are evaluated at $y(k)$. Neglecting the third and higher order terms for a moment, the problem takes the form $V^\alpha = XB^\alpha$, where

$$V^\alpha = \begin{pmatrix} z_\alpha^1(k;T_2) \\ z_\alpha^2(k;T_2) \\ \vdots \\ z_\alpha^{N_b}(k;T_2) \end{pmatrix},$$

$$B^\alpha = \begin{pmatrix} D_1 F_\alpha(k) \\ \vdots \\ D_d F_\alpha(k) \\ D_{11}^2 F_\alpha(k) \\ D_{12}^2 F_\alpha(k) \\ \vdots \\ D_{dd}^2 F_\alpha(k) \end{pmatrix},$$

and

$$X =$$

$$\begin{pmatrix} z_1^1(k;0) & \cdots & z_d^1(k;0) & z_1^1(k;0)z_1^1(k;0) & z_1^1(k;0)z_2^1(k;0) & \cdots & z_d^1(k;0)z_d^1(k;0) \\ z_1^2(k;0) & \cdots & z_d^2(k;0) & z_1^2(k;0)z_1^2(k;0) & z_1^2(k;0)z_2^2(k;0) & \cdots & z_d^2(k;0)z_d^2(k;0) \\ & \vdots & & & & \vdots & \\ z_1^{N_b}(k;0) & \cdots & z_d^{N_b}(k;0) & z_1^{N_b}(k;0)z_1^{N_b}(k;0) & z_1^{N_b}(k;0)z_2^{N_b}(k;0) & \cdots & z_d^{N_b}(k;0)z_d^{N_b}(k;0) \end{pmatrix}.$$

The notation $D_\beta F_\alpha = \partial F_\alpha / \partial y_\beta$ and $D_{\beta\gamma}^2 F_\alpha = \frac{1}{2!}\partial^2 F_\alpha / \partial y_\beta y_\gamma$ has been used. The interest lies in extracting the Jacobian DF, which may be obtained by (pseudo) inverting the matrix X. Adding the cubic term implies the addition of terms $z_\beta^r(k;0)z_\gamma^r(k;0)z_\delta^r(k;0)$ to X. The total number of neighbours to follow (in order to avoid an underdetermined system), N_b, needs to be at least N_P,

$$N_P = \left(\prod_{n=1}^{N_\tau} \frac{d+n}{n}\right) - 1,$$

where N_τ is the order of the expansion, which, including the cubic term, is $N_\tau = 3$. It is recommended that $N_b \geq 2N_P$, and in this thesis $N_b = 2N_P$.

Multiplying these Jacobians is not a stable procedure. Therefore, at every step k, a QR decomposition is made

$$DF(y(k))Q(k-1) = Q(k)R(k),$$

where $Q(0) = I$ (the identity matrix), implying that

$$DF(y(k))DF(y(k-1))...DF(y(1)) = Q(k)\prod_{n=1}^{k} R(n).$$

The Lyapunov exponents λ_m are calculated from (the real part of)

$$T_2\lambda_m = \lim_{K\to\infty} \frac{1}{K}\sum_{k=1}^{K} \ln(R_{mm}(k)),$$

where T_2 in this case is the actual time (not the dimensionless integer).

It is not obvious what d value should be used in the above equations. The notion of a *global* dimension d_G and a *local* dimension d_L may be introduced, where the global dimension is simply the embedding dimension, $d_G = d_E$. If DF is a $d_E \times d_E$ matrix, and d_E is larger than the "true/natural" dimension of the system, it will contain spurious Lyapunov exponents. As stated by Brown et al. [5], *"Under one approach the evolution vectors y(n) are of dimension* $d = d_L < d_G$*. The reconstruction is thus not globally diffeomorphic to the attractor that represents the true dynamics. However, we believe that the y's do capture the true local dynamics of the attractor."* Using a value of d_L as low as possible is probably beneficial for all (true) Lyapunov exponents in a noisy environment. For the local dimension, use

$$d_A \leq d_L < d_A + 1,$$

where the rest of the $(d_G - d_L)$ Lyapunov exponents should be of less interest for understanding the attractor. Thus, while d_G is used to calculate the N_b nearest neighbours, d_L is used for the rest of the procedures (in particular, z^r becomes a d_L-dimensional vector).

The global Lyapunov spectrum carries a lot of information about the dynamics on the attractor. In particular, the existence of at least one positive exponent is the hallmark of a chaotic system. The inverse of the maximum Lyapunov exponent furthermore reflects the time scale on which the system becomes unpredictable.

Chapter 5

Computational models

The governing equations for fluid flow have already been specified in Section (2.1). In order to solve these equations, with given initial and/or boundary conditions, all the active flow scales need to be accounted for. While this may not be a problem for laminar flows or flows at moderate Reynolds numbers, for high Reynolds numbers it becomes a huge problem. Following the discussion in Section (2.3), eq. (2.18) would imply a cell/node number (in a spatial discretization) scaling with

$$\left(\frac{l_0}{l_\eta}\right)^3 \sim Re_{l_0}^{9/4},$$

and a total scaling (including time integration) with $Re_{l_0}^3$. Resolving every (flow) scale in a computational realization is called a *direct numerical simulation* (DNS). For most engineering applications this is not feasible with todays computers, and reasonable approximations need to be made.

One approach is to solve for an averaged velocity field $\langle u_i \rangle$, where the large variations (derivatives) have been filtered out, implying that the resolution can be significantly reduced. The time/ensamble averaged (assuming an ergodic system) equations (2.9) and (2.10), for a statistically stationary flow, are called the *Reynolds averaged Navier-Stokes* (RANS) equations. The ensamble averaged equations, keeping the temporal derivatives, are called the *unsteady*-RANS (URANS), or perhaps the *transient*-RANS (TRANS), equations.

A proposal put forward by Kolmogorov, as already discussed in Section (2.3), is that the smaller spatial scales (away from any solid boundary) are independent of the geometry, a universality that could be exploited for modelling. Resolving only the larger spatial scales, while modelling the effect that the smaller scales would have had on the resolved scales, is called *large eddy simulation* (LES). Using LES, beyond the conjectured improvement in modelling prospects, one is able to capture structures that are not necessarily present on average, or that at least would become heavily smeared. However, computational requirements can increase substantially for ("good") LES compared to RANS/URANS. For ideal turbulent flow the resolution is often well within the inertial subrange, which in 3-D implies a spatial resolution of the order of O($Re^{1.5}$), and with adequate time resolution the total amount of computational work would be of the order O(Re^2). Some fundamental questions concerning LES are raised in Pope [51].

5.1 Reynolds averaged Navier-Stokes equations

Averaging eqs. (2.9) and (2.10), and introducing the separation $u_i = \langle u_i \rangle + u_i'$, gives

$$\frac{\partial \langle u_i \rangle}{\partial t} + \frac{\partial \langle u_i \rangle \langle u_j \rangle}{\partial x_j} = -\frac{1}{\rho}\frac{\partial \langle p \rangle}{\partial x_i} + \frac{\partial}{\partial x_j}\left(\nu \frac{\partial \langle u_i \rangle}{\partial x_j} - \langle u_i' u_j' \rangle\right).$$

and

$$\frac{\partial \langle u_j \rangle}{\partial x_j} = 0.$$

The extra term $-\langle u_i' u_j' \rangle$ has been moved to the right hand side, and is interpreted as a stress term, the so-called *Reynolds stress*. Note that the density, since it is just a constant value, will not be of concern (it may be put in at any time to get the correct dimensions).

The term $\langle u_i' u_j' \rangle$ is not available, and in trying to solve for this term, terms of the form $\langle u_i' u_j' u_k' \rangle$ are needed, and so on. This is called the *closure problem*, and it necessitates the introduction of models. The modelling is thus intended to incorporate how the fluctuations would affect the average flow $\langle u \rangle$, which is not an easy thing to do.

5.1.1 $k - \epsilon$ model

The most common closure model is the $k - \epsilon$ model. This is a two-equation model based on the eddy viscosity approach,

$$-\langle u_i' u_j' \rangle + \frac{2}{3} k \delta_{ij} = 2\nu_T \langle s_{ij} \rangle,$$

where $\nu_T = \nu_T(x, t)$ is the eddy viscosity field. The k-term on the left is added since the right hand side is traceless. The modelled Reynolds stresses are seen to respond immediately to changes in the mean field. The two equations are aimed at capturing the turbulence kinetic energy $k = \frac{1}{2} Tr(\langle u_i' u_j' \rangle)$, and the dissipation rate ϵ, which are then used to calculate ν_T,

$$\nu_T = C_\mu \frac{k^2}{\epsilon}.$$

The model equations are

$$\frac{\partial k}{\partial t} + \langle u_j \rangle \frac{\partial k}{\partial x_j} = \frac{\partial}{\partial x_j}\left(\frac{\nu_T}{\sigma_k}\frac{\partial k}{\partial x_j}\right) + P - \epsilon$$

and

$$\frac{\partial \epsilon}{\partial t} + \langle u_j \rangle \frac{\partial \epsilon}{\partial x_j} = \frac{\partial}{\partial x_j}\left(\frac{\nu_T}{\sigma_\epsilon}\frac{\partial \epsilon}{\partial x_j}\right) + C_{\epsilon 1}\frac{P\epsilon}{k} - C_{\epsilon 2}\frac{\epsilon^2}{k}$$

where $P = -\langle u_i' u_j' \rangle \langle s_{ij} \rangle = 2\nu_T \langle s_{ij} \rangle \langle s_{ij} \rangle$ is the production term, σ_k and σ_ϵ are the 'turbulent Prandtl numbers', usually $\sigma_k = 1.0$ and $\sigma_\epsilon = 1.3$, and the standard C-coefficients, taken from [52], are

$$C_\mu = 0.09, \quad C_{\epsilon 1} = 1.44, \quad C_{\epsilon 2} = 1.92.$$

In particular, due to the resulting production term P, there is likely to be a large overproduction of turbulence kinetic energy in regions where the streamlines are strongly curved.

5.2 Large eddy simulation

The object under consideration for LES is the spatially filtered field $\overline{\phi}$,

$$\overline{\phi}(x,t) = (G * \phi)(x,t) = \int G(x - x')\phi(x',t)dx',$$

for the filter kernel $G(x - x')$. Common filters, using filter width Δ, is the box filter

$$G(x) = \frac{1}{\Delta^3} H\left(\frac{1}{2}\Delta - |x_i|\right),$$

where H is the Heaviside function, and the Gaussian filter

$$G(x) = \frac{1}{\sqrt{2\pi\sigma^2}} \exp\left(-\frac{1}{2}\left(\frac{x}{\sigma}\right)^2\right),$$

where $\sigma \sim \Delta$. Most codes use implicit filtering, meaning that the discretization of the governing equations on the given grid provides the filtering operation. The filter width then essentially becomes the grid spacing h, $\Delta = h$. The alternative would be to explicitly filter the field at every grid point. The gain would be to suppress numerical errors introduced at the smallest scales (by averaging them out), at the expense of a reduced resolution ($\Delta > h$) and an increased overhead. Whether explicit filtering should be preferred, or if the additional computational resources instead should be put towards an increased resolution may be problem dependent. In general, explicit filtering needs somewhat less fine spatial resolution as compared with the implicit one. In general 3-D cases the gain in resolution is less as compared to the additional computational work. Thus, it is rather common using the implicit LES, provided that the resolution is fine enough to resolve at least some of the inertial subrange.

Filtering eqs. (2.9) and (2.10), assuming that the filtering operation and the spatial derivatives commute, gives

$$\frac{\partial \overline{u}_i}{\partial t} + \frac{\partial \overline{u}_i \overline{u}_j}{\partial x_j} = -\frac{1}{\rho}\frac{\partial \overline{p}}{\partial x_i} + \frac{\partial}{\partial x_j}\left(\nu \frac{\partial \overline{u}_i}{\partial x_j} + \tau_{ij}^{sgs}\right)$$

where

$$\tau_{ij}^{sgs} \equiv -(\overline{u_i u_j} - \overline{u}_i \overline{u}_j)$$

and

$$\frac{\partial \overline{u}_j}{\partial x_j} = 0.$$

The difference compared to the original problem, eqs. (2.9) and (2.10), is the additional term τ_{ij}^{sgs}, called the *subgrid scale* (SGS) stress tensor. Similar to RANS/URANS, LES also suffers from a closure problem. Thus, some assumptions/approximations are needed to solve for the filtered fields.

5.2.1 Smagorinsky model

The Smagorinsky model is analougus to the eddy viscosity concept,

$$\tau_{ij}^{sgs} - \frac{1}{3}\tau_{kk}^{sgs}\delta_{ij} = \nu_{sgs}\left(\frac{\partial \overline{u}_i}{\partial x_j} + \frac{\partial \overline{u}_j}{\partial x_i}\right) = 2\nu_{sgs}\overline{S}_{ij},$$

where the small scale turbulence is assumed to have a similar effect on the resolved scales as molecular viscosity. For the Smagorinsky model, the eddy viscosity is usually written as

$$\nu_{sgs} = (C_S\Delta)^2|\overline{S}|,$$

where $|\overline{S}| = (\overline{S}_{ij}\overline{S}_{ij})^{1/2}$ and the parameter C_S should be tuned for the particular case consided. Typically $C_S \sim 0.05 - 0.2$, with isotropic turbulence towards the higher end and shear flows towards the lower end, with even further decreasing values when approaching solid walls.

5.2.2 Germano procedure

For the Smagorinsky model, Section (5.2.1), the parameter C_S cannot be a constant and it should be considered as flow dependent. The Germano procedure provides a way to estimate this parameter, although the process is more general than that. The underlying assumption is that there is a certain similar (asymptotic) behaviour of the filtered variables when different filters are applied. Following the notation in [39],

$$\overline{\Phi}(q) = \Phi(\overline{q}) + \Phi_{mod}(\overline{q}, \Delta, C_1, C_2, ...), \tag{5.1}$$

where Φ_{mod} represents the model, with a set of parameters C_i. Especially, $\Phi(q = u) = u_i u_j$ should be considered. Introducing an additional filter of width $\alpha\Delta$, $\alpha > 1$, and *assuming that the same model, using the same parameter values, is valid on the coarser scale*,

$$\widetilde{\overline{\Phi}}(q) = \Phi(\widetilde{\overline{q}}) + \Phi_{mod}(\widetilde{\overline{q}}, \alpha\Delta, C_1, C_2, ...). \tag{5.2}$$

Applying the second filter on eq. (5.1), and equating it with the right hand side of eq. (5.2), leads to

$$\widetilde{\Phi}(\overline{q}) + \widetilde{\Phi}_{mod}(\overline{q}, \Delta, C_1, C_2, ...) = \Phi(\widetilde{\overline{q}}) + \Phi_{mod}(\widetilde{\overline{q}}, \alpha\Delta, C_1, C_2, ...), \tag{5.3}$$

called the (generalized) *Germano identity*. Since both $\overline{q}$ and $\widetilde{\overline{q}}$ should be available (without much effort), eq. (5.3) can be considered a restriction on the parameters C_i. One should note that the computed parameter may have both positive and negative sign and it may vary from one point to another. When one uses as a model a Smagorinsky like expression, a positive parameter value implies dissipation of kinetic energy into heat, whereas negative values mean generation of energy (and indirectly so-called backscatter). However, large negative values imply also that high frequency fluctuation are amplified which may lead to numerical instability. Therefore, it is common to put restrictions on the size of the negative value of the parameter. Olsson & Fuchs [48] for example proposed that the numerical and the dynamic model together should be dissipative.

5.2.3 Scale-similarity model

In this model it is assumed that the primary interactions take place between scales that are a little larger and a little smaller than the filter width Δ, along with the assumption of *self-similarity*, i.e., the idea that interactions at different scales show similar characteristics. This line of reasoning leads to

$$\tau_{ij}^{sgs} = -(\widetilde{\overline{u}_i\overline{u}_j} - \widetilde{\overline{u}}_i\widetilde{\overline{u}}_j),$$

using a second filter of width $\alpha\Delta$, $\alpha > 1$. Since this model has been seen to dissipate very little energy, it is often used in conjunction with another model. It allows for energy transfer from the smallest resolved scales to the larger scales (backscatter), which can be useful.

5.2.4 Implicit LES (ILES)

Using this approach the numerics itself should handle the turbulence modelling. Arguably the most important function for a subgrid scale model is to dissipate energy (mainly at the small scales), and a way to accomplish this can be through the addition of numerical diffusion. For a second order code, this may be done by including a (first order) upwind (UW) scheme. The principle can be illustrated by considering a positive convective flow, $u_i \equiv u(x_i) > 0$, which, assuming a constant mesh spacing, $\Delta x = x_i - x_{i-1}$, gives the upwind scheme

$$\begin{aligned} \left(\frac{du}{dx}\right)_i &\approx \left(\frac{du}{dx}\right)_{i,UW} = \frac{u_i - u_{i-1}}{\Delta x} = \frac{u_{i+1} - u_{i-1}}{2\Delta x} - \frac{\Delta x}{2}\frac{u_{i+1} - 2u_i + u_{i-1}}{\Delta x^2} \\ &\approx \left(\frac{du}{dx}\right)_{i,CD} - \frac{\Delta x}{2}\left(\frac{d^2u}{dx^2}\right)_i \end{aligned}$$

introducing the second order central difference (CD) scheme. The one-dimensional convective term may now be written as

$$u_i \left(\frac{du}{dx}\right)_i \approx u_i \left(\frac{du}{dx}\right)_{i,CD} - \nu_i \left(\frac{d^2u}{dx^2}\right)_i \tag{5.4}$$

where $\nu_i = u_i \Delta x/2 > 0$ can be considered to be a numerical viscosity. Eq. (5.4) becomes valid also for $u_i < 0$ given that $\nu_i = |u_i| \Delta x/2$. If the grid is fine enough to resolve scales far into the inertial subrange (see Fig. (2.11)), this approach should be sufficient. This follows since the other terms in the momentum equation should be much larger than the SGS term.

Chapter 6

Reacting flows

In the chapters above we have been considering the flow of an incompressible fluid (i.e. with constant density). Such flows are also characterized by the fact the information propagates at infinite speed (that is why the equation for the pressure is the Poisson equation) and the flow is isothermal (i.e. satisfying the energy equation identically with a given constant temperature). Chemical reactions with heat-release change the simplified picture of incompressible flows in several ways. The density and temperature vary in space and time. Equally, the turbulence of the flow affect the local concentration of the fuel and oxidizer, whereby the heat-release becomes non-uniform or constant. Therefore, one has to extend the system of equations to include not only the energy equation (and the equation of state relating the density, temperature and pressure to each other), but also the transport and consumption of the different species that are involved in the chemical process. In the following we give only the highlights and most relevant items of combustion modelling as this is not the main topic of the thesis.

Considering the simplest possible chemistry, the combustion of hydrocarbons may be highlighted, exemplified by the complete oxidation of methane,

$$\mathrm{CH_4} + 2\mathrm{O_2} \rightarrow \mathrm{CO_2} + 2\mathrm{H_2O}$$

releasing about 0.8MJ heat per mole of methane. The reaction given above is global, and does not happen in a single step. Instead, many intermediate species and interactions take place, and for an exact calculation typically a very large number of elementary reaction, with widely different time-scales, has to be accounted for. However, as a major simplification one may reduce the stiff system of chemical reaction to a single or few major chemical reactions. Each of the species involved has to be followed (by satisfying the convection by the fluid, diffusion and production/destruction through chemical reactions). One may distinguish between different combustion types and regimes. A common classification is to diffusion (non-premixed) flames, premixed flames, and more recently the partially premixed flame became popular. In this thesis we have been considering only the latter types of flames.

Since diffusion flames may be less efficient and burn at nearly stochiometric conditions, where the energy released per mole of fuel may lead to high temperatures and therefore a higher NO_x production, premixed flames are preferred in modern gas turbine and internal combustion engine applications. However, not only are there general safety concerns associated with a fuel and oxidizer mixed in advance, but there are also additional difficulties regarding flame stabilization.

Note that for premixed flames, the laminar flame speed of a typical hydrocarbon/air mixture is usually low. Thus, in order to enhance mixing and combustion one can utilize turbulence. Hence, turbulent mixing is required to increase the burning rate and the heat release rate.

6.1 Turbulent premixed combustion

A premixed flame, going normal to the flame front, can be divided into three regions. These are termed as the preheat zone, the inner layer or reaction zone, and the oxidation zone. In the preheat zone few reactions take place, and the increased temperature is primarily due to thermal diffusion from the reaction zone. The reaction zone is a thin layer where most of the reactions take place, and the only region where some short lived radicals will be found. Lastly, the oxidation zone is where the more long lived radicals oxidize (such as OH and CO), increasing further the temperature.

Consider a chemical time scale τ_c, estimated by $\tau_c \sim \delta_L^2/\alpha$ where δ_L is the laminar flame thickness and α is the thermal diffusion coefficient. The nondimensional Karlovitz number is introduced

$$Ka \equiv \frac{\tau_c}{\tau_\eta} \sim \left(\frac{\delta_L}{l_\eta}\right)^2,$$

where $\tau_\eta \sim l_\eta^2/\nu$ is the Kolmogorov time scale and a unity Prandtl number $Pr \equiv \nu/\alpha \sim 1$ has been assumed. For $Ka \ll 1$, the flame burns in the *flamelet* regime, where the effect of turbulence on the flame is only to wrinkle it. For values $Ka \sim 1 - 100$, the flame burns in the *thin reaction zone* regime, where the smallest turbulence scales can start to disturb and broaden the preheat zone. When the Karlovitz number goes above $Ka \sim 100$, the flame goes into the *distributed reaction zone* regime, where eddies at the Kolmogorov scale start to penetrate into the reaction zone, since this layer is typically about an order of magnitude thinner than the flame thickness, and flame quenching can become a problem. Further, comparing the large scale turbulence with the flame properties, one may consider the Reynolds number

$$Re = \frac{u_0' l_0}{S_L \delta_L},$$

using the laminar flame speed S_L, where $Re < 1$ is taken to be a laminar flame regime. The flame-flow regions specified above are summarized in Fig. (6.1), the

Peters-Borghi diagram. In practical applications, the flame in the combustion chamber is unsteady and it may exhibit different character in space in time (i.e. be located in different parts of the diagram).

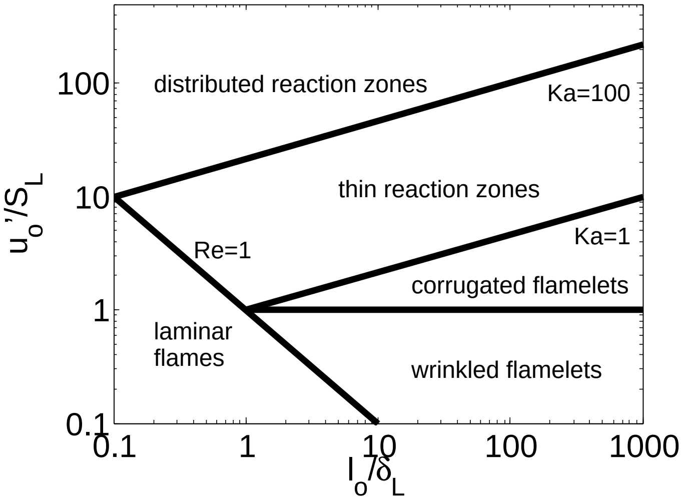

Figure 6.1: Peters-Borghi diagram for turbulent premixed combustion.

The flame thickness of non-wrinkled and wrinkled flames is often small for most hydrocarbons. With turbulent wrinkling the thickness of the flame may vary and it may become thicker of the order of the small Kolmogorov scales or even larger. In these cases the interaction between turbulence and the chemistry is strong and requires a Direct Numerical Simulations (DNS) resolution in space. Additionally, for consistency it would need also a complete temporal resolution for the different chemical reactions. Such computations are not practical even for simple cases. Most current simulation (often termed as DNS) use the required spatial resolution together with simple reduced chemistry with time-scales that are resolved. Faster reactions are handled by assuming steady-state or equilibrium. When the flame is thin one may use simplifications also to the chemistry by introducing the flamelet concept. This concept leads to 1-D handling of the chemistry and allows the handling of the flame motion through a flame tracking. In the combustion case considered in this thesis, the *G*-equation is used for tracking the flame.

6.1.1 Flame tracking: G-equation

Assume that the flame can be considered as a thin interface separating the unburnt and burned regions. We define a scalar valued *G*-field such that it attains the value one in the burned and minus one in the unburnt region with the value of zero at the flame front itself. With an appropriate scaling one may make the scalar to represent the distance from the flame front. Thereby, one may use a 1-D model describing the reaction in the flame as one crosses the from the unburnt to the burnt zone. Consider next a signed function, such that the isosurface

$$G(x,t) = 0$$

marking the flame front. The governing equation for the motion of the interface takes the form

$$\frac{\partial G}{\partial t} + u_j \frac{\partial G}{\partial x_j} = S_L |\nabla G|, \tag{6.1}$$

where u_j is the convective flow field that convects the front. The velocity S_L is the speed of the front relative to itself in the normal direction. This front velocity has to be provided in form of a model. The same applies also for turbulent flames where the flame front varies in space and time. Typically, one may assume that the flame speed is proportional to the velocity fluctuations when the laminar flame speed it small.

Typically, for LES $u_j \to \overline{u}_j$, $G \to \overline{G}$ might be considered, and then taking the flame speed to be related to the subgrid scale fluctuations.

$$S_L \to S_{LES} = S_L \cdot H \cdot \left(1 + C \frac{u'_{sgs}}{S_L + \beta}\right), \tag{6.2}$$

where usually $C \approx 1$, β takes some small value, and H is a Heaviside step function accounting for the lean flammability limit [43]. The model in equation (6.2) is supposed to account for the enhanced mixing and combustion by the subgrid scale turbulence. The subgrid scale fluctuations of the velocity field are handled through the Smagorinsky model.

Chapter 7

Numerical methods

The work presented in this thesis is very collaborative, and several different codes have been used. Focus is placed on the open source library *OpenFOAM* [81, 29], which is used in many of the cases, including the main study regarding bent pipe flow. OpenFOAM is a finite volume based code, where the computational domain is separated into an arbitrary number of non-overlapping polyhedral control volumes, or cells, allowing for complex geometries. Because of this large freedom in the structure of the cells, together with concerns regarding computational requirements, the method is limited to at most second order accuracy. As will be discussed, even this second order accuracy typically has to be relaxed in certain parts of the flow. An attractive feature of the finite volume approach is that conservation of momentum, mass, energy, and passive scalars, is upheld at the discrete level. Some of the numerical procedures implemented in OpenFOAM are covered in [29], on which much of this chapter is based, using similar notation. In particular, boundary conditions will not be treated below and may be found in [29].

In Section (7.1) the tools used for grid generation are introduced, followed by a general description of the second-order finite volume method in Section (7.2). A few of the temporal discretization schemes and spatial interpolation schemes available in OpenFOAM are then given in Section (7.3) and (7.4), respectively. Finally, in Section (7.5), the pressure-velocity coupling is addressed.

7.1 Grid generation

Grids were generated using the OpenFOAM tools *blockMesh* and *snappyHexMesh*. By combining these tools, rectangular cuboids can be obtained in the bulk of the domain also for complex geometries. For complex geometries, surface files of *stereolithographic* (STL) format were created using the open source software *Art of Illusion* [23].

7.2 Second-order finite volume method

The standard transport equation (for mass, momentum and energy), allowing for diffusive transport, for the quantity per unit mass ϕ can be considered to be

$$\frac{\partial \rho\phi}{\partial t} + \nabla \cdot (\rho u \phi) + \nabla \cdot (-\rho \Gamma_\phi \nabla \phi) = S_\phi(\phi)$$

where $\rho u \phi$ is the convective flux, $-\rho\Gamma_\phi \nabla\phi$ is the modelled diffusion flux, and S_ϕ is a source term. Integrating over a control volume V_P, containing the point x_P, and a time interval t to $t + \Delta t$, gives

$$\int_t^{t+\Delta t} \left[\frac{\partial}{\partial t} \int_{V_P} \rho\phi \, dV + \int_{V_P} \nabla \cdot (\rho u \phi) \, dV + \int_{V_P} \nabla \cdot (-\rho\Gamma_\phi \nabla\phi) \, dV \right] dt \\ = \int_t^{t+\Delta t} \left[\int_{V_P} S_\phi(\phi) dV \right] dt. \quad (7.1)$$

It will be assumed, or approximated, that only *linear* variations of the various fields inside the volume V_P take place,

$$\psi(x) = \psi_P + (x - x_P) \cdot (\nabla\psi)_P,$$

giving the volume integration

$$\int_{V_P} \psi \, dV = \psi_P V_P + \left[\int_{V_P} (x - x_P) \, dV \right] \cdot (\nabla\psi)_P.$$

At this stage, the point x_P may be defined to be the point inside the cell where $\int_{V_P} (x - x_P) \, dV = 0$. The spatial integration of the first term on the LHS of eq. (7.1) can then, given the above approximation, be written as

$$\int_{V_P} \rho\phi \, dV = (\rho\phi)_P V_P.$$

In the context of the finite volume approach, the (generalized) Gauss theorem is the major player, with

$$\int_V \nabla \cdot \psi \, dV = \int_{\partial V} dS \cdot \psi, \quad (7.2)$$

and

$$\int_V \nabla \psi \, dV = \int_{\partial V} dS \, \psi, \quad (7.3)$$

where ∂V denotes the boundary of the volume V. It should be noted that eq. (7.3) holds for both scalar and vector valued ψ. Again, assuming only a linear variation of the fields over every flat face f,

$$\psi(x) = \psi_f + (x - x_f) \cdot (\nabla\psi)_f,$$

gives

$$\int_f dS \cdot \psi = S_f \cdot \psi_f + \left[\int_f dS(x - x_f) \right] : (\nabla\psi)_f,$$

after which the point x_f on the face can be defined as the place where $\int_f dS(x - x_f) = 0$. The vector S_f has a magnitude equal to the surface area, and is considered to be pointing in the normal direction outwards from the cell. Each face is shared with only one neighbouring cell. For the spatial integration of the convective term in eq. (7.1) one may write

$$\int_{V_P} \nabla \cdot (\rho u\phi)\, dV = \int_{\partial V_P} dS \cdot (\rho u\phi) = \sum_f \left(\int_f dS \cdot (\rho u\phi) \right) = \sum_f S_f \cdot (\rho u\phi)_f.$$

For a colocated arrangement $\rho u\phi$ needs to be interpolated onto the faces f. The term is approximated by making the split $(\rho u\phi)_f = (\rho u)_f \phi_f$, and the mass flow rate through the face is introduced as $F_f \equiv S_f \cdot (\rho u)_f$. For the diffusion term in eq. (7.1) the spatial integration similarly becomes

$$\begin{aligned} \int_{V_P} \nabla \cdot (-\rho\Gamma_\phi \nabla\phi) &= \int_{\partial V_P} dS \cdot (-\rho\Gamma_\phi \nabla\phi) = \sum_f \left(\int_f dS \cdot (-\rho\Gamma_\phi \nabla\phi) \right) \\ &= \sum_f S_f \cdot (-\rho\Gamma_\phi \nabla\phi)_f, \end{aligned}$$

which requires the gradient of ϕ on the face f. Also here a split $(\rho\Gamma_\phi \nabla\phi)_f = (\rho\Gamma_\phi)_f (\nabla\phi)_f$ is considered. The term on the RHS in eq. (7.1), the source term, needs to be linearized if a linear solver is to be used,

$$S_\phi(\phi) = Su + Sp\,\phi,$$

and the spatial integration becomes

$$\int_{V_P} S_\phi(\phi) dV = SuV_P + SpV_P\phi_P.$$

Considering the special case of the incompressible Navier-Stokes equations, eq. (2.9), $\phi = u$ and $S_u = -\nabla p$, using eq. (7.3),

$$\begin{aligned} \int_t^{t+\Delta t} \left[\frac{\partial}{\partial t} u_P V_P + \sum_f F_f u_f - \nu \sum_f S_f \cdot (\nabla u)_f \right] dt \\ = \int_t^{t+\Delta t} \left[-\frac{1}{\rho} \sum_f p_f S_f \right] dt, \end{aligned} \tag{7.4}$$

where instead the *volume* flow rate $F_f = S_f \cdot u_f$ is considered. For the mass conservation, eq. (2.10),

$$0 = \int_{V_P} \nabla \cdot u dV = \int_{\partial V_P} dS \cdot u = \sum_f \left(\int_f dS \cdot u \right) = \sum_f S_f \cdot u_f = \sum_f F_f. \tag{7.5}$$

For eqs. (7.4) and (7.5), besides a way to handle the time integration, ways of handling the face interpolations for the different terms are needed. Below, a few different approaches are presented for handling the time integration, Section (7.3), and the spatial interpolation, Section (7.4).

7.3 Temporal discretization schemes

In this section the time integration in eq. (7.4) is addressed. Special treatment may be given to the non-orthogonal part of $(\nabla u)_f$.
Let

$$\psi^n \equiv \psi(t+\Delta t), \quad \psi^o \equiv \psi(t), \quad \psi^{oo} \equiv \psi(t-\Delta t).$$

7.3.1 1st order explicit scheme

$$u_P^n = u_P^o + \frac{\Delta t}{V_P}\left[-\sum_f F_f u_f^o + \nu \sum_f S_f \cdot (\nabla u)_f^o - \frac{1}{\rho}\sum_f p_f S_f\right]$$

For this scheme, the truncation error for the time derivative scales linearly with Δt in the asymptotic limit $\Delta t \to 0$, i.e., it is a first order accurate scheme. Since no coupled linear system needs to be solved, it is computationally inexpensive. However, it is subject to a restriction on the Courant number, Co, where, for the scheme to be stable,

$$Co = \frac{u_f \Delta t}{||d_f||} \leq 1,$$

needs to be satisfied, with $d_f = \overline{PN}$ being the vector from the point x_P to the neighbouring point x_N, such that the length of the vector is the grid size.

7.3.2 1st order implicit scheme

$$\frac{u_P^n - u_P^o}{\Delta t} V_P + \sum_f F_f u_f^n - \nu \sum_f S_f \cdot (\nabla u)_f^n = -\frac{1}{\rho}\sum_f p_f S_f$$

Like the explicit scheme, this is also first order accurate, but the system is stable even if the Courant number limit is violated. Of course, for a time resolved problem, the Courant number should not be too large.

7.3.3 2nd order implicit/backward scheme

$$\frac{\frac{3}{2}u_P^n - 2u_P^o + \frac{1}{2}u_P^{oo}}{\Delta t} V_P + \sum_f F_f u_f^n - \nu \sum_f S_f \cdot (\nabla u)_f^n = -\frac{1}{\rho}\sum_f p_f S_f$$

This scheme is second order accurate, unlike the two schemes above, and is used for the studies in this thesis. Note the extra storage required with this scheme. Further details of the numerical methods used in the different flows are given in the individual papers related to each of the cases.

7.4 Spatial interpolation schemes

7.4.1 Convection term

linear For a face f between two cells P and N, a linear interpolation gives

$$\phi_f = f_x \phi_P + (1 - f_x)\phi_N$$

using the weighting factor $f_x = ||\overline{fN}||/||\overline{PN}||$, where $\overline{ij}$ is the vector from the point x_i to the point x_j. This scheme gives (the optimal) second order accuracy, but unfortunately causes unphysical oscillations for convection dominated flows, and often becomes unstable.

upwind For the upwind scheme, which is only first order accurate, the interpolation depends on the flow direction,

$$\phi_f = \begin{cases} \phi_P & \text{if } F_f \geq 0, \\ \phi_N & \text{if } F_f < 0. \end{cases}$$

This scheme, while stable, is usually considered too diffusive to have practical application (although, is sometimes used with RANS).

blended This scheme tries to remedy the problems of the two schemes above by mixing them together,

$$\phi_f = (\phi_f)_{upwind} + \gamma((\phi_f)_{linear} - (\phi_f)_{upwind}),$$

using a constant blending factor γ. This factor determines how much numerical diffusion will be introduced.

The most popular schemes used at present in OpenFOAM are based on a combination of *linear* and *upwind*, where the "blending factor" depends on the *local* flow conditions. These include so-called *flux-limited* schemes, using a limiter function Ψ,

$$\phi_f = (\phi_f)_{upwind} + \Psi\left[(\phi_f)_{linear} - (\phi_f)_{upwind}\right].$$

Some of these schemes satisfy the *total variation diminishing* (TVD) criterion, where the *total variation* is a way of quantifying the term 'oscillation'.

filteredLinear The FilteredLinear scheme uses the limiter function

$$\Psi = \max(\min(\alpha, 1), 0.8),$$

where α is the function

$$\alpha = 2 - \frac{1}{2}\frac{\min\left(|\phi_N - \phi_P - d_f \cdot (\nabla\phi)_P|, |\phi_N - \phi_P - d_f \cdot (\nabla\phi)_N|\right)}{\max\left(|d_f \cdot (\nabla\phi)_P|, |d_f \cdot (\nabla\phi)_N|\right)},$$

comparing the face gradient with the neighbouring cell gradients, and $d_f = \overline{PN}$ is the vector from the centre point x_P to the centre point x_N. This scheme gives a limit of at most 20% upwind.

limitedLinear LimitedLinear is a TVD scheme which uses the limiter function

$$\Psi = \max(\min(\beta r, 1), 0),$$

where r is the function

$$r = 2\frac{d_f \cdot (\nabla\phi)_i}{\phi_N - \phi_P} - 1,$$

with $i = P$ for $F_f > 0$ and N for $F_f \leq 0$, $\beta = 2/k$ and $0 < k \leq 1$ is a user specified variable. $k = 1$ corresponds to full TVD compliance while small k-values give an approximately linear interpolation.

limitedLinearV If ϕ is a vector field, a different version of LimitedLinear, LimitedLinearV, may be considered. This scheme takes into account the direction of the field, instead of treating the components individually, using a different function r,

$$r = 2\frac{(\phi_N - \phi_P) \cdot (d_f \cdot (\nabla\phi)_i)}{(\phi_N - \phi_P)^2} - 1.$$

7.4.2 Diffusion term

For general polyhedral meshes, the vector from the point x_P to the neighbouring point x_N (sharing the face f), $d_f = \overline{PN}$, need not be parallel to the surface direction S_f. Considering the decomposition

$$S_f = \Delta_f + k_f \tag{7.6}$$

where Δ_f is parallel to d_f, one can write

$$S_f \cdot (\nabla\phi)_f = \Delta_f \cdot (\nabla\phi)_f + k_f \cdot (\nabla\phi)_f = ||\Delta_f||\frac{\phi_N - \phi_P}{||d_f||} + k_f \cdot (\nabla\phi)_f.$$

For the term $k_f \cdot (\nabla\phi)_f$, the non-orthogonal correction (vanishing for rectangular cuboids), the face gradient is calculated from

$$(\nabla\phi)_f = f_x(\nabla\phi)_P + (1 - f_x)(\nabla\phi)_N \tag{7.7}$$

with the weighting factor $f_x = ||\overline{fN}||/||\overline{PN}||$. Both of the above methods for handling the face gradient, the orthogonal contribution and the non-orthogonal correction, are second order accurate. However, eq. (7.7), in addition to having a larger computational molecule, leads to a larger truncation error than for the orthogonal scheme. The decomposition in eq. (7.6) may be chosen in many different ways, such as using

$$\Delta_f = \frac{d_f \cdot S_f}{d_f \cdot d_f} d_f,$$

keeping Δ_f and k_f orthogonal, and therefore $||k_f||$ to a minimum, called the *minimum correction approach*, or

$$\Delta_f = \frac{d_f}{||d_f||} ||S_f||,$$

keeping the orthogonal contribution the same as for an orthogonal mesh, called the *orthogonal correction approach.* For all these methods, k_f is in turn calculated from eq. (7.6).

7.4.3 Pressure gradient

Linear interpolation is typically used for the pressure gradient, and so also here.

7.5 Pressure-velocity coupling

Solving for the divergence free criterion simultaneously with the Navier-Stokes equation becomes a very expensive procedure for large systems, and so a segregated approach is usually taken. This means that the parts are solved for separately, using some form of coupling procedure. In OpenFOAM, the PISO (*Pressure Implicit with Splitting of Operators*) algorithm has been used. Also, wanting to avoid the use of a nonlinear system solver, the flux term F_f for the convection is lagged. Finally note that even though there may be conservation at the discrete level for the finite volume method, it may be undone at the solver level.

7.5.1 PISO-algorithm

Consider the semi-discretized form of the Navier-Stokes equation,

$$a_P u_P = H(u) - \nabla p, \tag{7.8}$$

where

$$H(u) = -\sum_N a_N u_N + \frac{1}{\Delta t} u_P^o. \tag{7.9}$$

Interpolating the velocity onto the cell faces, using eq. (7.8), gives

$$u_f = \left(\frac{H(u)}{a_P}\right)_f - \left(\frac{1}{a_P}\right)_f (\nabla p)_f,$$

and therefore for the flux

$$F_f = S_f \cdot u_f = S_f \cdot \left[\left(\frac{H(u)}{a_P}\right)_f - \left(\frac{1}{a_P}\right)_f (\nabla p)_f\right]. \tag{7.10}$$

It then follows from the continuity equation, eq. (7.5), that

$$\sum_f S_f \cdot \left[\left(\frac{1}{a_P}\right)_f (\nabla p)_f\right] = \sum_f S_f \cdot \left(\frac{H(u)}{a_P}\right)_f. \tag{7.11}$$

The steps followed in the PISO algorithm:

1. Predictor step: solve eq. (7.8) for an estimate of the velocity field, using the pressure field from the previous time step.
2. Recalculate $H(u)$ from eq. (7.9) using the new velocity field.
3. Solve for the pressure field using eq. (7.11).
4. Corrector step: update the fluxes in eq. (7.10) (using the new pressure field), and update u_P using eq. (7.8) treating the terms on the RHS explicitly.
5. Possibly go to step 2.

Two corrector steps, following the work by Issa [28], should be sufficient for most cases. Note that the coefficients a_N in $H(u)$, containing the fluxes, are only updated before each new predictor step, and not after the corrector steps. This is in line with the belief that the nonlinear coupling is less important than the pressure-velocity coupling.

Chapter 8

Turbulent flow through straight and curved pipes

Transport of fluids in pipes is very common in many applications, such as in water distribution systems, oil pipelines, heat exchangers, flow through blood vessels, etc. Large pipe networks include joints and bends, along with pipes with varying diameters and surface roughness. An important measure of efficiency for these systems is the resulting pressure drop, or head loss, since it translates into the energy input needed to sustain a specific mass flow rate. The pressure drop generally increases, compared to fully developed pipe flow, for e.g. pipe bends and entry regions when the flow is still developing. Also, since the velocity profile changes, the wall shear stress is not homogeneous along the pipe. Another important measure, connected to the momentum transfer, is the heat transfer characteristics, where entry regions and bends may cause significant increases in the heat transfer rate [82, 53, 64]. Therefore, a good understanding of the flow is needed for efficient heating and cooling. A very different type of phenomenon, which nevertheless may be significant, is the potential of flow induced vibrations. In particular, oscillations in piping systems may cause fatigue. This section will especially focus on the so-called swirl switching phenomenon, which is a large scale oscillation of the flow after a bend. It will also involve the cause of these oscillations, which is believed to be large scale structures created in the upstream turbulent pipe flow. Finally, note that pipes with circular cross section often are considered in practice, since they can withstand large pressure differences between the inside and outside.

8.1 Pipe flow

8.1.1 Laminar pipe flow

Laminar cylindrical pipe flow, or Poiseuille/Hagen-Poiseuille flow, is one of the few exceptions where an analytic solution to the Navier-Stokes equations exist.

For a fully developed flow, the velocity field takes the form $\vec{u} = (0, 0, u_z)$, where

$$u_z = 2U_{bulk}\left(1 - \frac{r^2}{r_o^2}\right), \tag{8.1}$$

in cylindrical coordinates. Here, r_o is the pipe radius and U_{bulk} is the bulk speed. Note that while the fully developed flow is parallel, the flow in the entrance region is not parallel, which can be seen from the continuity equation since $\partial u_z/\partial z < 0$ in the boundary layer. The profile in eq. (8.1) gives rise to a shear stress τ_{zr} in the axial (z) direction,

$$\tau_{zr} = \mu\left(\frac{\partial u_r}{\partial z} + \frac{\partial u_z}{\partial r}\right) = -4\mu\frac{U_{bulk}}{r_o}\frac{r}{r_o}.$$

In particular, the wall shear stress becomes $\tau_w = 4\mu U_{bulk}/r_o$. Furthermore, the pressure drop Δp, over a length L, is often written as

$$\Delta p = f\frac{L}{D}\frac{\rho U_{bulk}^2}{2}, \tag{8.2}$$

where $D = 2r_o$, and f, called the Darcy friction factor, is given by

$$f = \frac{8\tau_w}{\rho U_{bulk}^2}.$$

The friction factor for the fully developed laminar pipe flow, inserting the expression for the wall shear stress, takes the form $f = 64/Re$. It should be noted the friction factor in this case only depends on the Reynolds number, and makes no reference to the surface roughness. For more general situations, including turbulent flow and non-cylindrical pipes, eq. (8.2) is still typically used. However, the friction factor most likely has to be determined empirically.

8.1.2 Transitional pipe flow

While the profile given by eq. (8.1) is a solution for all Reynolds numbers, it starts to become sensitive to disturbances for Reynolds numbers larger than $Re \approx 2000$. As already mentioned in Section (2.2.3), cylindrical pipe flow is unconditionally stable to small disturbances for all Reynolds numbers. Therefore, in theory, the laminar profile should be able to be sustained up to any Reynolds number, given that the disturbance level is kept sufficiently low. However, the flow has been seen to become more sensitive to disturbances for higher Reynolds numbers, lowering the threshold for a potential transition [15]. As a practical consequence, the flow will eventually transition to a turbulent state, since disturbances are unavoidable in real situations.

Compared to flows showing linear instability to small disturbances, such as Taylor-Couette flow, where a typically small succession of states can be found when going from a steady laminar to a turbulent state, no "simple" intermediate states have been found for pipe flow. Also, transitional states in pipe flow may show intermittent behaviour, where the "transient turbulence" eventually decays. However, for large Reynolds numbers, the decay time may be very large. Besides the size of the disturbance, the shape of the disturbance is of course also important. The edge between relaminarization and sustained turbulence, even for a given disturbance profile, may be rather complicated [15].

8.1.3 Turbulent pipe flow

Turbulence in wall-bounded flow is quite different from the situation outlined in Section (2.3). As stated by Jiménez & Kawahara [11], *"the main emphasis in wall turbulence is not on the local inertial energy cascade, but on the interplay between different scales at different distances from the wall"*. Because of the presence of the wall, the viscosity dominates over the inertial effects, also at the large scales, at distances sufficiently close to the wall at any Reynolds number. Of course, it should be noted that the size of the "large" scales change with the wall distance. Close to the wall, the energy containing and dissipative range are at similar scales. In contrast, for free shear flows the inertial effects dominate at the large scales in the entire flow. Furthermore, compared to the laminar flow of eq. (8.1), there is no closed form solution for the mean velocity field of high Reynolds number pipe flow. To simplify the analysis of wall-bounded flows, the boundary layer is divided into different regions.

In order to make the separation into different layers/regions, some form of scaling should be performed. There are two sets of scaling parameters in use. The first set is based on the viscous scale, with length ν/u_τ and time ν/u_τ^2, where u_τ is the so-called friction velocity,

$$u_\tau \equiv \sqrt{\nu \left. \frac{d\langle u_z\rangle}{dy}\right|_{y=0}},$$

using the mean streamwise velocity $\langle u_z\rangle$, and the wall normal distance y ($y = r_o - r$), $u_z(y=0) = 0$. Quantities normalized using ν and u_τ, called wall units, are referenced by a superscript '+'. In particular, the normalized wall distance y^+ is typically utilized,

$$y^+ \equiv \frac{u_\tau y}{\nu}.$$

y^+ may be viewed as a Reynolds number, since the size of the flow structures are constrained by the presence of the wall (cf. eq. (2.18)). The second set of scaling parameters is based on the pipe radius/channel half-height/boundary layer thickness, denoted by δ, where a time may be obtained using e.g. U_{bulk}. A rough classification of the flow by wall distance is given by Pope [52]:

- Viscous sublayer: $y^+ < 5$
- Buffer layer: $5 < y^+ < 30$
- Log-law region: $y^+ > 30$, $y < 0.3\delta$
- Viscous wall region: $y^+ < 50$

- Inner layer: $y < 0.1\delta$
- Outer layer: $y^+ > 50$

In the viscous sublayer, the flow is completely dominated by viscosity. Thus, while the mean flow may change rapidly in the wall normal direction, the level of fluctuations is low. The axial velocity in this region is given by $u_z^+ = y^+$ to a very good approximation. The thickness of the viscous sublayer reduces with higher bulk speed and increases with higher viscosity. In the buffer layer, both viscosity and Reynolds stresses are important. The region is significant since it involves a peak in production of turbulence kinetic energy. However, at sufficiently high Reynolds numbers, the majority of the production has moved into the logarithmic region [67]. This feature, moving the bulk of the production to larger scales away from the wall, should be encouraging for LES. No widely accepted (phenomenological) expression for $\langle u_z \rangle$ exists for the buffer layer. In the logarithmic, or log-law, region, the mean flow is argued to scale as

$$u_z^+ = \kappa^{-1} \log(y^+) + B$$

where κ is called the von Karman constant. Note that for high Reynolds numbers, almost the entire velocity drop towards the wall takes place within, or below, the logarithmic layer.

While the above classification into layers is useful, it is only an approximation, and the layers are not independent. In particular, the large log and outer layer structures have been seen to modulate the near-wall motion. The flow structures of wall-bounded turbulence may be divided into four principal elements, near-wall streaks, hairpin/horseshoe vortices, Large-Scale Motions (LSM), and Very-Large-Scale Motions (VLSM) or superstructures [67]. The hairpin/horseshoe elements, however, perhaps should be replaced by quasi-streamwise vortices. While the notion of structures in turbulence is by no means uncontroversial, the above classification will be considered in this thesis. The "clarity" of the structures very much depends on where, that is at what distance from the wall, they are found. In particular, structures in the viscous sublayer and buffer layer should look "nice", while in the log and outer layer the flow is highly turbulent, and the associated structures become more fractured.

Streamwise streaks and quasi-streamwise vortices have been found to dominate in the region below $y^+ \approx 100$ [11]. The streamwise streaks may be very long, on the order of $10^3 - 10^4$ wall units, and the quasi-streamwise vortices are slightly tilting away from the wall. These streaks and vortices, especially in the viscous sublayer and the buffer layer, are believed to be part of a regenerating (self-sustained) process. The quasi-streamwise vortices move (lift) low streamwise velocity regions close to the wall into higher streamwise velocity regions further away from the wall, and vice versa, creating low and high streamwise velocity streaks, respectively. At some point, the low velocity streaks get (rapidly) ejected further into the high velocity region, where they eventually become unstable and wavy, creating streamwise vorticity (and finer-scale motions) in the process. Accompanying the ejection process is the sweeping of high velocity fluid into the near-wall layer. A strong quasi-periodic bursting results from this cycle. The corresponding situation also occurs for the high streamwise velocity streaks, which move further towards the wall. The high speed streaks are however shorter on average, which is thought to be connected to the higher streamwise velocity gradient in the wall-normal direction, which increases the dissipation. The symmetry between the high and low speed streaks is restored in the outer layer. While quasi-streamwise vortices are considered in the above regeneration cycle, similar sets of events have instead been proposed for hairpins, as well as other types of vortical structures. Compared to the quasi-streamwise vortices, the hairpins are typically not considered to be elongated in the streamwise direction. The common thread, for these ideas of streak generation, is that the patterns of the streaks are determined by the patterns of the vortices [10]. Note that the streaks are easier to observe, in experiments and DNS, than the patterns of wall normal motion giving rise to the streaks.

The near-wall structures are believed to give Reynolds number independent statistics, where the actual Reynolds number dependence comes from the influence of the log and outer layer structures on the near-wall motion. In the log layer and outer layer, the focus shifts to the LSM and VLSM. The LSM, also called turbulent bulges, have sizes comparable to the pipe radius, while the VLSM are usually much longer. Since the VLSM are believed to be especially important for the flow in curved pipes, these motions are the primary focus in the section below, with the LSM being of secondary importance.

Very-large-scale motion

VLSM are long regions of mainly streamwise velocity fluctuations, universally present in pipe, channel, and zero pressure gradient (ZPG) boundary layer flows. The definition in Guala *et al.* [18] divides structures with streamwise extent from $0.1\pi\delta$ to $\pi\delta$ into LSM, and those with streamwise extent above $\pi\delta$ into VLSM.

The first emphasis on VLSM came from experimental pipe flow studies by Kim & Adrian [32]. The length of the structures, estimated using spectra from point data, obtained by hot-film anemometry, was 12-14 radii. Monty *et al.* [41], using a hot-wire *rake* to study pipe and channel flow, found streamwise meandering structures with lengths up to 25δ. Large radial and azimuthal extent of the VLSM were seen in pipe flow experiments by Bailey & Smits [2]. In particular, using two hot-wire probes with varying relative positions, energetic flow modes with a narrow range of azimuthal wavenumbers, peaking at $m = 3$, were seen. In pipe flow experiments with $Re \approx 2 \cdot 10^5 - 4 \cdot 10^5$, Guala *et al.* [18] found that roughly half of the fluctuation energy, based on the streamwise velocity, were contained in the VLSM.

In attempting to explain the mechanism behind the formation of VLSM, Kim & Adrian [32] proposed that *"the VLSMs are not a new type of eddy, but merely the consequence of coherence in the pattern of hairpin packets"*. This mechanism however runs counter to the findings of Hwang & Cossu [25], who found similar types of structures using LES. By using increasingly larger values of the Smagorinsky coefficient (C_S, see Section (5.2.1)), the small scales could be quenched, while the VLSM were retained in the flow. This showed how these types of motions can appear without the agglomeration of small scale structures. These results, together with additional results in Hwang & Cossu [26], led them to infer a *large range of autonomous self-sustained processes*, with scales ranging from the buffer layer to the outer layer.

The self-sustained processes at the different scales were believed to be the type of "coherent lift-up effect" shown by del Álamo and Jiménez [12]. In the turbulent channel flow study, where the mean is used as the base flow, the global modes all decay while the structures with the largest transient growth are reminiscent of the near-wall streaks (in the viscous wall region) and the VLSM (in the outer layer). The independence of the structures in the outer region to the details of the wall is also supported by Flores *et al.* [45], where DNS using smooth and rough walls is considered. In this case, it is thought that the structures in the outer region are either created away from the wall, or they are formed at the wall but quickly forget their origin.

8.2 Flow through curved pipes

8.2.1 Laminar flow through curved pipes

A new layer of complexity can be added to pipe flow by bending the pipe. Generally, this leads to additional pressure losses, and an uneven distribution of wall shear stresses. An important dimensionless geometrical parameter for these flows is the curvature ratio $\gamma \equiv r_o/R_b$, where r_o is the pipe radius and R_b is the curvature radius of the bend. Additionally, the Reynolds number, Re, is equally important as for all viscous flow. However, for a fully developed flow in a very gradual bend, $\gamma \ll 1$, the two numbers can be combined into a single similarity parameter

$$De = \sqrt{\gamma} Re,$$

called the Dean number. Note that there exists other definitions of the Dean number, possibly including the axial pressure gradient. Expanding the solutions in powers of the Dean number, the Poiseuille flow naturally appears to leading order. The higher order terms act as perturbations from the Poiseuille flow, inducing a secondary flow. The secondary flow result from a centrifugal instability caused by the slower moving fluid at the outer wall. This leads to two counter rotating vortices, called the Dean vortices, which create a secondary boundary layer with the flow moving along the wall from the outer side to the inner side of the bend. The Dean vortices also move the high speed core towards the wall, creating larger velocity gradients on the outer side of the bend, along with smaller ones on the inner side. The higher gradients of the axial velocity can result in a significant increase in the flow resistance and dissipation rate. For larger Dean numbers, the secondary flow becomes stronger, and, in particular, the high axial velocity region becomes spread out along the outer side of the bend. Note that the instability also can appear in inviscid flow, given that the incoming velocity distribution is non-uniform. While a separate section concerning transitional flow will not be given here, transition has been seen to be delayed compared to straight pipes. Further information regarding primarily laminar flow in curved pipes can be found in the review article by Berger *et al.* [3].

8.2.2 Swirl switching for 90° curved pipes

The first to carefully study the unsteady behaviour of turbulent flow through sharp 90° bends were Tunstall & Harvey [75]. While looking at flow through pipe bends in the limit $\gamma \to \infty$, with Reynolds numbers of at most $Re = 2.17 \cdot 10^5$, they found a phenomenon that had not been observed earlier for laminar flow in gradual bends. The phenomenon, called *swirl switching*, involves a net swirl (circulation) downstream of the bend, where the swirl direction changes with time. The swirling motion involved a helical flow along the wall, appearing at small distances downstream of the bend, where no trace of the Dean vortices could be seen. The swirl switching was characterized as abrupt, with the flow jumping between two bi-stable states, and was claimed to be caused by a switching of the asymmetrical separation bubble on the inner side after the bend. The dimensionless frequency of the switching, which was considered to be random, peaked around $St \approx 0.001$ to 0.004 in the Reynolds number range $Re = 1 \cdot 10^5$ to $2 \cdot 10^5$. The trend of smaller dimensionless frequencies (i.e. Strouhal numbers) for lower bulk speed continued down to $Re \approx 5 \cdot 10^4$, beyond which no spectral data was provided. It should be noted how the frequencies are clearly much lower than would be expected for ordinary vortex shedding or large scale shear-layer fluctuations. Lowering the velocity was not only seen to reduce the frequency, but was also seen to significantly reduce the strength of the switching. The flow pattern, however, did not fundamentally change as the bulk velocity was reduced, until it was low enough for the flow to be laminar, after which the switching stopped. To make sure that the results did not depend on the sharp corners of the miter bend, they also tried using smooth corners, both inner (at most with an effective $\gamma = 0.5$) and outer, and still saw the same phenomenon. The proposed mechanism for the switching was the occasional existence of a sufficiently strong net axial circulation in the turbulent flow upstream of the bend, which would change the separation bubble from one state to the other. Two conditions were believed to be necessary for the swirl switching to occur. First, the bend should be acute enough to cause separation, and second, the flow entering the bend should be of at least moderate Reynolds number, and probably turbulent.

Another experimental study was performed by Brücker [6], where $\gamma = 0.5$ and the lower Reynolds numbers $Re = 2000$ and 5000 were considered. In this case PIV was used, with measurements at 0D, 1D, and 1.5D downstream of the bend. While no helical flow was seen as for Tunstall & Harvey [75], a switching in the strength of the Dean cells was clearly seen for $Re = 5000$, where the upper/lower cell became dominant. Associated with the switching in strength was roughly a rotation of the plane of symmetry of the vortices about the geometric plane of symmetry of the bend. Two dominant frequencies were found in the tangential flow, $St = 0.03$ and 0.12. Most of the results were given at 1.5D, where these effects were the strongest. The mechanism proposed for the switching involved a self-induced motion of the (Dean) vortex pair.

For a sharp bend with $\gamma = 1.0$, and $Re = 1.8 \cdot 10^4$, PIV at a distance 5.3D downstream of the bend was considered by Hellström *et al.* [21]. A swirl switching phenomenon, involving a single vortex along the lines of Tunstall & Harvey [75], was observed. However, the switching frequency was $St \approx 0.6$, which is clearly much higher than the frequency given by Tunstall & Harvey [75]. While an intermittent appearance of the Dean motions was highlighted, there was no discussion regarding the discrepancy in the frequencies.

In the LES investigation by Rütten *et al.* [56], two different curvature ratios, $\gamma = 0.17$ and $\gamma = 0.5$, along with three different Reynolds numbers, $Re = 5000$, 10000, and 27000, were studied. Looking at the forces on the pipe walls, a peak in the range $St \approx 0.1 - 0.3$ was seen for all cases. However, at $\gamma = 0.5$ the flow separated at every considered Reynolds number, which led to a broadening of the peak compared to the cases with $\gamma = 0.17$, where there was no separation for any of the Reynolds numbers. Furthermore, for the cases with the highest Reynolds number, $Re = 27000$, a low frequency contribution was also seen. Looking at the position of the outer stagnation point, the low frequency was found to represent the alternating strength of the upper/lower Dean cell, giving a net swirl, which is more in line with the experimental results of Brücker [6]. The transition between the two extremes of the stagnation point, at roughly ±40°, was gradual. Also, in contrast to the proposition put forward by Tunstall & Harvey [75], no flow separation was needed for this type of swirl switching to take place.

In a recent PIV study by Hellström *et al.* [20], structures at 5D, 12D, and 18D after the bend were extracted using POD. The curvature ratio was $\gamma = 0.5$ and the Reynolds number $Re = 2.5 \cdot 10^4$. The first POD mode showed a single vortex at all downstream locations, and the spectrum of the time coefficients at 5D showed a peak at $St = 0.33$. The second and third POD modes showed "tilted" Dean motions, in particular at the first downstream location (5D), with the two modes being roughly mirror images in the symmetry plane. In addition to being rotated about the symmetry plane, one of the cells was suppressed. The time coefficients of POD mode 2 at 5D showed a peak at $St = 0.16$. The (tilted) Dean motion was believed to be a transitional state between the single vortex states, with one of the Dean cells getting suppressed, suggested to be triggered by an instability at the inner bend.

Another recent experimental study, for a Reynolds number $Re = 3.4 \cdot 10^4$ and a bend with $\gamma = 0.32$, was performed by Kalpakli & Örlü [30]. A POD analysis of PIV data was considered, and a similar sort of "weak" swirl switching was seen as by Brücker [6] and Rütten *et al.* [56]. Also in this case, the switching was gradual, and not abrupt. The switching frequency was found to be at $St \approx 0.04$, but other strong frequencies were also present in the flow, $St \approx 0.12, 0.18$. As stated by Kalpakli & Örlü [30], regarding the swirl switching phenomenon, *"the mechanism which triggers such a motion is not fully understood yet and studies investigating its origin are still ongoing".*

In summary, the nature of the switching, and the time scales involved, varies substantially in the literature. In particular, the role of unsteady Dean motion in contrast to a dominant single cell (giving helical flow) is unclear, or as stated in [76], the role of "rocking" and "rolling" is unclear, as well as the role of the inner separation bubble after sharp bends. The (dimensionless) frequency of the switching ranges from $St \approx 0.01$ in Rütten *et al.* [56], and even less for Tunstall & Harvey [75], to $St \approx 0.6$ in Hellström *et al.* [21]. The baseline case in this study follows the experimental work of Kalpakli & Örlü [30], who found a gradual switching at $St \approx 0.04$. With this background, particularly highlighting the confusion surrounding the large span of time scales involved, the main question to answer may be stated:

- What is the origin of the swirl switching phenomenon?

8.3 Results

To be able to answer the above question, fully developed turbulent flow through 90° curved pipes were investigated using LES, considering four different curvature ratios. The upstream flow was generated in a straight pipe with cyclic boundary conditions, described in Section (8.3.1), and then used as an inlet condition for the curved pipes, Section (8.3.2).

8.3.1 Results - Turbulent pipe flow

The inlet flow to the curved pipes was generated using a straight pipe with cyclic boundary conditions. The pipe was seven diameters long, and the Reynolds number, based on the pipe diameter and the axial bulk velocity U_{bulk}, was $Re = 34000$. A spectrum using the axial velocity is shown in Fig. (8.1), where the Strouhal number is based on the pipe diameter and the axial bulk velocity. The energetic low frequency motion at $St \lesssim 0.01$ and $St \approx 0.13$ are observed, which would imply the presence of VLSM. Structures giving frequencies below $St = 0.5$, considering the whole cross section of the flow, were shown to contain 40% of the axial fluctuation energy.

A POD analysis was carried out, for all three velocity components, on a cross section of the pipe. The dominant fluctuating POD mode, representing a VLSM, is given in Fig. (8.2). The figure implies a lift-up process [72], where the high-speed streaks move outward towards the low-speed fluid at the wall, while the low-speed streaks move inward, towards the high-speed fluid in the centre.

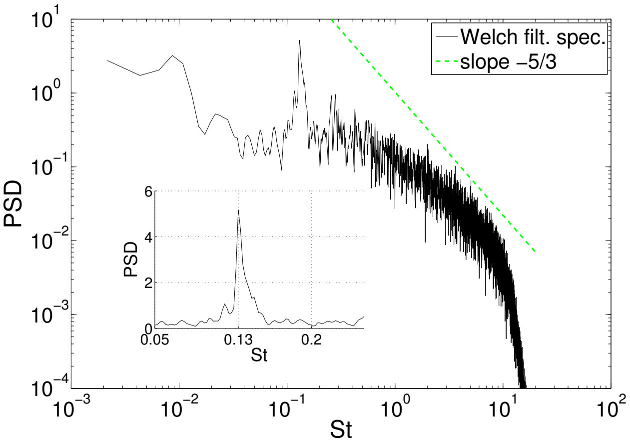

Figure 8.1: Power spectral density of the axial velocity, at a point $0.25r_o$ from the wall, in the straight pipe used to generate the inlet library.

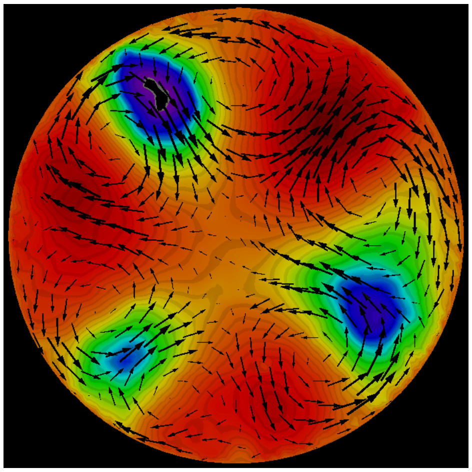

Figure 8.2: POD mode 1, representing a VLSM, using the velocity field on a cross sectional plane. The colour shows the axial component, where red implies an increased flow speed while the blue/black regions imply a decrease.

In order to further investigate the low frequency motions, a POD analysis was conducted on the full pipe flow. The energetic low frequency structures at $St \lesssim 0.01$ and $St \approx 0.13$ are shown at the top (with $m = 2$) and bottom (with $m = 3$), respectively, in Fig. (8.3).

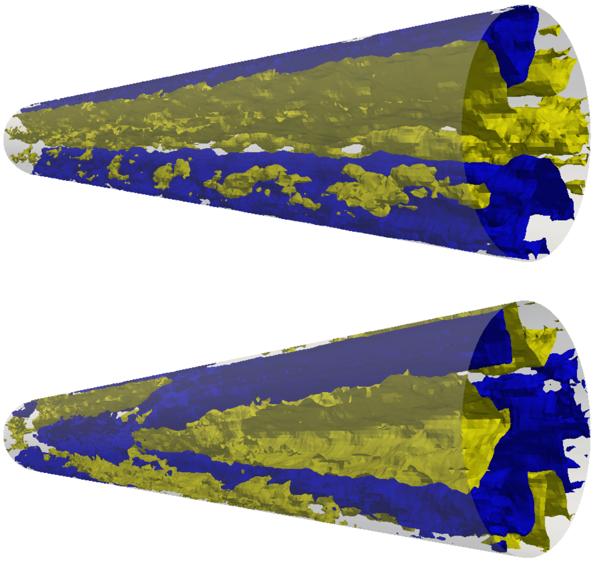

Figure 8.3: Positive/negative isocontours of the axial component of POD mode 1 (top) and 2 (bottom) in the straight pipe with cyclic boundary conditions.

A chaotic time series analysis was performed for the signal giving the spectrum in Fig. (8.1). The data was sampled over $U_{bulk}t/D = 1130$, in steps of $U_{bulk}\Delta t/D = 3.5 \cdot 10^{-3}$, giving a total of $3.2 \cdot 10^5$ samples. To determine the optimal time delay T, the average mutual information, eq. (4.2), is shown as a function of T in Fig. (8.4), using the sample interval 1-50000. The graph gives the value $T = 12$, which is also obtained for the intervals 100001-150000 and 200001-250000.

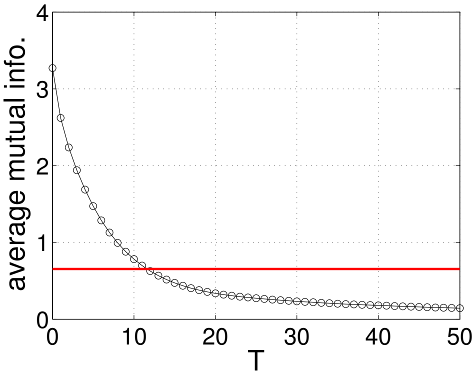

Figure 8.4: The average mutual information for the sample interval 1-50000. The red line shows where $I(T) = I(0)/5$.

A false nearest neighbour analysis (see Section (4.2)), using the first 50000 samples with the delay $T = 12$, gives the result shown in Fig. (8.5). The threshold value was set to $R_T = 15$, and the ratio of false nearest neighbours dropped below 1% at $d_E = 5$.

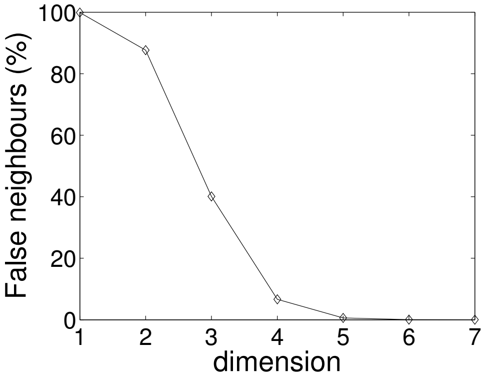

Figure 8.5: False nearest neighbours vs. the embedding dimension for $R_T = 15$.

In calculating the global Lyapunov spectrum the local dimension was in this case set to $d_L = d_G = 5$. The variables (time and velocity) were made dimensionless using U_{bulk} and D. Results for three different intervals are shown in Table (8.1). The similarity of the spectra in the three intervals is encouranging for the validity of the analysis. In addition to the five Lyapunov exponents, the Kaplan-Yorke dimension D_{KY} is also shown, giving a value $D_{KY} = 4.4$.

	1-50k	**100k-150k**	**200k-250k**
λ_1	44.6	48.4	47.9
λ_2	12.4	13.0	12.7
λ_3	-0.8	-0.7	-0.5
λ_4	-17.9	-17.5	-18.0
λ_5	-90.3	-96.9	-93.5
D_{KY}	4.42	4.45	4.45

Table 8.1: Lyapunov exponents λ_i for three different intervals, together with the Kaplan-Yorke dimension D_{KY}.

8.3.2 Results - Swirl switching for 90° curved pipes

Fully developed turbulent flow through curved pipes were investigated while varying the curvature ratio $\gamma \equiv r_o/R_b$, where r_o is the pipe radius and R_b is the radius of curvature of the bend (measured from the centre of the pipe). Four different curvature ratios were considered; $\gamma = 0.32, 0.5, 0.7,$ and 1.0. The curved pipe section of the computational domain can be seen in Fig. (8.6). At the pipe exit, the flow enters into a box with dimensions 16D × 13D × 16D, where a Neumann boundary condition is used for the velocity field.

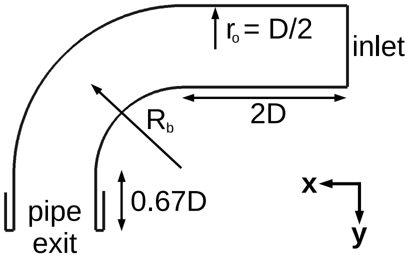

Figure 8.6: Curved pipe section of the computational domain.

A POD analysis was performed using the *in-plane* (x and z) velocity components at the pipe exit. The first two fluctuating POD modes for $\gamma = 0.32$, which is the most gradual bend, are shown at the top in Fig. (8.7). The modes compare favourably with the experimental results by Kalpakli & Örlü [30]. The spectrum of the time coefficients for POD mode 1 is given in Fig. (8.8), where the low frequencies are seen to contribute greatly. The corresponding modes for $\gamma = 0.5$ and 0.7 are similar in structure, but with an increase in the relative energy content of mode 1 for increasing γ.

To get a better sense of the switching, and to provide a further comparison with the results of Kalpakli & Örlü [30], a reconstruction using POD modes 0 and 1 was performed. Since POD modes generally do not vary in a purely sinusoidal fashion, the expression

$$\langle a_o \rangle v_o + \sqrt{2\langle a_1^2 \rangle}\sin(\omega t) v_1 \tag{8.3}$$

was considered, where $\langle a_1 \rangle \approx 0$. The resulting time sequence, showing the behaviour at $\omega t = -\pi/2$, 0, and $\pi/2$, is given in Fig. 8.9. Again, the results compare well with the experimental study.

Using a high-pass filtered inlet flow for $\gamma = 0.32$, removing frequencies below $St = 0.5$, *no swirl switching could be found.* This provides further evidence of the necessity of structures coming from the upstream pipe.

As the bend became sharper, a high frequency ($St \approx 0.5$) swirl switching started to grow strong. Similarly to $\gamma = 0.32$, carrying out a POD analysis on the in-plane velocity components at the pipe exit for $\gamma = 1.0$ gave the modes shown at the bottom in Fig. (8.7). The strong high frequency content for POD mode 1, seen in Fig. (8.8), should be clear. The qualitative difference between POD mode 1 for $\gamma = 0.32$ and $\gamma = 1.0$ should be noted, where the mode for the sharp bend is basically a single vortex.

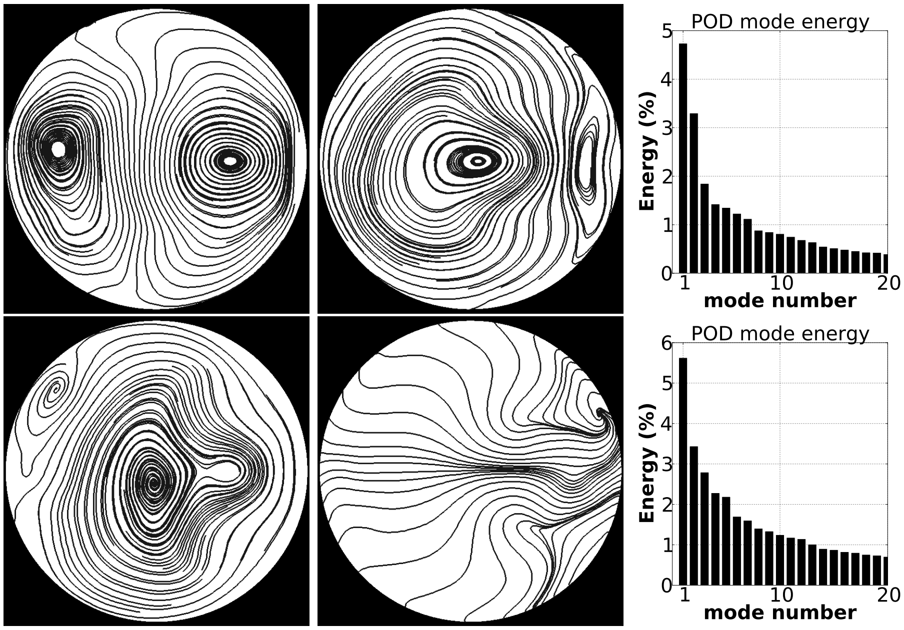

Figure 8.7: POD analysis based on in-plane velocity components at the pipe exit, for $\gamma = 0.32$ (top) and $\gamma = 1.0$ (bottom). POD mode 1 (left) and 2 (middle) are shown, along with the energy distribution amongst the first twenty modes (right). POD mode 0 is not included.

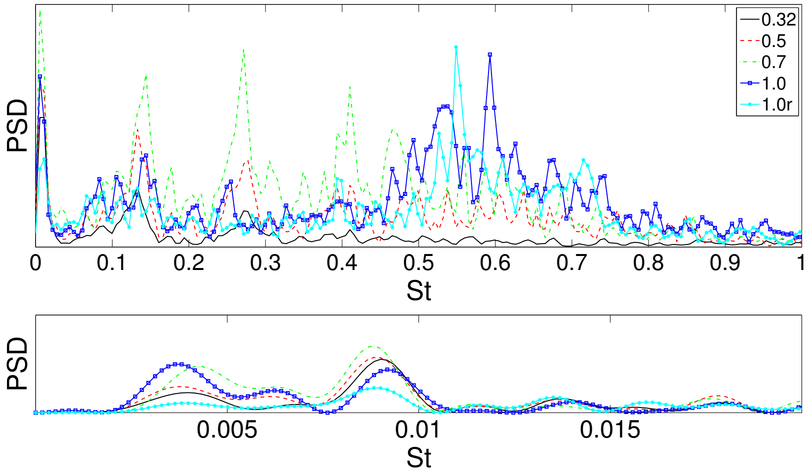

Figure 8.8: Power spectral density of the time coefficients for POD mode 1, obtained using in-plane velocities at the pipe exit. '1.0r' represents a refined grid for $\gamma = 1.0$. Note that the bounds for the upper and lower vertical axes are different.

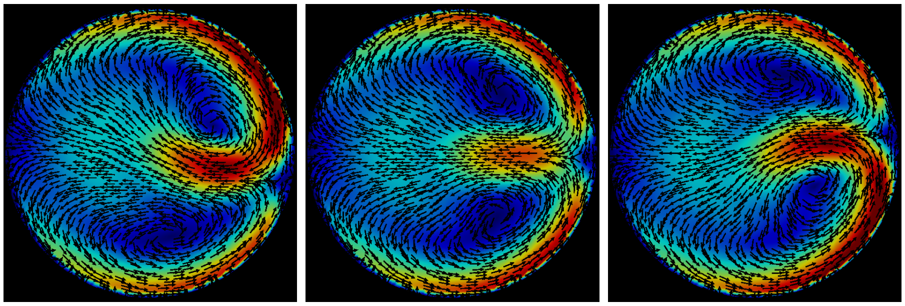

Figure 8.9: Reconstruction for $\gamma = 0.32$ using POD modes 0 and 1, as specified by expression (8.3).

A POD analysis was also carried out using a large three-dimensional region. The most energetic fluctuating POD modes, for $\gamma = 0.32$ and $\gamma = 1.0$, can be seen in Fig. (8.10). Note how the low frequency structure (for $\gamma = 0.32$) comes from the upstream pipe, and is therefore dependent on the upstream flow conditions, while the high frequency structure (for $\gamma = 1.0$) comes from the bend itself, and is therefore considered an inherent property of the system.

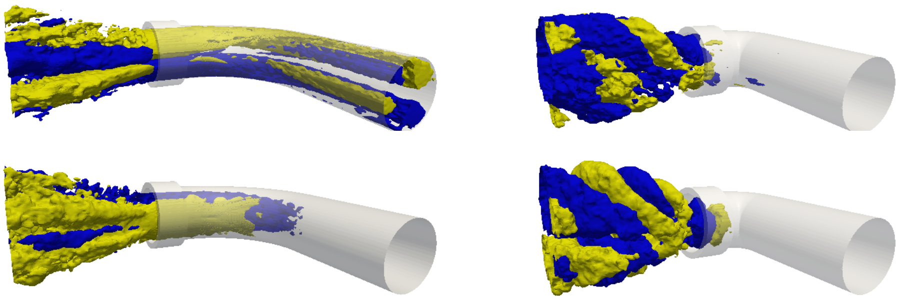

Figure 8.10: Positive/negative (yellow/blue) isosurfaces of POD mode 1 for $\gamma = 0.32$ (left) and $\gamma = 1.0$ (right). Top: x-component (x: normal direction to the inlet plane; positive direction pointing into the geometry), bottom: z-component (z: normal direction to the symmetry plane; positive direction "upward").

8.3.3 Results - Summary

A proposition is made to categorize the swirl switching into two phenomena with two distinct physical origins; one high frequency and one low frequency switching. While the high frequency switching ($St \sim 0.5$), which becomes stronger for sharper bends, originates from structures formed in the bend, and is therefore an inherent feature of the curvature, the low frequency switching seems to originate from large scale structures formed in the upstream turbulent pipe flow. These low frequency structures are believed to be an instance of VLSM. A connection between VLSM and swirl switching is also supported experimentally by Sakakibara & Machida [58].

Chapter 9

Summary of results - Swirl burners

Today's gas turbines typically utilize swirling flows to stabilize the flame. The swirl, together with sudden expansions of the geometries, give rise to divergent flows with a range of velocities to match the flame velocity. The azimuthal shear and centrifugal instabilities associated with swirling flow also result in enhanced mixing and entrainment of the ambient fluid [16], leading to an improved efficiency and a compact flame. The use of swirling flows may be divided into the two categories *high swirl*, which can be regarded as an established technology, and *low swirl*, which is a more recent development. It can be noted that the use of high swirl levels originated with diffusion flames, and was later adopted for premixed combustion.

A *high swirl* level may induce a recirculation zone [36], usually called a *vortex breakdown* (VB), that sends hot combustion products back into contact with the unburned mixture, raising its temperature and thereby *further contributing* to the stabilization. Such additional reinforcements to the stabilization could be vital for robust operation, especially when a wide range of fuels are to be used. However, the lift-off height is often quite low, requiring a cooling system for the burner, and the large swirl levels may cause flash back. Furthermore, the high swirl can induce strong oscillatory behaviour in the flow, such as a *precessing vortex core* (PVC), that may couple with acoustic modes in the combustor or trigger some other resonance of the system, potentially causing great harm.

A more recent complimentary technology is the *low swirl* burner, which generally avoids issues such as PVC and flash back, ideally giving a premixed flame lifted far from any solid surface. Another important goal for most burners is to reduce NO_x production, which follows from decreased combustion temperatures which in turn can be accomplished by using lean mixtures. Very lean mixtures however imply significantly weakened flames, generally resulting in incomplete combustion, high CO and/or unburnt hydrocarbon emissions, and, especially, a system very prone to instabilities.

Results from systems involving high swirl levels are given in Section (9.1), while low swirl configurations are addressed in Section (9.2).

9.1 High swirl - two cold flow studies

Two cases have been studied where high swirl levels were involved. The baseline geometry in the first case, seen in Fig. (9.1), was basically that of a Volvo VT40 gas turbine combustor. The interest for this annular burner rig was the effect of the downstream outlet contraction on the flow inside the main chamber. Therefore, the radius of the outlet pipe, R_0, was used as a control parameter, when the resulting flow was characterized. Note that while all cases considered cold flow, a reacting case has been studied earlier, using the baseline geometry [49]. Here we focus on the following question to be answered:

- Is there any qualitative change in the flow behaviour as the radius of the outlet pipe is varied? And if so what is the mechanism behind.

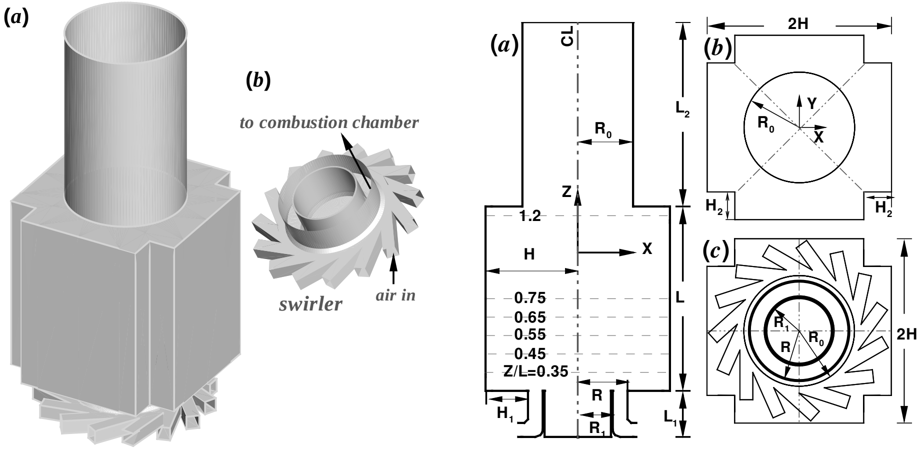

Figure 9.1: Combustor geometry with inlet swirler, for the first high swirl case.

The second case, which may be regarded as a more fundamental study of VB and PVC, used the geometry in Fig. (9.2). Whereas the combustor in Fig. (9.1) used a tangential inlet flow to generate the swirl, this setup uses a swirler with guide vanes. Five cases with different swirl levels and mass flow rates were considered, including three cases with high enough swirl to generate VB at the expansion. In fact, the swirl level was so high in these three cases that it generated a backflow along the centre line in the entire upstream pipe, up to the end of the swirler. Although such backflows in general makes the cases uninteresting for combustion applications, they are still of interest in the general study of swirling flows. The main question to be answered has been:

- What qualitative changes occur as the swirl number increases?

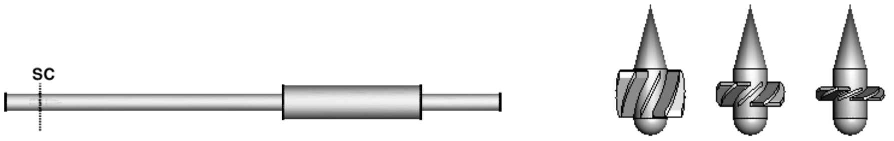

Figure 9.2: Geometry for the second high swirl case. Left: pipe with an expanded section. The flow is from left to right and 'SC' marks the position of the swirler. Right: the three swirlers used, where the blunt side of the swirler faces the inlet.

9.1.1 Results - VT40 burner

Qualitative changes in the *mean* flow behaviour were seen for the VT40-type burner, when the radius of the outlet pipe was changed. Nine different radii were considered, and the flow along the centre line of the main chamber changed from positive axial velocities for small outlet radii (small R_0), to mostly negative axial velocities for the large outlet radii (large R_0). In other words, the VB went from a torus for small R_0 to more of a bubble-type for large R_0, see Fig. (9.3). Additionally, the recirculation bubble inside the outlet pipes for the larger radii is seen to be quenched for the smaller radii.

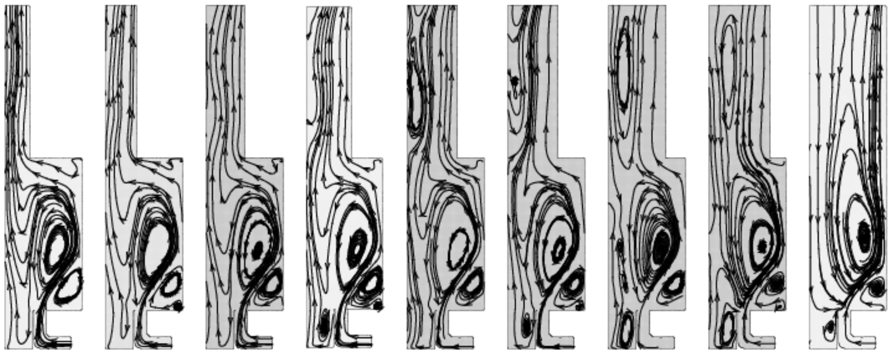

Figure 9.3: Streamlines of the mean flow, using cross sections of half of the combustors, for the nine VT40-type geometries.

Time resolved velocity fields were analysed using the fast Fourier transform (FFT) on point data, as well as POD/DMD of full 3D fields. Spectra at points on the centre axis, for the cases with the smallest and largest outlets, are given in Fig. (9.4). The flow frequencies in general were seen to get higher as the outlet pipe became narrower, along with a larger activity in the pilot chamber.

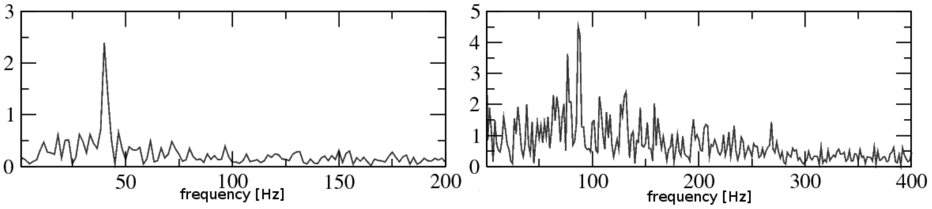

Figure 9.4: Power spectra of radial velocity data on the centre axis. Left: the case with the extended combustor (no outlet pipe), right: the case with the smallest outlet pipe.

The POD and DMD analyses of the velocity fields, obtained in each case using 200 snapshots, implied the existence of two categories of important modes; one with azimuthal wavenumber $|m| = 1$, modes with dipole character, and the other with $|m| = 2$, modes with quadrupole character. The $|m| = 1$ modes were connected to low frequencies, in part due to the low $|m|$ value, and had a large influence along the centre of the combustor, while the high frequency $|m| = 2$ modes started to play a larger role away from the centre line. Numerous energetic POD/DMD modes with $|m| = 1$ were seen for the smallest outlet pipe, covering a range of frequencies. This is also reflected in Fig. (9.4).

Isosurfaces of the radial component of the different types of modes, using the real part of DMD modes, are given in Fig. (9.5). The corresponding imaginary parts are basically just versions of the real parts that are rotated around the centre axis, reflecting the situation of modes spinning around the centre line. For the straight outlet case, the modes are counter-winding and co-rotating, with respect to the mean flow. The larger extent of the $|m| = 1$ mode for the straight outlet case compared to the smallest outlet case, following the discussion regarding the different modes in Fig. (2.6), depends on the larger vortex core. The associated frequencies of the modes for the straight outlet case are $41Hz, St = 0.14$ and $96Hz, St = 0.32$ for the $|m| = 1$ and $|m| = 2$ mode, respectively, while for the smallest outlet pipe it is instead $86Hz, St = 0.29$ and $167Hz, St = 0.56$. The $|m| = 1$ modes correspond well with the frequencies that stand out in the point spectra.

The two types of modes, the dipole and the quadrupole, result from the two vortical regions dictated by the geometry, following the discussion around Fig. (2.6). The combustor inlet is annular, creating an *outer vortex ring*, while the flow in the centre gives an *inner vortex core*. The outer vortex ring, which is more confined by the combustor walls, leads to a $|m| = 2$ deformation, while the inner vortex core, which is less constrained in the combustor and more free to move around, leads to an $|m| = 1$ mode.

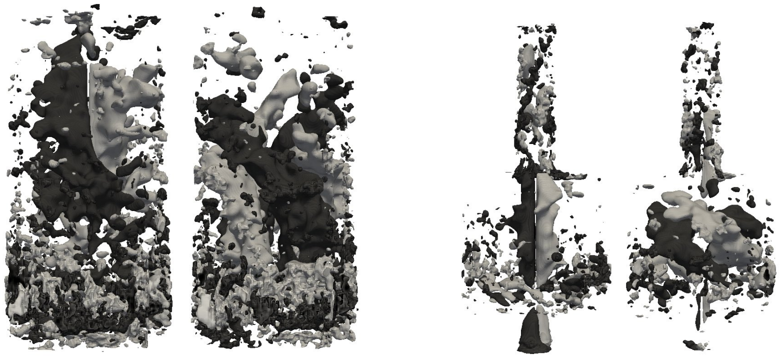

Figure 9.5: Radial parts of DMD modes. Left: the case with the extended combustor (no outlet pipe), right: the case with the smallest outlet pipe. For each geometry the *real part* of the strongest dipole (left) and quadrupole (right) modes are shown.

The POD in this case gave structures that look similar to the DMD modes. The radial component of the first four POD modes, where the POD was based on velocity fluctuations u' (instead of the velocity u), for the cases with the straight outlet and the smallest outlet pipe are shown in Figs. (9.6) and (9.7), respectively. Comparing the two cases, the fluctuations of the inner vortex core are seen to dominate for the smaller outlet. Since the movement of the vortex core is more constrained inside the outlet pipe, focusing on Fig. (9.7), a strong contribution comes from $|m| = 2$ deformations, as opposed to the strong $|m| = 1$ influence inside the chamber, where the vortex core has a greater freedom to move around. Note that the winding inside the small outlet pipe is in the same direction as the mean flow. The corresponding mode energies are given in Fig. (9.8).

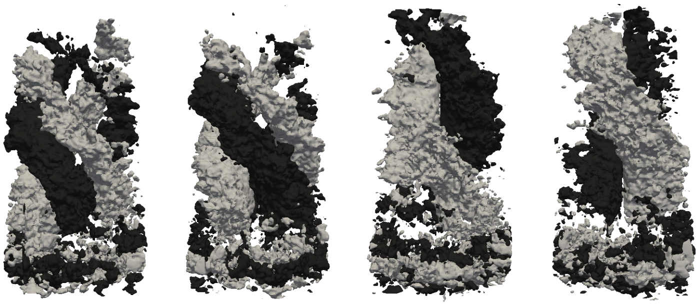

Figure 9.6: Isocontours of the radial component of the first four POD modes for the straight outlet.

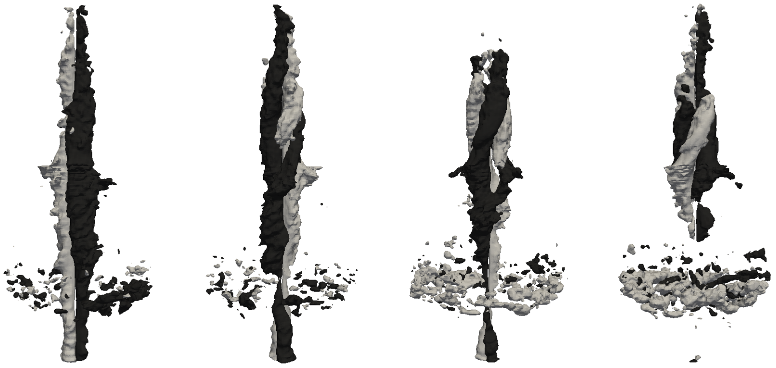

Figure 9.7: Isocontours of the radial component of the first four POD modes for the smallest outlet pipe.

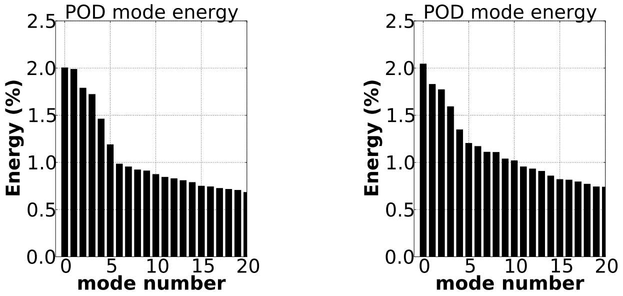

Figure 9.8: POD mode energy of some of the largest modes. The POD analysis was based on velocity fluctuations u'. Left: straight outlet, right: smallest outlet pipe.

9.1.2 Results - Expanding/Contracting pipe

For the swirling pipe flow with the extended section, Fig. (9.2), the qualitative change in the *mean* flow behaviour with increasing swirl was primarily the appearance of VB at the expansion, together with a reversed flow in a large part of the upstream pipe. The axial velocity along the centre-line is shown in Fig. (9.9), where five different cases are considered. The focus below will be only on one of the cases in Paper II, that is the case with swirl number $Sw = 0.76$.

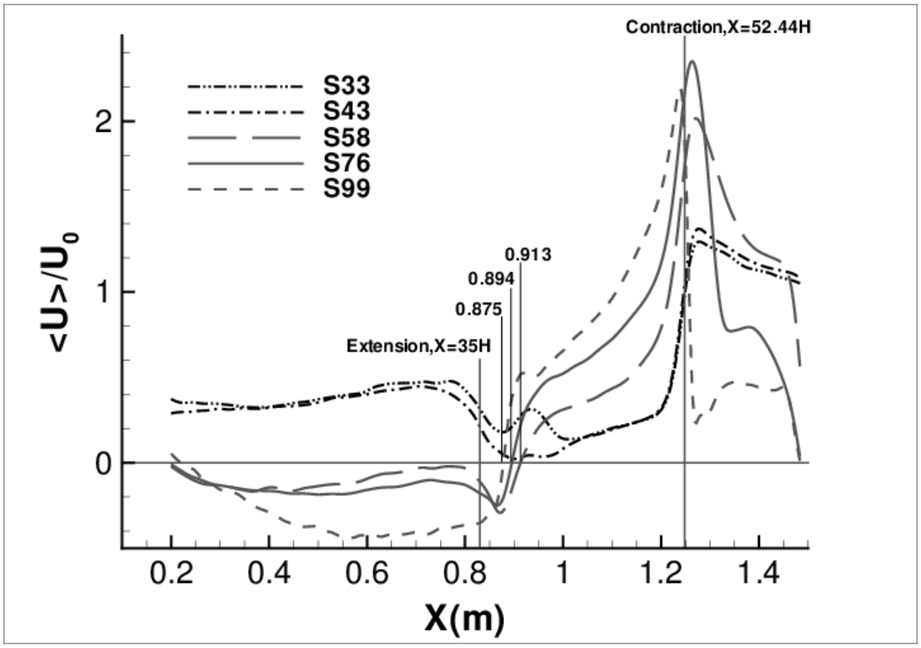

Figure 9.9: Mean axial velocity, normalized using the axial bulk velocity U_0, along the centre line of the pipe in Fig. (9.2), for different swirl levels.

The strongest unsteady flow structure was the PVC at the expansion, whose corresponding DMD mode can be seen in Fig. (9.10). The real and imaginary parts of the DMD mode are given, which represents the structure at two different times, showing the spinning of the mode. The frequency of the spinning is $St = 0.63$ ($f = 33Hz$), with a Strouhal number based on the small pipe diameter $D = 5.06cm$ and the uniform inlet velocity $U_0 = 2.63m/s$. As was already pointed out in Section(2.2.5), in a similar swirling flow experiment, this type of PVC has been seen to result from a supercritical Hopf bifurcation [46].

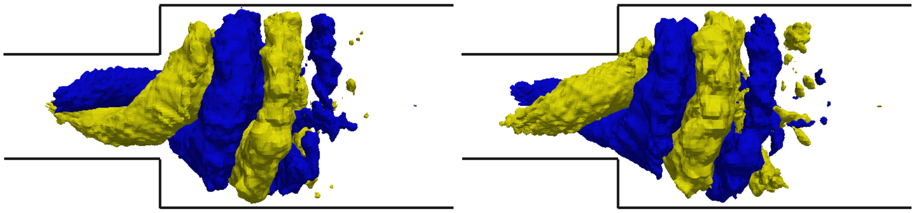

Figure 9.10: Positive/negative isocontours of the radial component of the real (left) and imaginary (right) part of the DMD mode representing the PVC at the expansion, for $Sw = 0.76$.

The DMD mode representing the strongest unsteady flow structure in the upstream pipe is shown in Fig. (9.11). It is a co-rotating and counter-winding $|m| = 2$ mode with the high frequency $St = 2.2$ ($f = 113Hz$). In a simplistic approach, using the axial bulk velocity, a wavelength $\lambda \sim U_0/f \sim (2.63/113)m \approx 2.3cm$ is obtained, which is about half the wavelength in the axial direction, given by Fig. (9.11). A cross section of the mode at $x = 0.4m$ is shown in Fig. (9.12). The mode is seen to span a large part of the cross section, and therefore a large range of axial velocities of the base flow. Recall that there is backflow along the centre axis (see Fig. (9.9)).

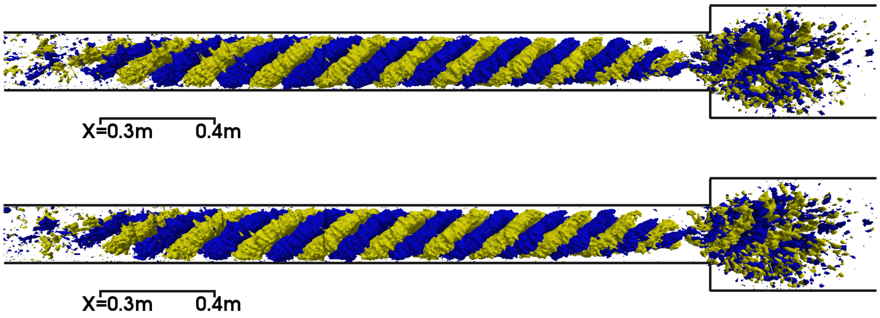

Figure 9.11: Positive/negative isocontours of the radial component of a DMD mode with $St = 2.2$. Real (top) and imaginary (bottom) parts are given.

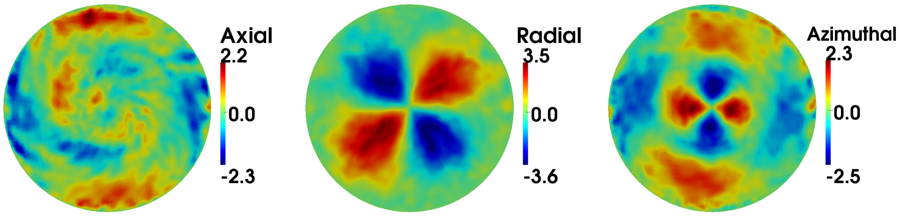

Figure 9.12: Cross section of the real part of the DMD mode in Fig. (9.11) at $x = 0.4m$. Left: axial, middle: radial, right: azimuthal. Note that the values are not physical, and should only be compared amongst each other.

Downstream of the sudden expansion, beyond the structure referred to as the PVC, shown in Fig. (9.10), there is a large influence from low frequency motion. A corresponding low frequency DMD mode, with $St = 0.1$ ($f = 5Hz$), is shown in Fig. (9.13). The mode is seen to have an $|m| = 1$ symmetry in a large part of the extended pipe, and $|m| = 2$ elsewhere. The region a bit upstream and downstream of the contraction is very reminiscent of the VT40 case with the small outlet pipe, given in Fig. (9.7). A strong centre vortex core is seen for the three higher swirl number cases. The behaviour of the mode in the upstream pipe, however, is more curious. Comparing the $|m| = 2$ structure to that seen for the high frequency mode in Fig. (9.11), the axial wavelength appears to be similar. This indicates a sensitivity for this type of mode, spanning over a large range of frequencies. Finally, the Strouhal numbers of the different modes, for the three high swirl cases, are shown in Fig. (9.14). Note that the Strouhal numbers, using the bulk velocity, are defined independently of the swirl number, which may be a factor to be considered for correct scaling of swirling flows. The simplification implies that the frequencies scale with the axial flow, and not the swirl.

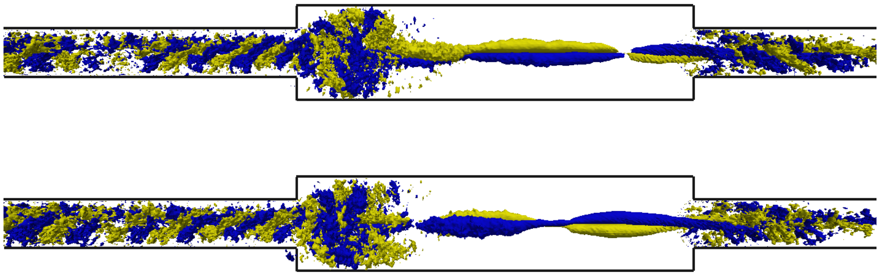

Figure 9.13: Positive/negative isocontours of the radial component of a DMD mode with $St = 0.1$. Real (top) and imaginary (bottom) parts are given.

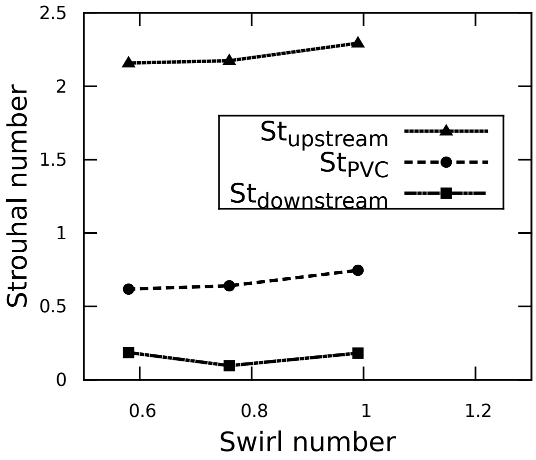

Figure 9.14: Strouhal number as a function of swirl number for the different flow structures found in the pipe with a sudden expansion and contraction.

9.2 Low swirl - stratified premixed combustion

A schematic of the burner geometry used in this study can be seen in Fig. (9.15). The swirling flow is generated in the outer regions of the flow, using eight annular vanes. While the diverging flow at the sudden geometric expansion is the main component to the flame stabilization, an understanding of additional contributions to the (de)stabilization is important to ensure robust operation. The role of the large scale coherent structures that may be formed inside and above the burner on the flame dynamics is of particular concern. In this study, the main question to be answered is:

- How do the large scale coherent structures formed inside the burner affect the flame?

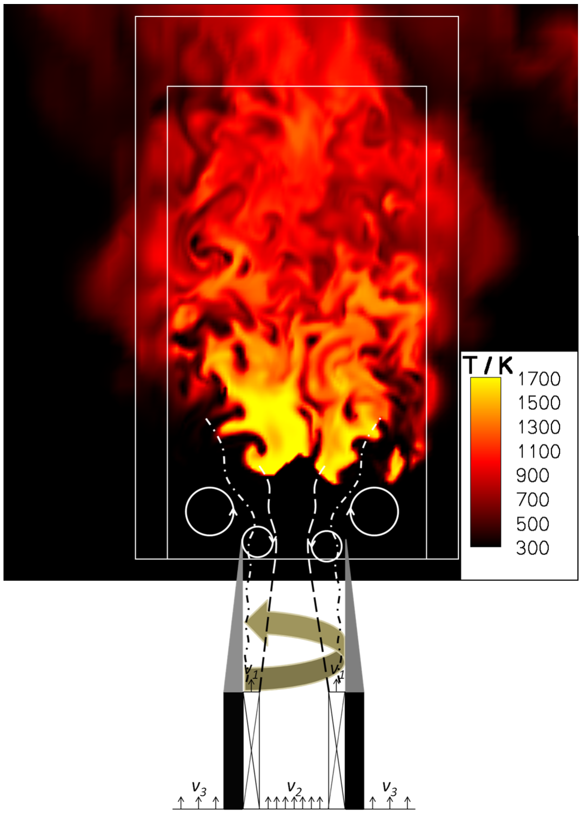

Figure 9.15: Schematic of the low swirl burner setup. $v_1 \sim 10m/s$ represents the flow coming from the eight annular swirl vanes, $v_2 \sim 3m/s$ the flow in the inner region of the burner, and $v_3 \sim 0.35m/s$ the co-flow. The large arrow shows the rotation direction of the flow while the loops represent large coherent structures. The dashed lines mark the inner and outer shear layers.

Simultaneous high-speed PIV and OH PLIF measurements, as well as LES with G-equation simulations for flame-tracking, were performed in an attempt to investigate flow-flame interaction of a turbulent low swirl stratified premixed flame. The flow coming from the burner (v_1 and v_2 in Fig. (9.15)) was a methane/air blend of equivalence ratio $\phi = 0.62$ (lean flammability limit $\phi \approx 0.4$), entering into ambient air (v_3). The Reynolds number, based on burner diameter D and bulk velocity, was Re=20000. The swirl number at the burner outlet, based on integrated flux, was $Sw \sim 0.5$ and did not result in vortex breakdown.

9.2.1 Results

The flame was stabilized, on average, at about $0.64D$ above the burner rim. The flame regime, referring to Fig. (6.1), ranged from the corrugated flamelet regime in the centre above the burner, to the thin reaction zone regime in the outer high-speed regions. With a DMD analysis of the velocity field, the spatial structures giving two strong peaks in the point spectra (no shown), also obtained in an earlier study of the same system [44], could be isolated. The modes, using azimuthal vorticity, are shown in Fig. (9.16). The idea, sketched in Fig. (9.17), is that the structures, particularly the $|m| = 3$ mode as will be argued below, pull the flame downwards in the outer regions. This contributes to the flame stabilization and in giving the flame its wider shape.

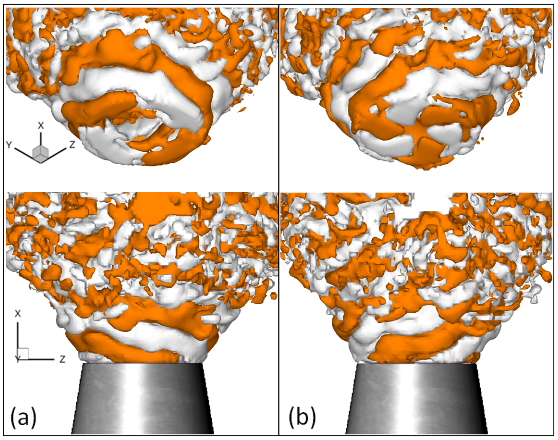

Figure 9.16: Azimuthal vorticity of the real part of two DMD modes from an LES simulation of the low swirl burner, given at two different angles. Left: mode with $|m| = 2$ and dimensionless frequency of 2.9 , right: mode with $|m| = 3$ and dimensionless frequency of 5.3.

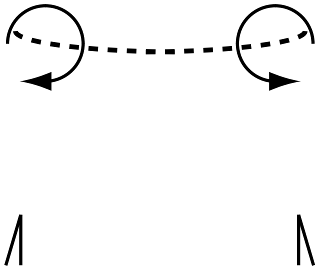

Figure 9.17: Schematic of the structures above the burner anchoring the flame (represented by the dashed line).

For comparison, the first two POD modes are given in Fig. (9.18). No large scale coherent pattern can be seen for mode 1, or any of the higher order modes that were investigated. While POD in this case is not able to separate the frequencies into distinct structures, DMD does so by design.

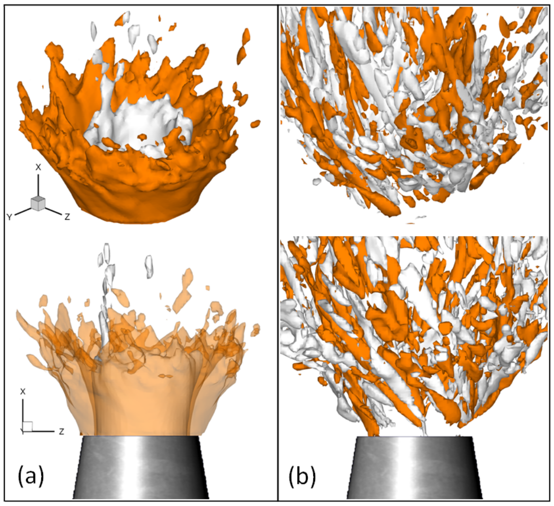

Figure 9.18: Azimuthal vorticity of the two most energetic POD modes. Left: mode 0, right: mode 1.

In order to provide a closer link between the flame and the flow behaviour, an extended DMD (EDMD) analysis was performed, introduced in Section (3.4.2). The DMD analysis is based on the velocity field, while the G-field, which represents the flame (see Section (6.1.1)), is coupled through eq. (3.14). The investigation can be interpreted as giving the effect of the flow field on the flame. This method (as opposed to performing the DMD analysis on the two fields separately) provides a direct coupling between the flame and the flow, including direct phase information. The eigenvalues of the DMD analysis can be seen in Fig. (9.19).

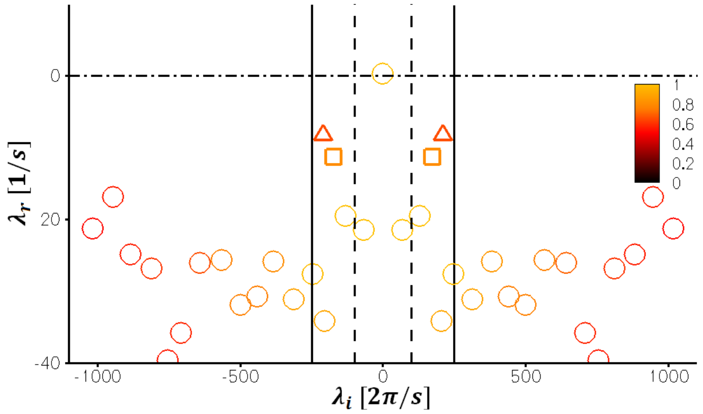

Figure 9.19: Eigenvalues λ, $\sigma = \exp(\lambda \Delta t)$, of the DMD analysis. The imaginary part λ_i represents the angular frequency while the real part λ_r determines the modal rate of growth/decay. The color scale shows the relative mode energies, and the vertical solid and dashed lines give what is deemed acceptable high and low frequency limits, respectively, for well captured modes. The square and the triangle correspond to the upper and lower flow modes in Fig. (9.20), respectively.

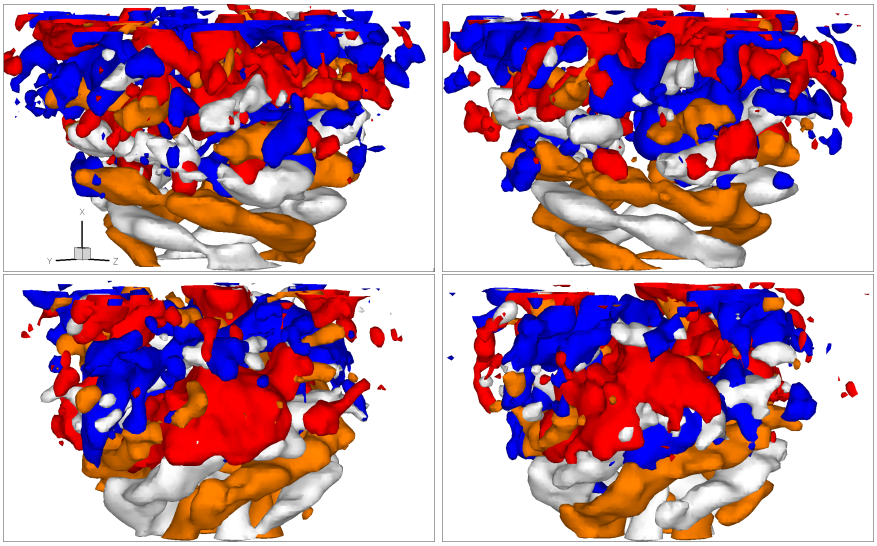

Figure 9.20: Real (left) and imaginary (right) parts of the two DMD modes seen as a square (upper) and triangle (lower) in Fig. (9.19). The orange and white iso-surfaces corresponds to positive and negative radial velocity, respectively, whereas the red and blue iso-surfaces show respectively positive and negative values of the G-field.

The modes corresponding to the square and the triangle in Fig. (9.19), whose flow modes were already given in Fig. (9.16), are shown in Fig. (9.20) for the flow-flame coupling. The $|m| = 3$ mode, the lower mode in Fig. (9.20) which rotates in the same direction as the mean flow while winding in the opposite direction, is seen to correlate well with the flame. The $|m| = 2$ mode on the other hand, the upper mode in Fig. (9.20), which rotates in the opposite direction to the flow while winding in same (general) direction, does not seem to correlate with the flame. This is seen more clearly in the horizontal cross sections shown in Fig. (9.21). Thus, the $|m| = 3$ mode is shown to be the important structure regarding the shape and improved stability of the flame.

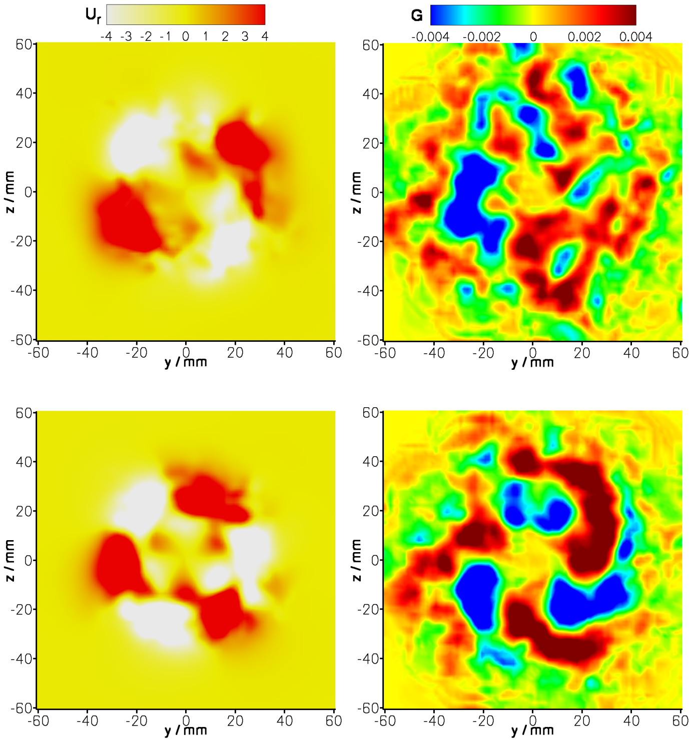

Figure 9.21: Horizontal cross sections of the $|m| = 2$ mode (top) and $|m| = 3$ mode (bottom) taken at heights $0.3D$ for the radial velocity, and $0.7D$ for the G-field, above the burner rim.

For the considered case, one should particularly note the difficulty in catching the correlation found between flow and flame using only point data. This observation, together with the inherent limitations of POD, shows the strength of a method such as the DMD. The procedure used to connect the flow and the flame appears promising.

Chapter 10

Summary of results - Flow around interacting cylinders and beams

Flow around solid objects, which in turn respond to the flow, is important for many practical applications. The flow exerts forces on objects and these may alter the geometry itself, whereby a nonlinear interaction between the fluid and the structures occurs. By their nonlinear nature, the stability of such interaction is essential for maintaining the structural integrity of the objects. Applications include airplane wings, bridges, tall buildings, chimneys, and legs of oil rigs, to name a few. In particular, the notion of resonance between the fluid and the solid structure can be very essential and has to be avoided in many applications. Similarly to the previous investigations in this thesis, the formation and stability of large scale structures around bluff bodies are in focus. The geometries considered are of a general type, placing the nature of the studies more towards the fundamental side.

The two investigations in this chapter differ from the other cases due to the need for different mesh handling. In Section (10.1) the *Immersed Boundary Method* (IBM) is used for flow around cylinders, while in Section (10.2) a moving mesh is used for flow around a cantilever beam. In both of these studies *no special treatment* is given, in terms of the mode decomposition techniques. However, the interpretation of the results becomes a bit different. For the IBM, especially, the behaviour of the modes in the immediate vicinity of the cylinders should be handled with some care. For the moving mesh, the cells close to beam were always at (approximately) the same distance (as opposed to the IBM where they were "turned off"). The cell deformation is also deemed to be small enough to not cause further difficulties.

10.1 Single and multiple cylinders connected to springs

The flow past a single, or an array of, rigid circular cylinder(s), suspended by springs obeying Hooke's law is considered. Compared to the other cases treated in this thesis, the flow velocities in this investigation are small. Figure (10.1) shows the single cylinder setup together with the multiple cylinder arrangements with and without staggering of the downstream cylinders. The cylinders span the entire 4D long channel in the spanwise (y) direction and are only allowed to oscillate in the x-direction.

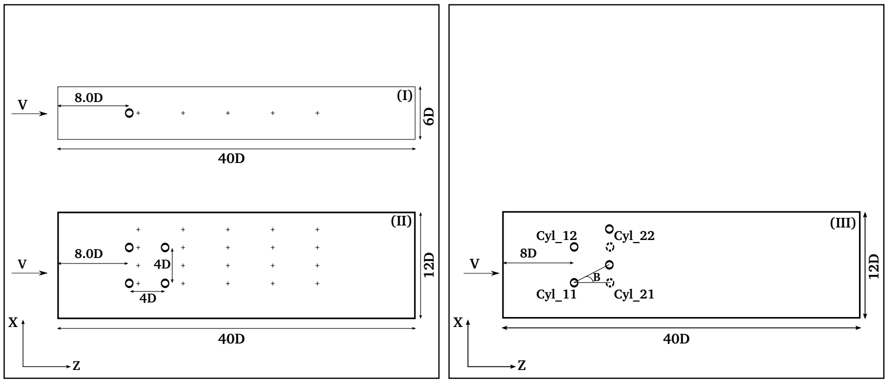

Figure 10.1: Cross sections of the three different geometries considered. $V = V_\infty$ represents the incoming flow. Top left: single cylinder setup, bottom left: multiple cylinder arrangement, bottom right: multiple cylinder arrangement with staggering. B $(= \beta) = 20°$ is the staggering angle. The '+' signs represent probe locations.

The flow may be categorized into three main regions, denoted the *pre-lockin*, *lockin*, and *post-lockin* regions. The notion of "locking in" refers to a region of resonance where the motion of the cylinder and the vortex shedding are synchronized, giving rise to large amplitude oscillations. This happens as the frequency of the vortex shedding approaches the natural frequency of the cylinder in the fluid. Thus, there is a qualitative difference in the system behaviour for shedding frequencies close to the natural frequency of the cylinder-spring system. The main questions to answer with this study are:

- Single cylinder: There are *two characteristic frequencies* in this system, the von Karman shedding frequency of the bluff body flow and the natural frequency of the cylinder-spring system. How are they reflected in the wake?
- Multiple cylinders, non-staggered: How do the different cylinders interact?

- Multiple cylinders, staggered: What are the main differences to the non-staggered case?

The different flows around a single and an array of interacting cylinders were investigated in terms of the flow structures for different ω_N^*, the dimensionless natural frequency of the spring-cylinder system. Three different regions were studied; the pre-lockin region for large ω_N^*, the lockin region where the natural frequency is close to the von Karman shedding frequency, and the post-lockin region for small ω_N^*. The cylinders were only allowed to oscillate in the crossflow direction, with an assumed linear response, giving a cylinder deviation $x = x(t)$ following a Newton equation for an undamped driven harmonic oscillator. The code used dimensionless quantities, e.g. $x \rightarrow x^* = x/D$, where D is the cylinder diameter, leading to the governing equation

$$m^* \frac{d^2 x^*}{dt^{*2}} + k^* x^* = C_x(t), \tag{10.1}$$

where m^* is the dimensionless cylinder mass, k^* is the dimensionless spring constant, and C_x is the dimensionless force excerted by the fluid (in the x-direction) created by the flow. The effects of added mass are included implicitly by solving the coupled system of eq. (10.1) and the flow equations simultaneously in each time step. Furthermore, the added mass enters into the force that the fluid exerts on the object and is computed (expressed by C_x) and added to the momentum equations with opposite sign. The different flow regions, as already stated, were computed by changing the dimensionless natural frequency of the springs, $\omega_N^* = D\omega_N/V_\infty = \sqrt{k^*/m^*}$, where V_∞ is the incoming uniform flow speed. The Reynolds number $Re = \rho V_\infty D/\mu = 400$ is kept fixed. Since the dimensionless mass is also kept fixed, $m^* = \pi$, it is actually the dimensionless spring constant k^* that is varied.

10.1.1 Results - Single cylinder

Spectra of the cylinder motion, for the single cylinder cases, can be seen in Fig. (10.2). The two frequencies in the pre-lockin region (the lower shedding frequency and the higher natural frequency) go to a single frequency in the lockin region, and finally to a more broadband signal in the post-lockin region. It is the (dimensionless) natural frequency that is varied while the Strouhal number for the shedding is $St \approx 0.2$ in all regions.

Because of the presence of just a few dominating modes of different frequencies, a DMD analysis seems very applicable. DMD modes 2 (von Karman shedding) and 7 (mode oscillating at the natural frequency), in the pre-lockin region, are shown in Fig. (10.3). The modes are shown together with normalized time coefficients and spectra, obtained using projections. Recall that the velocity is scaled with the incoming uniform flow speed V_∞. DMD mode 3 (the third largest mode in terms of global energy content) is shown in Fig. (10.4). Note that this mode has a frequency $f_3 \approx |f_2 - f_7|/2$, which is hardly visible in the cylinder motion (Fig. (10.2)).

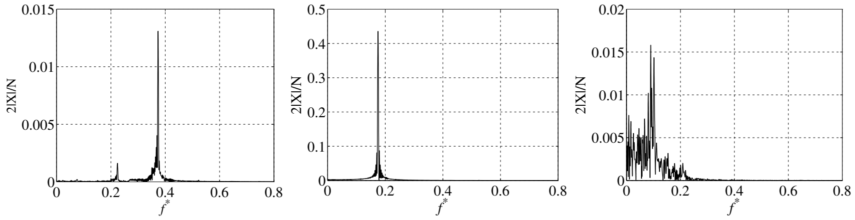

Figure 10.2: Frequency spectra of the cylinder motion for the three regions, pre-lockin (left), lockin (middle), and post-lockin (right). Note the larger amplitude (above 0.4 diameters) in the lockin region.

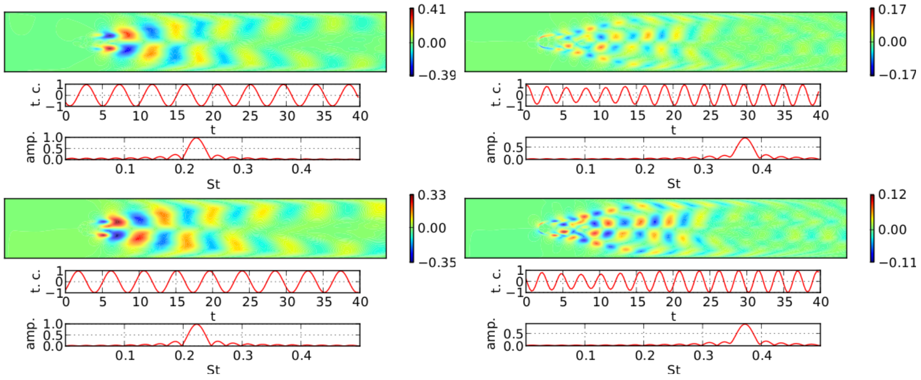

Figure 10.3: The axial component (z-component) of DMD modes 2 (left) and 7 (right), with the real and imaginary parts on the top and bottom, respectively, in the pre-lockin region. Since projections were made, the scales are physical, measured in units of the incoming uniform flow speed V_∞.

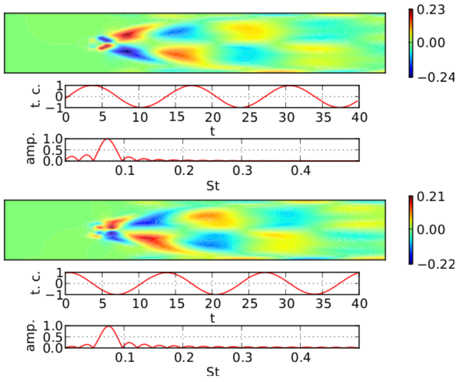

Figure 10.4: The axial component of DMD mode 3 in the pre-lockin region.

DMD modes for the lockin region show an overwhelming dominance of just the coupled shedding/natural frequency mode together with its first few harmonics. In the post-lockin region, DMD mode 2 represents the von Karman shedding, while mode 5 represents a structure oscillating at the natural frequency. Again, an energetic low frequency mode with $f_3 \approx |f_2 - f_5|/2$ appears, similar to the pre-lockin region. This mode is believed to be connected to an interaction between the von Karman shedding and the natural frequency mode, through a mechanism such as e.g. vortex-pairing. If this is the case, the natural frequency, which very much dominates the cylinder motion, gives a relatively weak *direct* impact in the wake, while giving a much larger contribution through the low frequency mode 3. However, the hypothesis has not been verified.

While there are similarities between the pre- and post-lockin regions, the post-lockin case appears chaotic, as suggested in Fig. (10.2). The reason for this is believed to stem from the smaller spring constant ("looser spring") giving a cylinder-spring system which is *much more susceptible to disturbances*. This leads to a larger influence of the low frequency mode on the cylinder motion, which in turn effects the low frequency mode. This type of *feedback process* causes the dynamics to be much more complicated and the frequency content to be more broadband.

10.1.2 Results - Multiple cylinders

In the following we focus on the non-staggered configuration (the square formation), although an analysis was also carried out for the staggered case. The displacement of the two upstream cylinders in the pre-lockin region are shown to the left in Fig. (10.5), where it is seen that the motion is *in phase*. Note that the cylinders initially are completely motionless and that their transient behaviour is very different. Nevertheless, somehow information seems to be transferred from one cylinder to the other, leading to this synchronized motion. *W*hat is the mechanism behind this occurrence? It brings to mind the notion of *phase-locking* (familiar in the study of chaotic systems), where only a *very small* coupling between two independent (identical) oscillators is necessary to give this kind of synchronization. Furthermore, the downstream cylinders are shown to have larger maximum amplitudes along with more erratic behaviour.

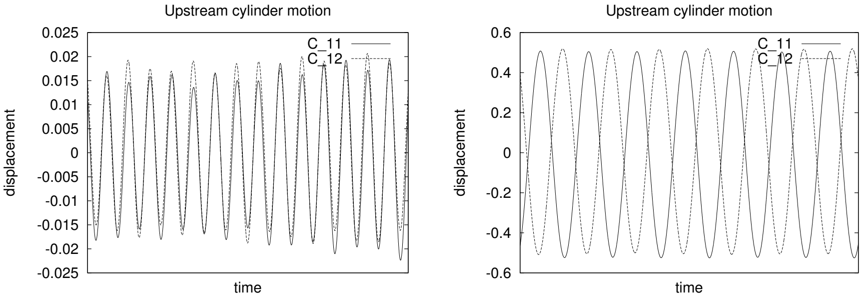

Figure 10.5: Displacement $x^*(t)$ of the two upstream cylinders (see Fig. (10.1)), for the non-staggered configuration, in the pre-lockin region (left) and the lockin region (right).

The left hand side in Fig. (10.6) shows the most energetic fluctuating DMD mode in the pre-lockin region. The Strouhal number takes the value $f^* = 0.23$, which is similar to the shedding mode in the single cylinder case (see mode 2 in Fig. (10.3)), and the mode is symmetric about the centre line. The symmetry implies a forcing towards a cylinder motion *180° out of phase*, which is clearly distinct from what is seen to the left in Fig. (10.5).

As was learnt for the single cylinder case in the post-lockin region, the temporal fluctuations in both the cylinder motion and in the wake are much more erratic. DMD mode 4 ($f^* = 0.21$) for the post-lockin case is given to the right in Fig. (10.6). This mode is seen to be similar to mode 2 in the pre-lockin region, both in terms of spatial structure and frequency, and in the same way this suggests a forcing towards a cylinder motion roughly 180° out of phase. Note that mode 2 in the post-lockin region has a lower frequency ($f^* = 0.17$), and is asymmetric, while mode 3 ($f^* = 0.20$) decays quite rapidly.

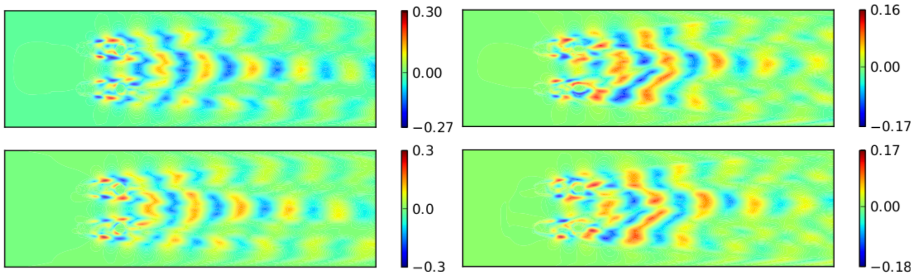

Figure 10.6: Real (top) and imaginary (bottom) part of the axial component of two DMD modes. Left: mode 2 for pre-lockin, right: mode 4 for post-lockin.

The upstream cylinder displacement in the lockin region is shown to the right in Fig. (10.5). Here a cylinder motion almost 180° out of phase can be seen (*frequency-locking*). Note the large amplitudes. The dominating fluctuating

DMD mode for the lockin region is shown in Fig. (10.7). The symmetry of the strong mode reflects what is seen in the cylinder motion, Fig. (10.5).

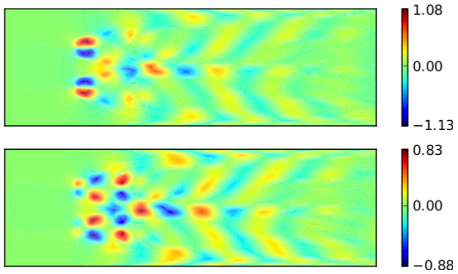

Figure 10.7: Real (top) and imaginary (bottom) part of the axial component of DMD mode 2 in the lockin region.

Looking at Fig. (10.5), together with the symmetry of the shedding modes in Figures (10.6) and (10.7), knowing that the cylinders displayed very different transient behaviour, suggest *two opposing mechanisms* influencing the cylinder motion. One of these mechanisms is the von Karman shedding, which favours oscillations of the upstream cylinders in anti-phase, and another, unknown mechanism, favouring oscillations in phase. Because of the influence of the upstream cylinders on the ones downstream, analysis of the downstream cylinders naturally becomes more complicated.

An overall observation that can also be made is that the *low frequency mode*, so prominent for the single cylinder cases in the pre- and post-lockin regions, is suppressed for the multiple cylinder cases.

10.2 Stiff and flexible beams

In this case the wake structures of cantilever beams with square cross sections, one stiff (stationary, rigid) and one flexible, are investigated. The beams are otherwise identical. A cross section in the centre of the channel is shown in Fig. (10.8), where the flow moves from left to right.

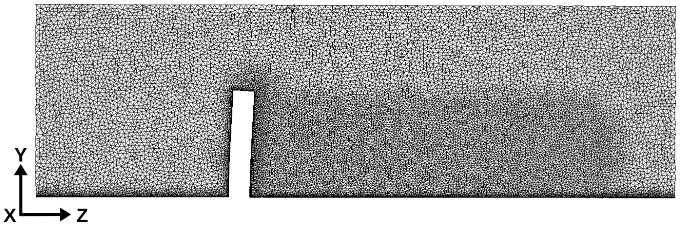

Figure 10.8: Cross section of the fluid mesh.

The computational domain has dimensions 9D×9D×30D while the beam has dimensions 1D×5D×1D, centrally located 9D from the inlet. The velocity field on the lateral and top boundaries is restrained by a slip condition, while for the bottom boundary and the beam there is a no-slip condition. The Reynolds number is $Re = v_\infty D/\nu = 50000$, where v_∞ is the uniform axial inlet velocity. The main goal of the study is:

- Characterize the flow structures giving rise to the forces experienced by the beams.

10.2.1 Results

The integrated dimensionless force on the flexible beam is given in Fig. (10.9), where C_x may be considered to be the lift while C_z is the drag force. The lift force is seen to exhibit a beat frequency where the high amplitudes coincide with the peaks in the drag force. The corresponding spectra are shown in Fig. (10.10). The frequencies making up the beating have Strouhal numbers around $St \approx 0.11$, while C_y and C_z clearly peak at much lower frequencies.

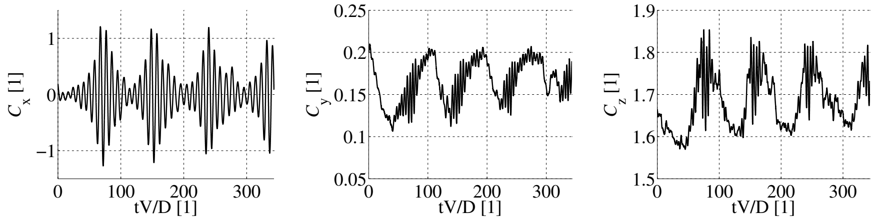

Figure 10.9: Integrated dimensionless force coefficients, as a function of dimensionless time, for the flexible beam.

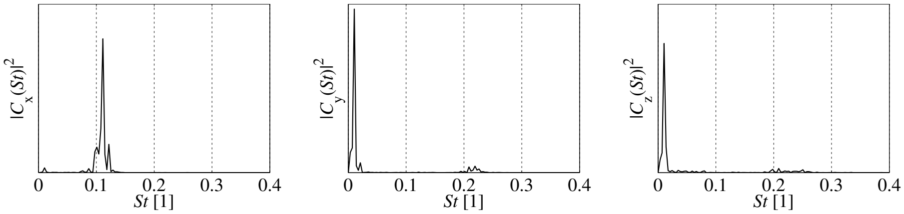

Figure 10.10: Power spectra of the signals in Fig. (10.9).

The integrated dimensionless force on the stiff beam is given in Fig. (10.11), with the corresponding spectra in Fig. (10.12). While there are clear similarities, for the flexible beam, Fig. (10.9), the beat frequency in the lift is much more consistent compared to the more intermittent behaviour seen for the stiff beam.The fluid-structure coupling amplifies the interaction.

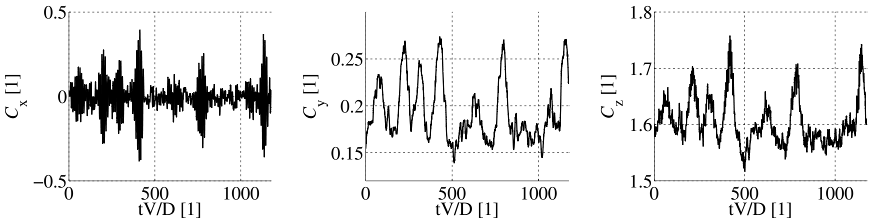

Figure 10.11: Integrated dimensionless force coefficients, as a function of dimensionless time, for the stiff beam.

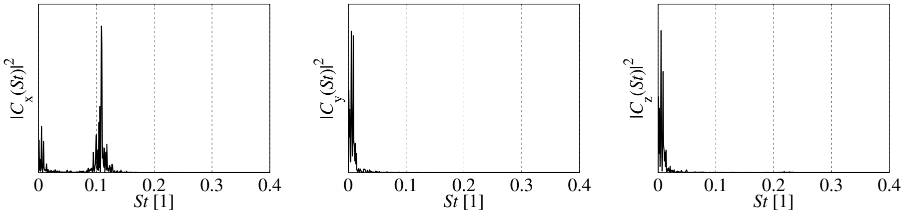

Figure 10.12: Power spectra of the signals in Fig. (10.11).

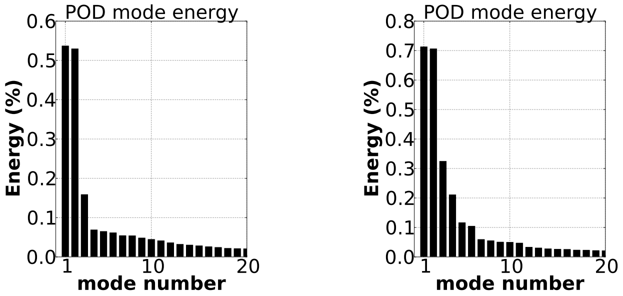

Figure 10.13: POD eigenvalues, for the stiff (left) and flexible (right) beam cases, showing results for the first 20 fluctuating modes.

POD analyses have been carried out on the flow fields. The resulting energy distributions, considering only the fluctuating modes (ignoring the mean which is mode 0), are shown in Fig. (10.13). Since both the stiff and the flexible beam studies show similar overall characteristics, the focus will here (because of the intermittent behaviour of the stiff beam) be on the flexible beam. POD modes 1 and 2, Fig. (10.14), are recognized as the von Karman shedding behind a bluff body. From the anti-symmetry of these modes, it is seen why they only show up (to any noticeable extent) in the lift, and not in the drag (see Figures (10.10) and (10.12)). On the other hand, from the symmetric structure of POD modes 3 and 4, Fig. (10.15), a contribution to the drag is expected. The different extrema of the time coefficients can be directly correlated to extrema in the drag. The negative peaks in the time coefficients for POD mode 3 correspond to the positive peaks in the drag and the large amplitude of the envelope for the beats in the lift, Fig. (10.9). Looking at the colour of the iso-contours of POD mode 3 around the beam, where black is the negative contour, the negative peaks in the time coefficients are seen correspond to positive contributions to the flow velocity. A strong structure comparable to the low frequency structure has also been documented in a similar system [42].

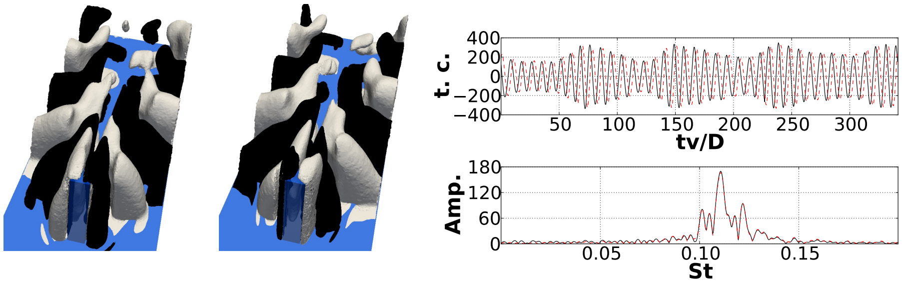

Figure 10.14: Left: positive and negative isocontours of the axial (z-) components of POD modes 1 and 2. Right: accompanying time coefficients with spectra. Solid line: mode 1, dashed line: mode 2.

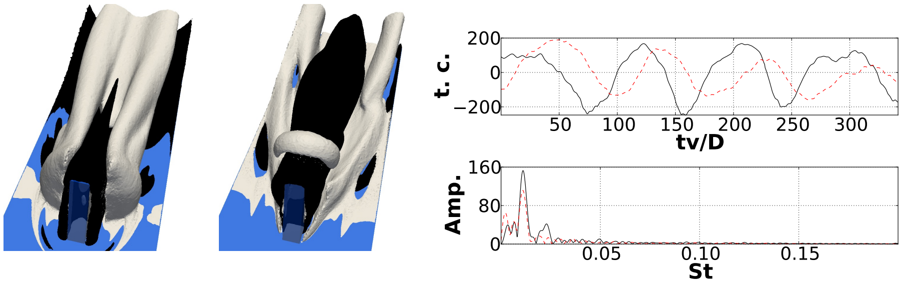

Figure 10.15: Left: positive and negative isocontours of the axial (z-) components of POD modes 3 and 4. Right: accompanying time coefficients with spectra. Solid line: mode 1, dashed line: mode 2.

To really be able to separate out structures based on frequency, a DMD analysis was performed. The results of the decomposition are shown in Figures (10.16) and (10.17). The modes in fig. (10.16) are similar to the POD modes in Figures (10.14) and (10.15). DMD mode 4, in Fig. (10.17), with a Strouhal number very close to that of DMD mode 2, can be considered as part of the von Karman shedding. DMD mode 6, on the other hand, has the frequency $St_6 = 0.098$ and is more concentrated towards the centre of the wake. Therefore, with $St_6 \approx St_2 - St_3$, DMD mode 6 (and similar modes) is believed to be the result of an interaction between DMD modes 2 and 3. With its antisymmetric shape it is expected to contribute to the lift, which, together with DMD mode 2, gives rise to the beat frequency $St_{beat} \approx |St_2 - St_6| \approx St_3$ shown in Fig. (10.9).

It may be noted that the type of structure separation seen in Figures (10.16) and (10.17) cannot be accomplished, at least not easily, by using POD alone. Note also the difference in frequency for the von Karman shedding (see spectra in Fig. (10.14)) compared to the low Reynolds number cylinder cases (Section (10.1)).

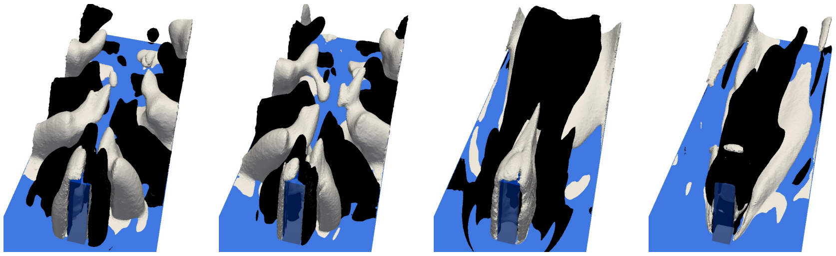

Figure 10.16: DMD modes, real/imag., 2 (left) and 3 (right). Mode 2: $St \approx 0.110$, mode 3: $St \approx 0.010$.

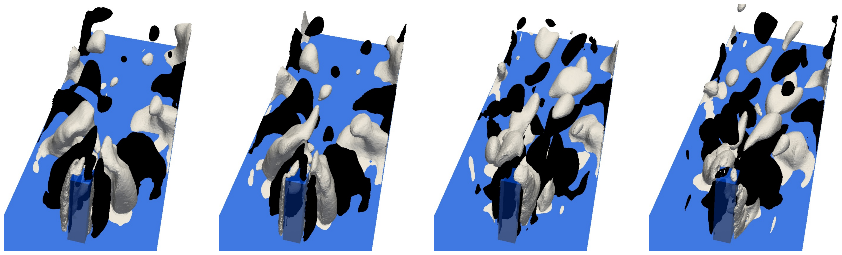

Figure 10.17: DMD modes, real/imag., 4 (left) and 6 (right). Mode 4: $St \approx 0.109$, mode 6: $St \approx 0.098$.

Chapter 11

Summary of papers and contributions

Paper I
C. Carlsson, E. Alenius, and L. Fuchs - Swirl switching in turbulent flow through 90° pipe bends. To be submitted for journal publication.

The swirl switching phenomenon for flow through 90° pipe bends was investigated using LES. A proposition was made to divide the swirl switching into two different phenomenon, a low frequency and a high frequency switching, each with its own distinct physical origin. While the low frequency switching was argued to result from incoming very-large-scale motion, coming from the upstream pipe, the high frequency switching was a result of the bend itself, and was stronger for sharp bends.

C. Carlsson carried out all the simulations, and did the general post-processing and POD (except for the 3-D POD of the straight pipe, which was carried out by E. Alenius). C. Carlsson had the main role in the analysis of the data and in writing the first version of the paper.

Paper II
Y. Wu, C. Carlsson, R. Szazs, L. Fuchs, and X.-S. Bai - Geometry outlet contraction ratio effect to the swirling flow structure and precessing vortex core. To be submitted for journal publication.

The effect of the outlet contraction on a swirling flow for a geometry similar to the Volvo VT40 burner was studied. Two different vortical regions, an outer vortex ring and an inner vortex core, were seen to give unsteady large scale coherent structures. The outer vortex ring, being constrained by the combustor walls, gave an unsteady structure reflecting its deformation, while the inner vortex core inside the combustor, being much less constrained by the walls, instead showed an unsteady structure reflecting its translation. The effect of the outlet contraction ratio on these structures was investigated using POD and DMD.

Y. Wu carried out the basic computations and C. Carlsson carried out the post-processing and analysis using POD and DMD of the velocity field. C. Carlsson made contributions for the physical interpretations of the computed results in addition to writing the relevant parts of the paper. C. Carlsson also created the baseline geometry.

Paper III
P. Petersson, R. Wellander, J. Olofsson, H. Carlsson, C. Carlsson, B. Beltoft Watz, N. Boetkjaer, M. Richter, M. Aldén, L. Fuchs, and X.-S. Bai - Simultaneous high-speed PIV and OH PLIF measurements and modal analysis for investigating flame-flow interaction in a low swirl flame. 16th Int. Symp. on Applications of Laser Techniques to Fluid Mechanics, Lisbon, Portugal, 9-12 July, 2012.

Simultaneous high-speed OH planar laser-induced fluorescence (PLIF) and PIV measurements, as well as LES, were performed for a turbulent low swirl stratified premixed flame. The goal was to investigate the influence of large scale flow structures on the flame, and in particular their impact on the flame stabilization. To accomplish this, mode analysis was used; oscillating pattern decomposition (OPD) for the PIV data, and POD and DMD for the LES data. The experimental part highlighted vortices giving rise to flow reversal in the outer flame region, contributing to large scale mixing, and vortices in the inner region, which, while not giving rise to flow reversal, were still seen to clearly bias the flame propagation. As for the LES, DMD was able to extract two frequency specific helical flow structures, offering a better understanding compared to the POD analysis. The helical structures were believed to contribute to the flame stabilization mechanism.

C. Carlsson performed the POD and DMD of the velocity field from the LES, participated in the analysis of the computational and the experimental results, and contributed in the writing of the numerical parts of the paper.

Paper IV
H. Carlsson, C. Carlsson, L. Fuchs, and X.-S. Bai - Large eddy simulation and extended dynamic mode decomposition of flow-flame interaction in a lean premixed low swirl stabilized flame. *Flow, Turbulence and Combustion* Volume 93 Issue 3 (2014) pp. 505-519 DOI 10.1007/s10494-014-9560-6

The stabilization mechanism of a turbulent stratified premixed flame above a low swirl burner was investigated using LES, expanding on the work in Paper III. Introducing an extended version of DMD (EDMD), the flow and the flame were able to be coupled, showing an anchoring of the outer regions of the flame by one of the two frequency specific helical flow structures coming from the burner.

C. Carlsson introduced a new variant of DMD methodology (EDMD) and used it on the velocity and G-field, participated in the analysis of the results and contributed in the writing of the relevant parts of the paper until it was accepted for journal publication.

Paper V
A. Cesur, C. Carlsson, L. Fuchs, and J. Revstedt - Modal analysis for oscillating cylinder arrays at low Reynolds number. Under review for publication in Journal of Fluids and Structures.

The flow around a single interacting cylinder, as well as an array of interacting cylinders, was studied numerically. Three different flow regimes were considered; one where the frequency of the spring-cylinder system was above the flow induced frequency (pre-lockin regime), one where it was at resonance (lockin regime), and one where it was below the flow induced frequency (post-lockin regime). In particular, a strong low frequency motion was found in the pre- and post-lockin regimes, which was believed to drive the chaotic behaviour in the post-lockin case. For the cylinder array, especially the two leading cylinders, two different mechanisms were proposed to influence the motion. The first was a mechanism involving the von Karman shedding, biasing the cylinders to oscillate in antiphase, while the second was based on an unknown phenomenon, biasing the cylinders to oscillate in phase. Also, for the cylinder array, the low frequency motion, so prominent in the single cylinder case, was suppressed.

A. Cesur carried out the computations. C. Carlsson carried out the DMD of the velocity field, and participated in the analysis of the results, contributing to the physical understanding of the flow. C. Carlsson contributed in the writing of the relevant parts of the paper.

Paper VI
A. Cesur, C. Carlsson, A. Feymark, L. Fuchs, and J. Revstedt - Analysis of the wake dynamics of stiff and flexible cantilever beams using POD and DMD. *Computers and Fluids* **101** (2014) pp. 27-41 DOI 10.1016/j.compfluid.2014.05.012

The forces on a stiff and a flexible cantilever beam were investigated by performing a POD and a DMD analysis of the full high Reynolds number flow, obtained using LES. In addition to the von Karman shedding, a low frequency symmetric structure was seen to modulate the lift force on the beams. An explanation of the forces on the beam were given in terms of frequency specific flow modes.

A. Cesur carried out the computations. C. Carlsson carried out the POD and DMD of the velocity field, and participated in the analysis of the results, contributing to the physical understanding of the flow. C. Carlsson contributed in the writing of the relevant parts of the different versions of the paper until it was accepted for publication.

The following papers have not been included

- H. Carlsson, C. Carlsson, L. Fuchs, and X.-S. Bai - Large eddy simulation and dynamic mode decomposition of flame/flow interaction in a lean premixed low swirl stabilized flame. Eighth Mediterranean Combustion Symposium, Çeşme, Izmir, Turkey, 8-13 September, 2013.
- H. Carlsson, P. Petersson, C. Carlsson, R. Wellander, M. Richter, L. Fuchs, X.-S. Bai, and M. Aldén - Flame speed analysis in a methane/air low swirl premixed flame. European Combustion Meeting, Lund, Sweden, 25-28 June, 2013.
- Y. Wu, C. Carlsson, M. Wessman, J. Klingmann, R. Szazs, L. Fuchs, and X.-S. Bai - Coherent structures and precessing vortex core in a confined swirling flow. To be submitted for journal publication.

Chapter 12

Future work

Future work will include finalizing articles which have not been fully completed, or need to be revised. The author is furthermore interested in the mode selection process regarding (helical) instabilities for swirling flows in simple geometries, which, however, does not assume any homogeneous directions. Such a case is outlined in Section (12.1).

12.1 Bifurcation analysis of a swirling jet

Swirling jets are studied among other things because of the associated increase in spreading rate and mixing (compared to non-swirling jets). The additional, possibly destabilizing, azimuthal shear layer along with potential centrifugal instabilities provide a larger number of pathways to turbulence. For this case a round jet, with an axial velocity profile of top hat character along with swirl of solid body type, is ejected into a rectangular box open at the side opposite to the inlet. For some given swirl number Sw, an attempt will be made to find the two critical Reynolds numbers connected to a steady (symmetry breaking) supercritical pitchfork bifurcation and a Hopf bifurcation (followed by an oscillatory flow). Thus, the main questions may be stated:

- Find the critical Reynolds number $Re_{cr}(Sw)$ for symmetry breaking, and the associated flow mode
- Find the critical Reynolds number $Re_{cr}(Sw)$ for the onset of oscillatory flow, and the associated flow mode

To make it easier to answer the questions stated above, one should compute not only the velocity field u, but also the first and second partial derivatives of u with respect to $\epsilon \equiv \frac{1}{Re}$, u_ϵ and $u_{\epsilon\epsilon}$ [68]. The equation for these variables can be derived by taking the derivatives of the velocity vector with respect ϵ in the momentum equations. The solution of the linear problem would be straightforward and yields information about the sensitivity and possible singularity of the solution with respect to increasing Reynolds number.

Acknowledgements

This work was carried out at the Division of Fluid Mechanics, Department of Energy Sciences, Lund University, Sweden. The work was financially supported by the Swedish Research Council (VR), and the computational resources were provided by the Swedish National Infrastructure for Computing (SNIC), via the Centre for Scientific and Technological Computing at Lund University (LUNARC).

I would like to thank my supervisor Professor Laszlo Fuchs for all his help and for introducing me to this interesting field of research. I would also like to thank my co-supervisors Professor Xue-Song Bai and Doctor Robert Szász for all their comments and support. Thank you also to Professor Johan Revstedt for answering many of my questions on the fly.

Furthermore, I would like to thank my roommate Rickard Solsjö for all the interesting conversations, regarding work and otherwise, and overall for being a good guy. Also, I would like to thank Henning Carlsson, Emma Alenius, Alper Cesur, Yajing Wu, and Per Petersson for all the fruitful discussions and collaborations. A special thanks to Emma for the help in reviewing the thesis. Thank you also to Hesameddin Fatehi, Rixin Yu, Mehdi Jangi, and Johan Lorentzon for the interesting conversations regarding general topics in fluid mechanics.

Thanks also to Ali Al Sam, Tobias Joelsson, Jiangfei Yu, Fan Zhang, Naser Hamedi, Erdzan Hodzic, Cheng Gong, Vivianne Holmén, Henrik Bär, Weiwei Li, Qing Li, and all the former PhD students that I've interacted with, for brightening my days. Finally, I would like to thank my family for their support.

Bibliography

[1] H. D. I. Abarbanel, R. Brown, J. J. Sidorowich, and L. Sh. Tsimring. The analysis of observed chaotic data in physical systems. *Rev. Modern phys.*, 65(4), 1993.

[2] S. C. C. Bailey and A. J. Smits. Experimental investigation of the structure of large- and very-large-scale motions in turbulent pipe flow. *J. Fluid Mech.*, 651:339–356, 2010.

[3] S. A. Berger, L. Talbot, and L.-S. Yao. Flow in curved pipes. *Ann. Rev. Fluid Mech.*, 15:461–512, 1983.

[4] J. Borée. Extended proper orthogonal decomposition: a tool to analyse correlated events in turbulent flows. *Experiments in Fluids*, 35:188–192, 2003.

[5] R. Brown, P. Bryant, and H. D. I. Abarbanel. Computing the lyapunov spectrum of a dynamical system from an observed time series. *Phys. Rev. A*, 43(6), 1991.

[6] Ch. Brücker. A time-recording dpiv-study of the swirl switching effect in a 90° bend flow. *Proc. 8th International symposium on flow visualization, Sorrento (NA), Italy, Sept. 1-4*, pages 171.1–171.6, 1998.

[7] P. Bryant, R. Brown, and H. D. I. Abarbanel. Lyapunov exponents from observed time series. *Phys. Rev. Lett.*, 65(13), 1990.

[8] C. D. Cantwell, D. Barkley, and H. M. Blackburn. Transient growth analysis of flow through a sudden expansion in a circular pipe. *Phys. Fluids*, 22(034101), 2010.

[9] K. K. Chen, J. H. Tu, and C. W. Rowley. Variants of dynamic mode decomposition: boundary conditions, koopman, and fourier analyses. *J. Nonlinear Sci*, 22:887–915, 2012.

[10] S. I. Chernyschenko and M. F. Baig. The mechanism of streak formation in near-wall turbulence. *J. Fluid Mech.*, 544:99–131, 2005.

[11] P. A. Davidson, Y. Kaneda, and K. R. Sreenivasan. *Ten chapters in turbulence*, chapter 6: Dynamics of wall-bounded turbulence. Cambridge University Press, 2013. The authors of Chapter 6 are J. Jiménez and G. Kawahara.

[12] J. C. del Álamo and J. Jiménez. Linear energy amplification in turbulent channels. *J. Fluid Mech.*, 559:205–213, 2006.

[13] P. G. Drazin. *Introduction to hydrodynamic stability.* Cambridge University Press, 2002.

[14] C. Duwig and P. Iudiciani. Extended proper orthogonal decomposition for analysis of unsteady flames. *Flow, Turbulence and Combustion*, 84:25–47, 2010.

[15] B. Eckhardt, T. Schneider, B. Hof, and J. Westerweel. Turbulence transition in pipe flow. *Annu. Rev. Fluid Mech.*, 39:447–468, 2007.

[16] F. Gallaire and J.-M. Chomaz. Instability mechanisms in swirling flows. *Phys. Fluids*, 15(9), 2003.

[17] J. Gleick. *Chaos.* Vintage, 1998. Originally published in 1987.

[18] M. Guala, S. E. Hommema, and R. J. Adrian. Large-scale and very-large-scale motions in turbulent pipe flow. *J. Fluid Mech.*, 554:521–542, 2006.

[19] J. Guckenheimer. Strange attractors in fluids: another view. *Ann. Rev. Fluid Mech.*, 18:15–31, 1986.

[20] L. H. O. Hellstöm, M. B. Zlatinov, G. Cao, and A. J. Smits. Turbulent pipe flow downstream of a 90° bend. *J. Fluid Mech.*, 735:R7, 2013.

[21] L. H. O. Hellström, M. B. Zlatinov, A. J. Smits, and G. Cao. Turbulent flow through a 90^o bend. *Seventh international symp. on turbulence and shear flow phenomenon*, 2011.

[22] P. Heurre and P. A. Monkewitz. Local and global instabilities in spatially developing flows. *Annu. Rev. Fluid Mech.*, 22:473–537, 1990.

[23] URL: http://www.artofillusion.org.
Latest visit: 2014-03-04.

[24] URL: http://www.claymath.org/millenium-problems.
Latest visit: 2014-03-04.

[25] Y. Hwang and C. Cossu. Self-sustained process at large scales in turbulent channel flow. *Phys. Rev. Lett.*, 105(044505), 2009.

[26] Y. Hwang and C. Cossu. Self-sustained processes in the logarithmic layer of turbulent channel flows. *Phys. Fluids*, 23(061702), 2011.

[27] O. E. Lanford III. The strange attractor theory of turbulence. *Ann. Rev. Fluid Mech.*, 14:347–364, 1982.

[28] R. I. Issa. Solution of the implicitly discretised fluid flow equations by operator-splitting. *J. Comp. Phys.*, 62:40–65, 1986.

[29] H. Jasak. *Error Analysis and Estimation for the Finite Volume Method with Applications to Fluid Flow.* PhD thesis, Imperial College London, 1996.

[30] A. Kalpakli and R. Örlü. Turbulent pipe flow downstream a 90° pipe bend with and without superimposed swirl. *Int. J. Heat Fluid Flow*, 2013.

[31] M. B. Kennel, R. Brown, and H. D. I. Abarbanel. Determining embedding dimension for phase-space reconstruction using a geometrical contruction. *Phys. Rev. A*, 45(6), 1992.

[32] K. C. Kim and R. J. Adrian. Very large-scale motion in the outer layer. *Phys. Fluids*, 1(2), 1999.

[33] B. Leclaire and D. Sipp. A sensitivity study of vortex breakdown onset to upstream boundary conditions. *J. Fluid Mech.*, 645:81–119, 2010.

[34] S. Leibovich and A. Kribus. Large-amplitude wavetrains and solitary waves in vortices. *J. Fluid Mech.*, 216:459–504, 1990.

[35] J. M. Lopez. On the bifurcation structure of axisymmetric vortex breakdown in a constricted pipe. *Phys. Fluids*, 6(11), 1994.

[36] O. Lucca-Negro and T. O. O'Doherty. Vortex breakdown: a review. *Progress in Energy and Combustion Science*, 27:431–481, 2001.

[37] J. L. Lumley. The structure of inhomogeneous turbulent flows. *Atmospheric Turbulence and Radio Wave Propagation*, pages 166–178, 1967.

[38] S. Maurel, J. Borée, and J. L. Lumley. Extended proper orthogonal decomposition: application to jet/vortex interaction. *Flow, Turbulence and Combustion*, 67:125–136, 2001.

[39] C. Meneveau. Germano identity-based subgrid-scale modeling: A brief survey of variations on a fertile theme. *Phys. Fluids*, 24(121301), 2012.

[40] I. Mezić. Analysis of fluid flows via spectral properties of the koopman operator. *Annu. Rev. Fluid Mech.*, 45:357–378, 2013.

[41] J. P. Monty, J. A. Stewart, R. C. Williams, and M. S. Chong. Large-scale features in turbulent pipe and channel flows. *J. Fluid Mech.*, 589:147–156, 2007.

[42] T. W. Muld, G. Efraimsson, and D. S. Henningson. Mode decomposition on surface-mounted cube. *Flow, Turbulence and Combustion*, 88:279–310, 2011.

[43] K. J. Nogenmyr, C. Fureby, X. S. Bai, X. S. Peterson, P. Petersson, R. Collins, and M. Linne. Large eddy simulation and laser diagnostic studies on a low swirl stratified premixed flame. *Comb. Flame*, 156(1):25–36, 2009.

[44] K. J. Nogenmyr, P. Petersson, X. S. Bai, C. Fureby, R. Collin, A. Lantz, M. Linne, and M. Aldén. Structure and stabilization mechanism of a stratified premixed low swirl flame. *Proc. Combust. Inst.*, 33:1567–1574, 2011.

[45] J. Jiménez O. Flores. Vorticity organization in the outer layer of turbulent channels with disturbed walls. *J. Fluid Mech.*, 591:145–154, 2007.

[46] K. Oberleithner, M. Sieber, C. N. Nayeri, C. O. Paschereit, C. Petz, H.-C. Hege, B. R. Noack, and I. Wygnanski. Three-dimensional coherent structures in a swirling jet undergoing vortex breakdown: stability analysis and empirical mode construction. *J. Fluid Mech.*, 679:383–414, 2011.

[47] Kungl. Ingenjörsvetenskapsakademien och Kungl. Vetenskapsakademin. *Energi - möjligheter och dilemman.* Kungl. Vetenskapsakademin, 2009.

[48] M. Olsson and L. Fuchs. Large eddy simulations of a forced semiconfined circular impinging jet. *Phys. Fluids*, 10(476), 1998. DOI 10.1063/1.869535.

[49] R. C. Orbay, K.-J. Nogenmyr, J. Klingmann, and X.S. Bai. Swirling turbulent flows in a combustion chamber with and without heat release. *Fuel*, 104:133–146, 2013.

[50] R. L. Panton. *Incompressible flow. Third edition.* John Wiley & Sons, Inc., 2005.

[51] S. Pope. Ten questions concerning the large-eddy simulation of turbulent flows. *New J. Phys.*, 6(35), 2004.

[52] S. B. Pope. *Turbulent flows.* Cambridge University Press, 2000.

[53] J. Prusa and L.-S. Yao. Numerical solution for fully developed flow in heated curved tubes. *J. Fluid Mech.*, 123:503–522, 1982.

[54] A. Revuelta. On the axisymmetric vortex breakdown of a swirling jet entering a sudden expansion pipe. *Phys. Fluids*, 16(9), 2004.

[55] C. W. Rowley, I. Mezić, S. Bagheri, P. Schlatter, and D. S. Henningson. Spectral analysis of nonlinear flows. *J. Fluid Mech.*, 641:115–127, 2009.

[56] F. Rütten, W. Schröder, and M. Meinke. Large-eddy simulation of low frequency oscillations of the Dean vortices in turbulent pipe bend flows. *Phys. Fluids*, 17(035107), 2005.

[57] Y. Saad. *Numerical methods for large eigenvalue problems. Revised edition*, volume 66 of *Classics in applied mathematics.* Society for Industrial and Applied Mathematics (SIAM), 2011.

[58] J. Sakakibara and N. Machida. Measurement of turbulent flow upstream and downstream of a circular pipe bend. *Phys. Fluids*, 24(041702), 2012.

[59] E. Sanmiguel-Rojas, C. del Pino, and C. Gutiérrez-Montes. Global mode analysis of a pipe flow through a 1:2 axisymmetric sudden expansion. *Phys. Fluids*, 22, 2010.

[60] P. J. Schmid. Nonmodal stability theory. *Annu. Rev. Fluid Mech.*, 39:129–162, 2007.

[61] P. J. Schmid. Dynamic mode decomposition of numerical and experimental data. *J. Fluid Mech.*, 656:5–28, 2010.

[62] P. J. Schmid and D. S. Henningson. *Stability and transition in shear flows*, volume 142 of *Applied Mathematical Sciences*. Springer-Verlag New York, Inc., 2001.

[63] R. Seydel. *Practical bifurcation and stability analysis, Third edition*. Springer, 2010.

[64] J. J. M. Sillekens, C. C. M. Rindt, and A. A. van Steenhoven. Mixed convection in a 90 degrees horizontal bend. *Proceedings of the 10th International Heat Transfer Conference, Brighton UK*, pages 567–572, 1994.

[65] D. Sipp and A. Lebedev. Global stability of base and mean flows: a general approach and its applications to cylinder and open cavity flows. *J. Fluid Mech.*, 593:333–358, 2007.

[66] L. Sirovich. Turbulence and the dynamics of coherent structures. *Q. Appl. Math*, 45:561–590, 1987.

[67] A. J. Smits, B. J. McKeon, and I. Marusic. High-Reynolds number wall turbulence. *Annu. Rev. Fluid Mech.*, 43:353–75, 2011.

[68] R. Z. Szász. *Numerical modeling of flows related to gas turbine combustors*. PhD thesis, Lund Institute of Technology, 2004.

[69] F. Takens. Detecting strange attractors in turbulence. In *Dynamical Systems and Turbulence, Warwick 1980*, volume 898 of *Lecture Notes in Mathematics*, pages 366–381, 1981. DOI 10.1007/BFb0091924.

[70] V. Theofilis. Advances in global linear instability analysis of nonparallel and three-dimensional flows. *Progress in Aerospace Sciences*, 39:249–315, 2003.

[71] V. Theofilis. Global linear instability. *Annu. Rev. Fluid Mech.*, 43:319–352, 2011.

[72] L. N. Trefethen, A. E. Trefethen, S. C. Reddy, and T. A. Driscoll. Hydrodynamic stability without eigenvalues. *Science*, 261(5121):578–584, 1993.

[73] A. Tsinober. *An informal introduction to turbulence. Second edition.* Springer, 2009.

[74] A. Tsinober. *The essence of turbulence as a physical phenomenon.* Springer, 2014.

[75] M. J. Tunstall and J. K. Harvey. On the effect of a sharp bend in a fully developed turbulent pipe flow. *J. Fluid Mech.*, 34:595–608, 1968.

[76] A. Kalpakli Vester. *Vortices in turbulent curved pipe flow - rocking, rolling and pulsating motions.* PhD thesis, Royal Institute of Technology, 2014.

[77] M. O. Vigueras-Zuñiga, A. Valera-Medina, and N. Syred. Studies of the precessing vortex core in swirling flows. *J. Applied Research and Technology*, 10:755–765, 2012.

[78] E. Vyazmina, J. W. Nichols, J.-M. Chomaz, and P. J. Schmid. The bifurcation structure of viscous steady axisymmetric vortex breakdown with open lateral boundaries. *Phys. Fluids*, 21, 2009.

[79] S. Wang and Z. Rusak. The effect of slight viscosity on a near-critical swirling flow in a pipe. *Phys. Fluids*, 9(7), 1997.

[80] J. Warnatz, U. Maas, and R. W. Dibble. *Combustion: Physical and Chemical Fundamentals, Modeling and Simulation, Experiments, Pollutant Formation. 4th Edition.* Springer, 2006.

[81] H. G. Weller, G. Tabor, H. Jasak, and C. Fureby. A tensorial approach to computational continuum mechanics using object-oriented techniques. *Computers in Physics*, 12(6):620–631, 1998.

[82] L.-S. Yao and S. A. Berger. Flow in heated curved pipes. *J. Fluid Mech.*, 88(2):339–354, 1978.